

FABRICATION AND CHARACTERIZATION OF ALUMINUM OXIDE AND
SILICON/ALUMINUM OXIDE FILMS WITH Si NANOCRYSTALS FORMED
BY MAGNETRON CO-SPUTTERING TECHNIQUE

A THESIS SUBMITTED TO
THE GRADUATE SCHOOL OF NATURAL AND APPLIED SCIENCES
OF
MIDDLE EAST TECHNICAL UNIVERSITY

BY

İLKER DOĞAN

IN PARTIAL FULFILLMENT OF THE REQUIREMENTS
FOR
THE DEGREE OF MASTER OF SCIENCE
IN
PHYSICS

JULY 2008

Approval of thesis:

**FABRICATION AND CHARACTERIZATION OF ALUMINUM OXIDE
AND SILICON/ALUMINUM OXIDE FILMS WITH Si NANOCRYSTALS
FORMED BY MAGNETRON CO-SPUTTERING TECHNIQUE**

submitted by **İLKER DOĞAN** in partial fulfillment of the requirements for the degree of **Master of Science in Physics Department, Middle East Technical University** by,

Prof. Dr. Canan Özgen
Dean, Graduate School of **Natural and Applied Sciences** _____

Prof. Dr. Sinan Bilikmen
Head of Department, **Physics** _____

Prof. Dr. Raşit Turan
Supervisor, **Physics Dept., METU** _____

Examining Committee Members:

Prof. Dr. Çiğdem Erçelebi
Physics Dept., METU _____

Prof. Dr. Raşit Turan
Physics Dept., METU _____

Prof. Dr. Mürvet Volkan
Chemistry Dept., METU _____

Assoc. Prof. Dr. Ceyhun Bulutay
Physics Dept., Bilkent University _____

Dr. Hakan Altan
Physics Dept., METU _____

Date: July 15, 2008

I hereby declare that all information in this document has been obtained and presented in accordance with academic rules and ethical conduct. I also declare that, as required by these rules and conduct, I have fully cited and referenced all material and results that are not original to this work.

Name Surname: İlker Doğan

Signature :

ABSTRACT

FABRICATION AND CHARACTERIZATION OF ALUMINUM OXIDE AND SILICON/ALUMINUM OXIDE FILMS WITH Si NANOCRYSTALS FORMED BY MAGNETRON CO-SPUTTERING TECHNIQUE

Doğan, İlker

M.Sc., Department of Physics

Supervisor: Prof. Dr. Raşit Turan

July 2008, 108 pages

DC and RF magnetron co-sputtering techniques are one of the most suitable techniques in fabrication of thin films with different compositions. In this work, Al_2O_3 and $\text{Si}/\text{Al}_2\text{O}_3$ thin films were fabricated by using magnetron co-sputtering technique. For Al_2O_3 films, the stoichiometric, optical and crystallographic analyses were performed. For Si contained Al_2O_3 films, the formation conditions of Si nanocrystals were investigated. To do so, these thin films were sputtered on Si (100) substrates. Post annealing was done in order to clarify the evolution of Al_2O_3 matrix and Si nanocrystals at different temperatures. Crystallographic properties and size of the nanocrystals were investigated by X-ray diffraction (XRD) method. The variation of the atomic concentrations and bond formations were investigated with X-ray photoelectron spectroscopy (XPS). The luminescent behaviors of Si nanocrystals and Al_2O_3 matrix were investigated with photoluminescence (PL) spectroscopy. Finally, the characteristic emissions from the matrix and the nanocrystals were separately identified.

Keywords: Magnetron Co-Sputtering, Al₂O₃, Si nanocrystals, X-Ray Diffraction, X-Ray Photoelectron Spectroscopy, Photoluminescence Spectroscopy.

ÖZ

ALUMİNYUM OKSİT VE SİLİSYUM/ALUMİNYUM OKSİT İNCE FİLMLERİN MIKNATISLI EŞ SAÇTIRMA TEKNİĞİ İLE ÜRETİMİ VE İNCELENMESİ

Doğan, İlker

Yüksek Lisans, Fizik Bölümü

Tez Yöneticisi: Prof. Dr. Raşit Turan

Temmuz 2008, 108 sayfa

Doğru akım (DC) ve radyo frekanslı (RF) mıknatıslı eş saçtırma tekniği, değişik kompozisyonlu ince film üretimi için kullanılan en uygun tekniklerden biridir. Bu çalışmada, Al_2O_3 ve Si/Al_2O_3 ince filmleri mıknatıslı eş saçtırma yöntemi ile üretilmiştir. Al_2O_3 ince filmler için, stokiyometrik, optik ve kristalografik analizler gerçekleştirilmiştir. Si içeren Al_2O_3 örnekler için ise, Si nanokristallerin oluşum koşulları incelenmiştir. Bunun için, ince filmler Si (100) alttaşların üzerine saçtırılmıştır. Al_2O_3 matrisin ve Si nanokristallerin değişik sıcaklıklardaki evrimini incelemek için örnekler üretim sonrası fırınlamaya tabi tutulmuştur. Kristalografik özellikler ve nanokristallerin boyutları X-Işını Kırınımı (XRD) tekniği ile belirlenmiştir. Atomik derişimlerdeki deęişim ve baę oluşumları X-Işını Fotoelektron Spektroskopisi (XPS) ile incelenmiştir. Si nanokristallerin ve Al_2O_3 matrisin ışımaya özellikleri ise Fotoışımaya Spektroskopisi (PL) ile incelenmiştir. Son olarak, matristen ve nanokristallerden gelen karakteristik ışımalar ayrı ayrı tanımlanmıştır.

Anahtar Kelimeler: Mıknatıslı Eş Saçtırma, Al_2O_3 , Si nanokristaller, X-Işını Kırınımı, X-Işını Fotoelektron Spektroskopisi, Fotoışımaya Spektroskopisi.

To my family...

ACKNOWLEDGEMENTS

I would like to thank to my supervisor Prof. Dr. Raşit Turan, for giving me a great chance and opportunity to work with him. Without his guidance, it would be harder to gain and improve my knowledge. With his support, I showed up at international conferences and contributed papers, which are the first milestones of my career. I also would like to thank to Prof. Dr. Çiğdem Erçelebi, Prof. Dr. Mürvet Volkan, Assoc. Prof. Dr. Ceyhun Bulutay and Dr. Hakan Altan for their critical comments and advices on my thesis.

I am most grateful to my family members for their continued moral and support especially to my brother Soner Doğan who was a great motivator to me most of the time.

I am very happy to be a part of Prof. Dr. Raşit Turan's group, Semiconductor Materials and Devices (SMD). I want to thank to my present and former group partners Dr. Uğur Serincan, Dr. Ercan Yılmaz, Dr. İlker Yıldız, Arife Gencer İmer, Ayşe Seyhan, Seda Bilgi, Umut Bostancı, Nader A. P. Moghaddam, Selçuk Yerci, Seçkin Öztürk, Urcan Güler, Sedat Canlı and Döndü Şahin. I would especially like to thank to Mustafa Kulakcı for his great ideas, great jokes and great personality, to Buket Kaleli for being not just like a group partner but also a close friend of mine, to Arif Sinan Alagöz for teaching me the "art" of sputtering, to Yücel Eke for his technical support and great friendship, to Savaş Ulucan for being as close as a brother. I also want to thank to people in Central Laboratory, for SEM and XPS measurements. For AFM images, I would also like to thank to Dr. Aykutlu Dana.

I would like to thank to my work friends who studied with me and gaining motivation to me: Beste Korutlu, Sinem Bayar Özbilgen, Elif Beklen, Kadir Gökşen, Oktay Aydoğdu, Nader Ghazanfari, Tahir Çolakoğlu, Murat Kaleli, Hazbullah Karaağaç, Engin Özkol, Şeyda Şahiner and Seçkin Kıntaş. I would like

to thank to Seda Şalap and Hasan Başar Şık for being my best friends for long years, to Erdem Aytakin for our late night therapies, and finally to Nurcan Yanarcan for her invaluable support. Without her presence, nothing could be that easy and confident.

TABLE OF CONTENTS

ABSTRACT	iv
ÖZ	vi
ACKNOWLEDGEMENTS	viii
TABLE OF CONTENTS	x
LIST OF TABLES	xiii
LIST OF FIGURES	xiv
LIST OF ABBREVIATIONS	xix
CHAPTERS	
1. INTRODUCTION	1
1.1 Introduction	1
1.2 Plenty of Room at the Bottom.....	2
1.3 The Famous Trinity and Search for New Structures.....	3
1.3.1 Nanocrystal Based FLASH Memory Cells, LEDs and Solar Cells	5
1.3.2 Al ₂ O ₃ as an Alternative Host Matrix for Si Nanocrystals.....	8
1.4 Overview of the Dissertation	9
2. STRUCTURAL AND THEORRETICAL APPROACH TO Al ₂ O ₃ AND Si NANOCRYSTALS	11
2.1 Introduction.....	11
2.2 Properties and Theoretical Background about Al ₂ O ₃	12
2.2.1 Crystallographic Properties.....	12
2.2.2 Optical and Electronic Properties.....	17
2.2.2.1 Electron Band Structure – Density Functional Theory	17

2.2.2.2 Optical Constants	25
2.3 Nanocrystals – Quantum Mechanical Aspects.....	28
2.3.1 Weak Confinement	28
2.3.2 Strong Confinement	31
2.3.3 Growth of Nanocrystals in a Matrix.....	32
3. INSTRUMENTATION FOR FABRICATION AND CHARACTERIZATION	34
3.1 Introduction.....	34
3.2 Magnetron Sputtering	34
3.2.1 Sputtering Methods	38
3.2.1.1 RF Magnetron Sputtering.....	38
3.2.1.2 DC Magnetron Sputtering.....	39
3.2.2 Reactive and non Reactive Sputter Deposition.....	40
3.2.3 Changing the geometry of the Target.....	41
3.3 X-Ray Diffraction	41
3.3.1 Ideal Diffraction Conditions	41
3.3.2 Non-Ideal Diffraction Conditions	43
3.4 Scanning Electron Microscopy	45
3.5 X-Ray Photoelectron Spectroscopy	48
3.6 Photoluminescence Spectroscopy	51
4. FABRICATION AND CHARACTERIZATION OF Al ₂ O ₃ SPUTTERED FILMS.....	55
4.1 Fabrication	55
4.2 Characterization	58
4.2.1 X-Ray Diffraction	58
4.2.2 Atomic Force Microscopy.....	63

4.2.3	X-Ray Photoelectron Spectroscopy.....	65
4.2.4	Photoluminescence Spectroscopy	67
4.3	Application to MOS Based Radiation Sensors	70
5.	FABRICATION AND CHARACTERIZATION OF Si NANOCRYSTALS IN Al ₂ O ₃ CO-SPUTTERED FILMS.....	74
5.1	Fabrication	74
5.2	Characterization	76
5.2.1	X-Ray Diffraction	76
5.2.2	Photoluminescence Spectroscopy	83
5.2.3	X-Ray Photoelectron Spectroscopy	89
6.	CONCLUSION AND FUTURE WORK.....	96
	REFERENCES.....	98

LIST OF TABLES

TABLES

Table 2.1.	Comparison of the crystal structures of α -Al ₂ O ₃ (Space group $R\bar{3}C$)	14
Table 2.2.	Electron and hole effective masses of different aluminas	22
Table 4.1.	Details of the pre-sputtering procedure	55
Table 4.2.	Details of the sputtering procedure.....	57
Table 4.3.	The transition forms, included by the films at different temperatures.....	62
Table 4.4.	Atomic percentages of sample C22, with respect to increasing annealing temperatures	66
Table 5.1.	Details of the sputtering procedure.....	75
Table 5.2.	The physical parameters, gathered from the XRD scans.....	81

LIST OF FIGURES

FIGURES

Figure 1.1.	A typical MOS capacitor	3
Figure 1.2.	Schematic diagram of a conventional gate FLASH memory cell	4
Figure 1.3.	Direct and indirect absorption in semiconductors	5
Figure 1.4.	Si nanocrystal based FLASH memory device	6
Figure 1.5.	Loss process in a standard solar cell: (1) non-absorption of below band gap photons; (2) lattice thermalization loss; (3) and (4) junction and contact voltage losses; (5) recombination loss	7
Figure 1.6.	Third generation multiple band gap nanocrystal tandem solar cells	8
Figure 2.1.	Crystal structure of α -Al ₂ O ₃ in hexagonal lattice	13
Figure 2.2.	Thermal transformation pathway of different aluminum hydroxides	15
Figure 2.3.	X-ray diffraction powder curves of (a) chi-Al ₂ O ₃ , (b) kappa-Al ₂ O ₃ , (c) gamma-Al ₂ O ₃ , (d) delta-Al ₂ O ₃ , (e) theta-Al ₂ O ₃ , (f) eta-Al ₂ O ₃ , (g) α -Al ₂ O ₃	16
Figure 2.4.	LDA band structure and total DOS of α -Al ₂ O ₃	21
Figure 2.5.	Calculated total and partial DOS of α -Al ₂ O ₃	23
Figure 2.6.	Calculated orbital resolved partial DOS of α -Al ₂ O ₃	24
Figure 2.7.	The reflectance of single crystalline α -Al ₂ O ₃	27
Figure 2.8.	Transmittance spectrum of α -Al ₂ O ₃	27

Figure 2.9.	The density of states of carriers in different confinement configurations (a) bulk, (b) quantum well, (c) quantum wire, (d) quantum dot	29
Figure 3.1.	The main chamber of the sputter deposition system located in Semiconductor Material & Device Fabrication Lab.....	35
Figure 3.2.	The targets used in the experiments: Al ₂ O ₃ (left) and Si (right) ...	36
Figure 3.3.	Sputter rate with respect to magnetron power (above) and Ar flow rate (below). Each thickness value was recorded after 15 minutes of sputtering	37
Figure 3.4.	The schematic of the sputter deposition system. The positively charged Ar ⁺ ions hit to target/cathode and the neutrally ejected target atoms stick to the substrate.....	39
Figure 3.5.	The basic features of an XRD experiment	42
Figure 3.6.	Bragg-Brentano diffractometer. The point F is either the focal point of the monochromator or the focal point on an X-ray tube	43
Figure 3.7.	The diffraction at ideal (left) and non ideal (centre) conditions. The effect of the finite size of the crystal on diffraction is seen on the right.....	44
Figure 3.8.	The schematic describing the operation of an SEM.....	46
Figure 3.9.	The image of the SEM, located at Central Laboratory.....	46
Figure 3.10.	A typical EDS spectrum of Al ₂ O ₃ sputtered films with Si nanocrystals. C peak is from the surface due to contamination	47
Figure 3.11.	An illustration of the photoemission phenomenon in XPS	49
Figure 3.12.	Specs 200 XPS, located at Central Laboratory (a) General view, (b) process chamber and (c) electron analyzer	50

Figure 3.13.	Possible excitation and recombination mechanisms between the conduction and valence bands of semiconductors.....	52
Figure 3.14.	Possible light emitting mechanism of PL from Si-nc/SiO ₂ system: Left: pictorial illustration, right: energy levels including (1) recombination of electron-hole pairs in the nanocrystal, (2) radiative states at the interface between the nanocrystal and SiO ₂ matrix (3) luminescent defect centers due to the matrix defects.....	53
Figure 3.15.	The experimental PL setup used in this work	54
Figure 4.1.	Abbreviations used in coding the sample names.....	56
Figure 4.2.	The schematic diagram of the sputtered samples of (a) C52, (b) C55, (c) C22 and (d) C25	56
Figure 4.3.	XRD spectrum of the sample C22, annealed at different temperatures.....	59
Figure 4.4.	XRD spectrum of the samples annealed at 1000°C at different O ₂ partials and reference sample sputtered without O ₂	60
Figure 4.5.	X-ray diffraction data of the transition aluminas	61
Figure 4.6.	AFM images of C22, (a) as sputtered, (b) 900°C, (c) 1000°C and (d) 1100°C.....	64
Figure 4.7.	XPS spectrum of the sample C22, surface and beneath-surface measurements	67
Figure 4.8.	PL spectra of the sputtered samples, annealed at 1000°C for 1 hour.....	68
Figure 4.9.	PL spectra of the sputtered samples, annealed at 1100°C for 1 hour.....	69

Figure 4.10.	PL spectra of the sputtered sample C22, annealed at various temperatures for 1 hour.....	69
Figure 4.11.	The C-V curve of the Al ₂ O ₃ MOS capacitor before and after gamma irradiation at 1000 kHz	72
Figure 4.12.	Radiation induced charges for p-type SiO ₂ with 250 nm thick and Al ₂ O ₃ with 250, 500 and 750 nm thick MOS capacitors.....	73
Figure 5.1.	Abbreviations used in coding the sample names.....	75
Figure 5.2.	The schematics of the sputtered samples of (a) D5, (b) D7, (c) D10, (d) D12 and (e) D15	75
Figure 5.3.	XRD spectra of the samples (a) D5, (b) D7, (c) D10, (d) D12 and (e) D15	77
Figure 5.4.	XRD spectra of the samples D10, D12 and D15.....	78
Figure 5.5.	XRD peak fits around 2 θ =28.5° region of 150 W [(a) 900°, (b) 1000°, (c) 1100°]; 125 W [(d) 900°, (e) 1000°, (f) 1100°] and 100 W [(g) 1100°C] Si target power sputtered samples	79
Figure 5.6.	Variation in the nanocrystal size and elastic strain with respect to annealing temperature and Si DC-power	82
Figure 5.7.	PL Spectra of the samples. (a) D5, (b) D7, (c) D10, (d) D12 and (e) D15	84
Figure 5.8.	Flat band diagram of Al ₂ O ₃ summarizing the relative energy positions of F type centers at different charge states.....	85
Figure 5.9.	Variation of the PL emission spectra with respect to time.....	87
Figure 5.10.	PL depth profile of the 150 W sputtered and 1100°C annealed sample.....	88

Figure 5.11. XPS depth profiles of the as sputtered 150 W samples (a) O <i>1s</i> and (b) Si <i>2p</i>	90
Figure 5.12. XPS depth profiles of the 1100°C annealed 150 W samples (a) O <i>1s</i> and (b) Si <i>2p</i>	91
Figure 5.13. Deconvolution of Si <i>2p</i> signals of (a) as sputtered and (b) 1100°C annealed sample. Identical layers (17 th layers from the top surface) were chosen from Fig. 5.11 (b) and 5.12 (d). The effect of annealing was increased the Si and SiO ₂ density. Inset shows the raw data.....	93
Figure 5.14. The variation in the atomic concentrations and the PL intensity of the 1100°C annealed sample in Figure 5.13 with respect to sputter time and depth. The PL etching was referenced to the maximum of the main peak around 800 nm	95

LIST OF ABBREVIATIONS

AC	Alternating Current
AFM	Atomic Force Microscopy
CB	Conduction Band
CCD	Charge Coupled Device
CMOS	Complementary Metal Oxide Semiconductor
DC	Direct Current
DFT	Density Functional Theory
DOS	Density of States
EDS	Energy Dispersive X-ray Spectroscopy
FTIR	Fourier Transform Infrared
FWHM	Full-Width Half-Maximum
ICDD	International Centre for Diffraction Data
LDA	Local Density Approximation
LED	Light Emitting Diode
MOS	Metal Oxide Semiconductor
PL	Photoluminescence
RF	Radio Frequency
SEM	Scanning Electron Microscopy

UHV	Ultra High Vacuum
UV	Ultraviolet
VB	Valence Band
XPS	X-ray Photoelectron Spectroscopy
XRD	X-ray Diffraction

CHAPTER 1

INTRODUCTION

1.1 Introduction:

49 years ago, on December 29, 1959, a famous physicist who was known for his formulation of the path integral in quantum mechanics, and the theory quantum electrodynamics, was giving a talk at an American Physical Society meeting at Caltech. He was talking about “manipulating and controlling things on a small scale.” He was actually talking about a promising research area of physics, in which a great number of applications together with intense physical theories can be done. His words were truly describing his amazement on this area [1]:

“I would like to describe a field, in which little has been done, but in which an enormous amount can be done in principle. This field is not quite the same as the others in that it will not tell us much of fundamental physics (in the sense of, “What are the strange particles?”) but it is more like solid-state physics in the sense that it might tell us much of great interest about the strange phenomena that occur in complex situations. Furthermore, a point that is most important is that it would have an enormous number of technical applications.”

He was continuing his famous lecture about these words, which explains the behavior of “atoms in a small world”:

“... Atoms on a small scale behave like nothing on a large scale, for they satisfy the laws of quantum mechanics. So, as we go down and fiddle around with the atoms down there, we are working with different laws, and we can expect to do different things. We can manufacture in different ways. We can use, not just

circuits, but some system involving the quantized energy levels, or the interactions of quantized spins, etc.”

He was Richard P. Feynman, who gave this famous lecture under the title of “*Plenty of Room at the Bottom.*” At that time, he has just catalyzed the limited research on this applied physics area.

The original name of this applied physics area was given by Prof. Norio Taniguchi who was naming the processing and manipulating of materials on atomic scale as “nano-technology” [2]. Since then, the term nanotechnology is ultimately used for the “physics of small” and today, nanotechnology is turned out to be a multidisciplinary science including chemistry, biology, engineering and materials science on the base of solid state physics.

1.2 Plenty of Room at the Bottom:

When a material is downscaled to a certain size at least in one dimension, usually in the order of nanometers, the motion of electrons are restricted and confined along that side. This confinement results in a change in the physical properties of the material with respect to its bulk counterparts. Scientists have been challenging with the small scale of the materials in order to control the size, or physically, to control the properties. Fabrication of materials in small scale was also desirable for building more compact, more sensitive and more responsive devices for technological applications. When the first transistor was invented by Bardeen, Brattain and Shockley [3] in 1947, nobody can imagine the importance of this invention and the level we reached today. The empirical theory predicted by Intel co-founder Gordon Moore states that, the density and performance of integrated circuits doubles every two years, which is known as Moore’s law [4, 5]. As far as his predictions stand still, Feynman’s dreams will come true. Nowadays, transistors down to 30 nm can be fabricated and hundreds of millions of them can be put together to form an ensemble of synchronous working tiny machines, such as computer processors.

1.3 The Famous Trinity and Search for New Structures:

The reliability, performance and also cost of these tiny devices are mostly depending on the material used during fabrication. A typical integrated circuit contains individual metal-oxide-semiconductor (MOS) transistors which are used to amplify or switch the electronic signals. Si is used as the semiconductor, its natural oxide SiO_2 is used as the dielectric and Al is used as the metal layer in these structures. Today, the microelectronic industry is based on this famous trinity of Si/ SiO_2 /Al system shown in Figure 1.1.

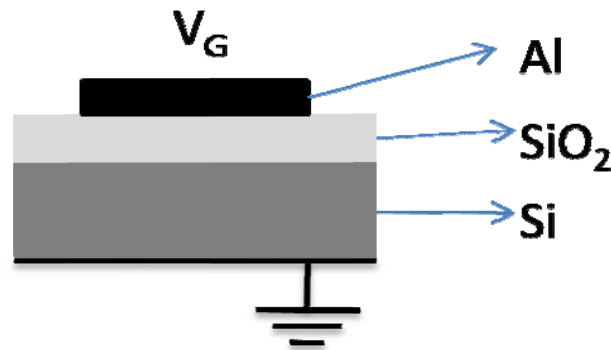


Figure 1.1. A typical MOS capacitor.

MOS type structures can be used for different purposes such as FLASH memory and LED applications. In these structures, a floating Si layer is inserted in the oxide, which is used for memory element (Figure 1.2). Charge can be injected or ejected from the tunneling oxide layer. The responsible transport mechanism from injecting and removing charges is Fowler-Nordheim tunneling [6]. This structure is well defined and used nowadays extensively. However the big drawback of these structures is to prevent leakage current through tunneling oxide. In the case of a leakage, the floating gate is shorted and all the information is lost.

For LED applications, GaAs and InP are used widely due to their high luminescence efficiency. Unfortunately, these materials prevent the production of Si based photonic components integrated with the electronic circuits [7]. So it is an important issue to get efficient light emission from Si itself, if so, the optic and electronic components in a circuit can be fabricated from the same material. However, Si is an indirect band gap material, in which direct absorption of photons cannot be possible (Figure 1.3). In order to absorb a photon, a suitable photon-phonon interaction is needed. The poor light emitting property of bulk Si is due to the non radiative recombination centers such as free carrier absorption, Auger recombination, defect and trap assisted recombination. The solution of this problem is to turn Si into an efficient light emitter to fabricate reliable, efficient and cost effective optic and optoelectronic devices.

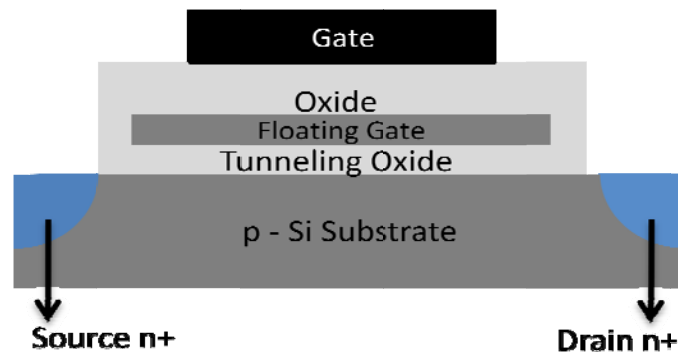


Figure 1.2. Schematic diagram of a conventional floating gate FLASH memory cell.

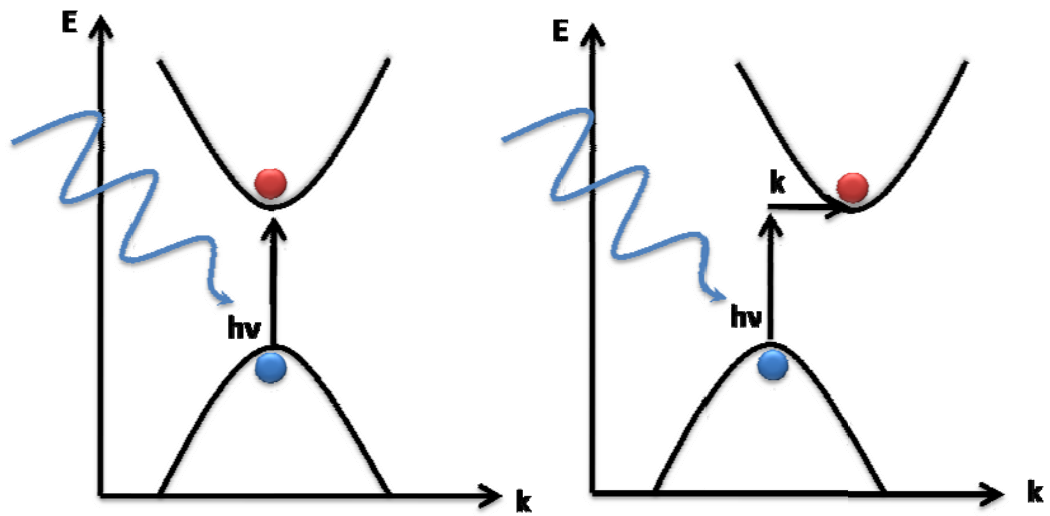


Figure 1.3. Direct and indirect absorption in semiconductors.

As a quantum structure, nanocrystalline Si exhibits different electrical and optical behavior with respect to bulk Si due to quantum size effect [8]. In recent years, it is found that, nanocrystal Si imparted in dielectric matrices may be an alternative to classical FLASH memory cells and also it may be an efficient light emitter.

1.3.1. Nanocrystal Based FLASH Memory Cells, LEDs and Solar Cells:

Recent developments showed [9, 10] that nanocrystals of Si and Ge can be used to fabricate memory cells which are alternative to classical ones (Figure 1.4). In nanocrystal based FLASH devices, a small leakage current through the tunneling oxide does not result in a total loss of the information, but instead, only a few of the nanocrystals may be shorted. Instead of a single sheet of charge, dot-like charges are more reliable and faster. Recently nanocrystal based memory elements have been reported [11 12] and simulated [13] in silicon oxide.

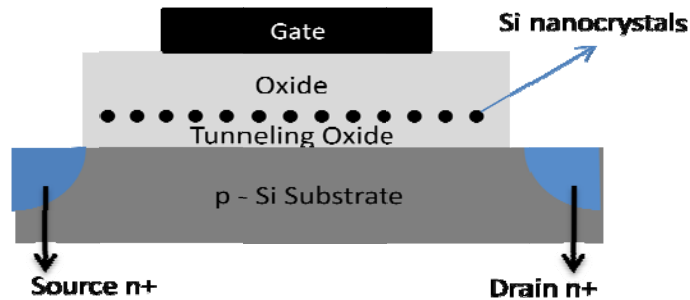


Figure 1.4. Si nanocrystal based FLASH memory device.

Observation of intense photoluminescence from Si nanocrystals [14] has created new excitements for the development of new optical and electro-optical components such as LEDs [15, 16] and waveguides [17]. The internal photoluminescence quantum efficiency of Si nanocrystals was found to be around 60% [18] and the external quantum efficiency was found to be 4.5% [19]. The non radiative recombinations due to the defects are decreased in the nanocrystals formed in a passivating dielectric matrix. The increase in the PL efficiency will make way to new generation Si nanocrystal based LEDs [20].

The quantum confinement effect of Si nanocrystals can be used in advantage of catching a wider range solar absorption. In thin film and bulk solar cells, absorption can occur only at the band gap energy of the material and the remaining wavelengths are totally lost. Figure 1.5 [21] demonstrates the possible energy loss mechanisms in a first and/or second generation solar cell. In order to create a current, the electrons and holes should be generated at the junction and they should be separately collected.

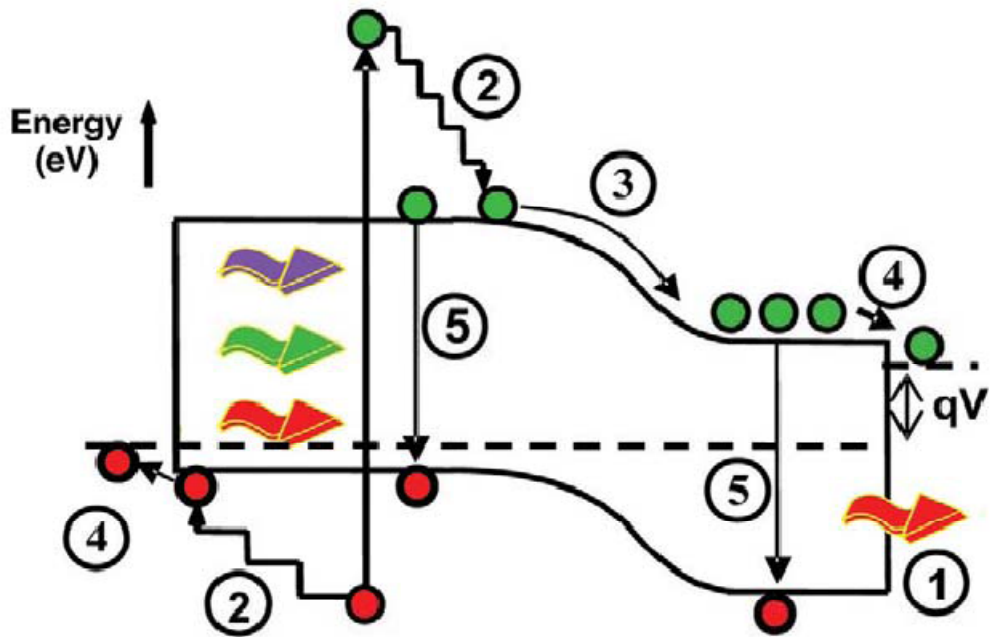


Figure 1.5. Loss processes in a standard solar cell: (1) non-absorption of below band gap photons; (2) lattice thermalization loss; (3) and (4) junction and contact voltage losses; (5) recombination loss. Adopted from Ref. 21.

When a lower energy photon is incident on the junction, it cannot be absorbed and does no effect on electron-hole pair creation. Inversely, a high energy photon, which is well above the band gap energy is absorbed and the excess energy is thermalized which in turn heats the cell. The loss mechanism can also take part in junctions and contacts that result in a decrease in the total efficiency. Another unavoidable loss mechanism is the instant recombination of the generated electron-hole pairs.

If a multilayer tandem solar cell containing different sizes of nanocrystals at each layer is fabricated, multiple energy regions of the solar spectrum can be absorbed and this increases the efficiency of the solar cell (Figure 1.6) [22]. Recently,

single layer nanocrystal solar cells at efficiency 10% have been reported [23]. However, Schokley - Quessier limit allows up to 87% efficiency and at ideal conditions (zero contact resistance and infinite mobility) up to 100% efficiency can be reached for third generation tandem solar cells. With these promising properties, Si nanocrystals are very suitable for energy conversion for photovoltaic applications.

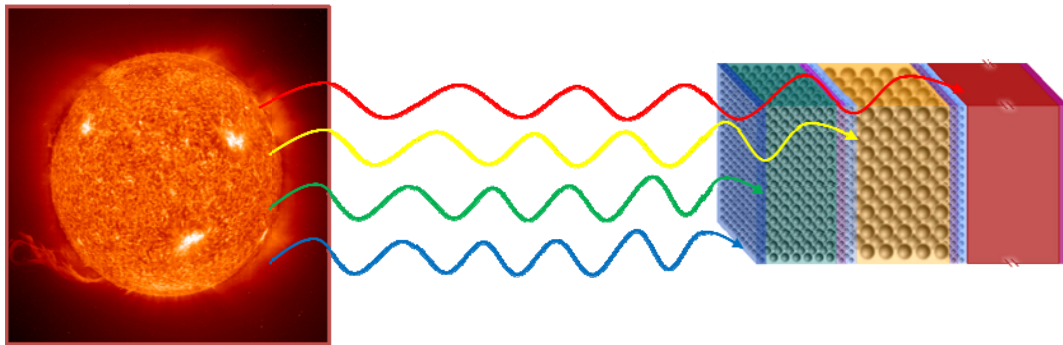


Figure 1.6. Third generation multiple band gap nanocrystal tandem solar cells. Adopted from Ref. 22.

1.3.2 Al_2O_3 as an Alternative Host Matrix for Si Nanocrystals:

To date, the most widely used dielectric host matrix to Si nanocrystals was SiO_2 . This matrix has been extensively studied [24 - 26] due to its importance and wide use in microelectronic components. The advantages of SiO_2 are that it is the natural oxide of Si, it has a relatively large dielectric constant and it can be grown on Si thermally. With the shrinking dimensions however, there is a limit to the thickness of this dielectric layer in MOS devices for reliable device operations.

Search for alternative materials having similar properties to that of SiO₂ and higher dielectric constant has been intensified in recent years. Aluminum oxide (Al₂O₃) appears to be a good candidate for this purpose as it has a larger dielectric constant compared to that of SiO₂ [27]. Furthermore, due to optical transparency, Al₂O₃ is an ideal host material for optical devices including solar cells. The visible photoluminescence from Si nanocrystals formed in Al₂O₃ matrix has been reported previously [28]. Since then, a number of research groups have studied this system [27, 29].

1.4 Overview of the Dissertation:

This dissertation will attempt to demonstrate the formation of Si nanocrystals in an alternative dielectric matrix, namely Al₂O₃. It is shown that, as long as the stoichiometry of the Al₂O₃ is sustained, this dielectric layer can be used in MOS type devices, such as radiation dosimeters, or sensing layers. Moreover, under certain conditions of sputtering and post annealing, an efficient light emission in the near infrared part can be obtained from Si nanocrystals formed in the Al₂O₃ matrix. Main topics of this study are divided into six chapters and these chapters will rely on a part of the entire body.

CHAPTER TWO gives theoretical knowledge and some physical properties of Al₂O₃ and Si nanocrystals. Density Functional Theory and Local Density Approximation to electronic band diagram of Al₂O₃ and surface-interface defect nature of the Si nanocrystals will be demonstrated.

CHAPTER THREE provides a description of the experimental techniques used in the fabrication and characterization of the materials.

In CHAPTER FOUR, formation and characterization of stoichiometric Al₂O₃ films will be demonstrated. Al₂O₃ thin films were sputtered with different parameters in order to find the stoichiometry, and with the best parameters, a

MOS device was fabricated to investigate the sensitivity under radiation with compared to SiO₂ based MOS radiation sensors.

In CHAPTER FIVE, formation and characterization of Si nanocrystals in aluminum oxide matrix was demonstrated. Different DC-powers were applied to Si target at each run, with the aim of producing different size nanocrystals and detect size dependent PL emission. X-ray photoelectron spectroscopy depth profile studies were conducted to investigate the chemical structure of the film. The formation of Si nanocrystals in some samples was tailored by x-ray diffraction experiments. Size calculation of Si nanocrystals was also performed.

Finally in CHAPTER SIX, some final words and conclusions are provided. Some future direction to these materials is also discussed.

CHAPTER 2

STRUCTURAL AND THEORETICAL APPROACH TO Al₂O₃ AND Si NANOCRYSTALS

2.1 Introduction

Aluminum oxide (Al₂O₃) is probably the most important ceramic material that has wide range of applications from metallurgy to electronics and optics to nanotechnology. During the recent development and research, Al₂O₃ has become an indispensable material to these areas due to its superior mechanical, chemical and thermal properties. Being a wide band gap and high-*k* material, aluminum oxide is suitable in microelectronics as alternative gate oxides [30], in integrated optics as low-loss dielectric waveguides [31], in nanotechnology as a host material within the context of nanocrystals [32]. In fact, the concept of different wide gap high-*k* materials as host matrices for nanocrystals has become an active research topic in silicon based technology. Among these materials, aluminum oxide is the most suitable material to be replaced with SiO₂, the ultimate oxide material in silicon based technology. Moreover, in optical applications, the impurities and defects in aluminum oxide should be well understood in order to control their emission properties in the matrix. Due to these facts, the knowledge about the physical properties of aluminum oxide is crucial for better understanding of this material and for expanding possible range of applications.

In this section, a theoretical background about the physical, optical and electronic properties of aluminum oxide will be given. The main theoretical model focused here is density functional theory for band calculations. Quantum mechanical

aspects of nanocrystal formation and size dependence of the physical properties at the confinement regime will also be considered.

2.2 Properties and Theoretical Background about Aluminum Oxide (Al_2O_3):

2.2.1 Crystallographic Properties:

In nature, Al exists in crystalline oxides and the natural, colorless and transparent crystalline aluminum oxide is named as alumina (Al_2O_3). Al_2O_3 is an inorganic-solid chemical compound, whose formation occurs by geological processes in different kind of rocks hence, it is a mineral and has a specific name; corundum. The corundum structure is named as alpha-alumina ($\alpha\text{-Al}_2\text{O}_3$) [33] with a rhombohedral unit cell containing two Al_2O_3 molecules (space group D_{3d}^6 or $R\bar{3}C$). The crystal structure is hexagonal, containing six Al_2O_3 molecules as shown in Fig. 2.1 [34]. The crystal parameters of $\alpha\text{-Al}_2\text{O}_3$ are shown in Table 2.1 [35].

There also exist five crystalline aluminum hydroxides which are named as gibbsite, bayerite, nordstrandite, diaspore and boehmite [36]. The dehydroxilation of these species occurs by heating them with different temperatures between 300 and 600°C which at last, different transition aluminas are formed [37]. These transitions aluminas are formed through dehydroxilation to alpha-alumina crystallization temperature (1100°C), each of which has a stable crystalline structure [36].

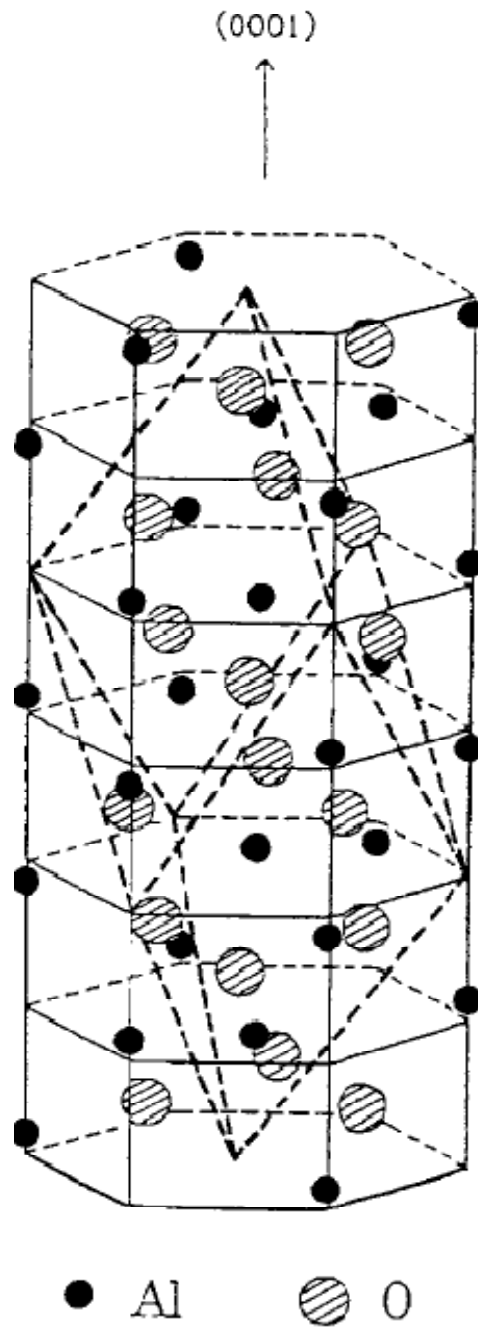


Figure 2.1. Crystal structure of α - Al_2O_3 in hexagonal lattice. Adopted from Ref. 34.

Table 2.1. Comparison of the crystal structures of α -Al₂O₃ (Space group $R\bar{3}C$).
Adopted from Ref. 35.

Hexagonal	
a (Å)	4.762
c (Å)	12.896
c/a	2.727
Trigonal	
a (Å)	5.128
α	55.333°
Unit cell volume (Å ³)	255.039
Al–O bonds (Å)	
(3)	1.857
(3)	1.969
Al–Al dist. (Å)	
(1)	2.649
(3)	2.792
O–O dist. (Å)	
(2)	2.524
(2)	2.619
(4)	2.725
(4)	2.869

There are seven synthetic transition aluminas which receive Greek letters to be identified: gamma, delta, theta, kappa, chi, eta and rho (Fig. 2.2) [38]. As it is seen from Fig. 2.2, α -Al₂O₃ is not a transition alumina; it is the last crystalline material to be reached when the transition forms are annealed up to 1100°C. In fact, the phase transformation of aluminas is not reversible. None of the high temperature transition aluminas can be converted to any low temperature aluminas. Therefore, thermodynamically more stable aluminas are the ones formed at higher temperatures.

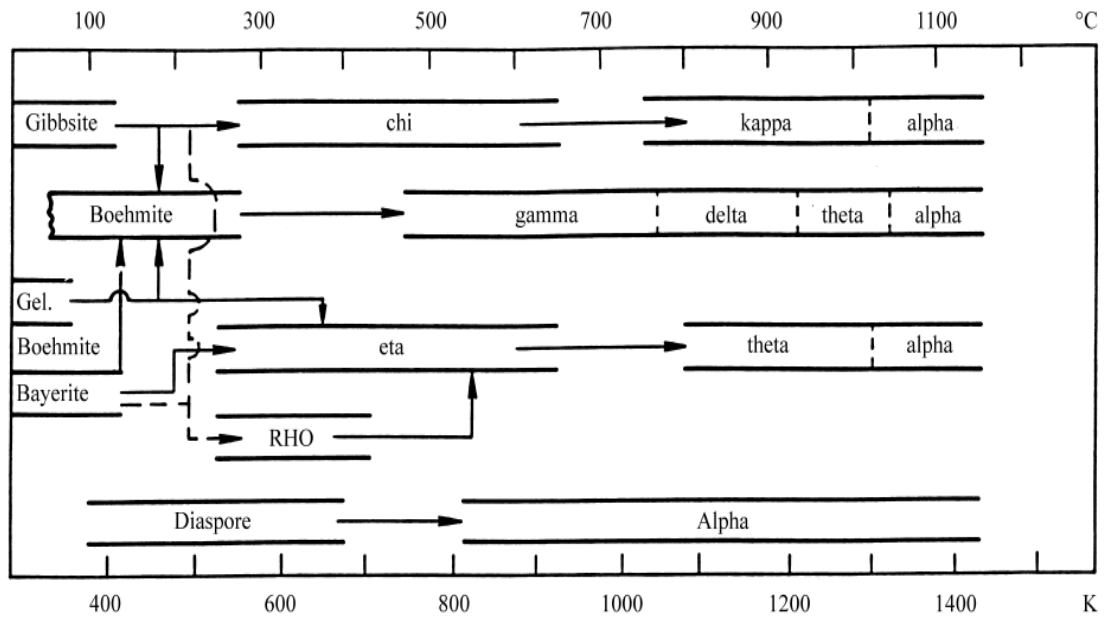


Figure 2.2. Thermal transformation pathway of different aluminum hydroxides Adopted from Ref.38.

Fig. 2.3 shows the X-ray powder data of the transition aluminas. Note that the transition aluminas give well defined peaks, which therefore, implies these transition forms are also crystalline in structure. The structural changes and increasing stability with temperature are also tailored from the figure.

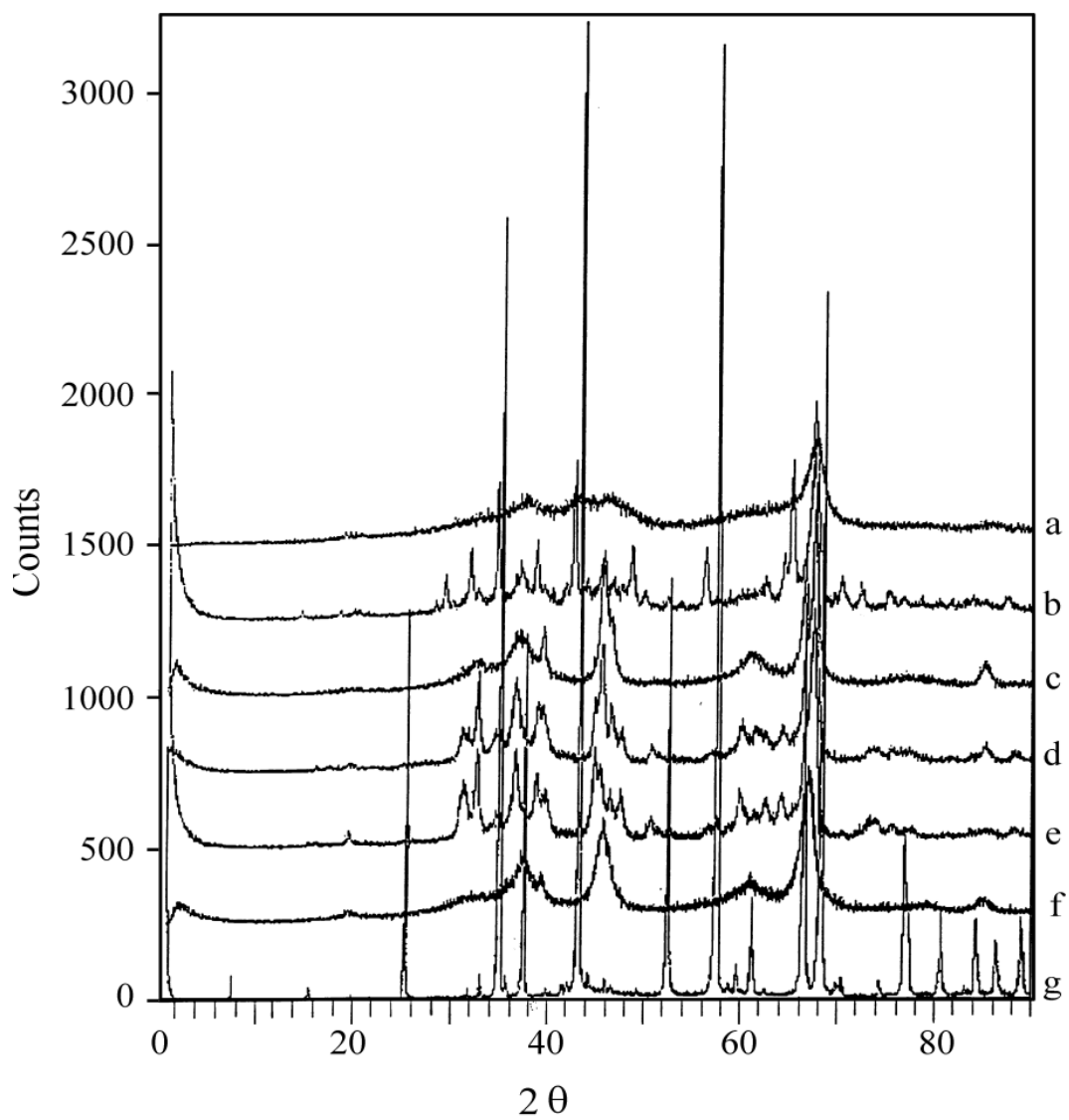


Figure 2.3 X-ray diffraction powder curves of (a) chi-Al₂O₃, (b) kappa-Al₂O₃, (c) gamma-Al₂O₃, (d) delta-Al₂O₃, (e) theta-Al₂O₃, (f) eta-Al₂O₃, (g) α-Al₂O₃ Adopted from Ref. 37.

2.2.2 Optical and Electronic Properties:

Optical and electronic properties of Al_2O_3 are influenced by its crystal structure, crystal defects, grain boundaries and interface defects which are critical in macroscopic applications. Therefore, it is of interest to know and control the electronic band structure and optical constants quite well. In solid state theory, there are numerous theoretical formalisms to define the band structure and optical constants of many body systems, molecules and atoms. In this section, a theoretical approach will be given to band structure and optical constants of solids, specifically Al_2O_3 .

2.2.2.1 Electron Band Structure - Density Functional Theory:

The widely used theoretical approach to simulate the behavior of many body systems is density functional theory (DFT) which is a quantum mechanical theory used in physics and chemistry to investigate the ground state of many body systems. The history of DFT dates back to the works of Thomas (1927) and Fermi (1928) [39] and the theory has been given a firm formalism by Hohenberg, Kohn and Sam [40, 41]. Different from Hartree-Fock model which based on complicated many electron wave functions; DFT uses the electronic density of states as basic quantity. If we take $\Psi_i(\vec{r})$, the one electron wave function, we can find the electronic density as,

$$n(\vec{r}) = \sum_{i=1} \Psi_i^*(\vec{r}) \Psi_i(\vec{r}) \quad (2.1)$$

where the energy Hamiltonian includes the kinetic and potential terms:

$$H = -\frac{\hbar^2 k^2}{2m} + V(\vec{r}) \quad (2.2)$$

If the effect of the potential on one electron is known $n(\vec{r})$ can be estimated. If $n(\vec{r})$ is expressed directly in terms of the potential $V(\vec{r})$, one electron wave function need not to be calculated, and this was what Thomas and Fermi have done. This idea was the starting point of the density functional theory.

In Thomas Fermi model, an N electron system interacting each other is defined by its local density $n(\vec{r})$ in an external electrostatic potential $V_a(\vec{r})$. The total energy functional of a system in terms of electron density can be given as,

$$E[n] = \int n(\vec{r})V_a(\vec{r})d\vec{r} + \frac{1}{2} \int \frac{n(\vec{r})n(\vec{r}')}{|\vec{r}-\vec{r}'|} d\vec{r} d\vec{r}' + \frac{3}{10} (3\pi^2)^{2/3} \int n^{5/3}(\vec{r})d\vec{r} \quad (2.3)$$

Where the first term represents the external potential energy, the second term represents the Coulomb potential energy of the electrons and the third term represents the total kinetic energy of the system. Since this model does not contain the exchange and correlation contributions, it has deficiencies when estimating the total energy functional. Dirac (1930) was introduced the exchange energy E_x to the Equation 2.3 to give a more satisfactory estimation and the Equation 2.3 is turned out to be

$$E[n] = \int n(\vec{r})V_a(\vec{r})d\vec{r} + \frac{1}{2} \int \frac{n(\vec{r})n(\vec{r}')}{|\vec{r}-\vec{r}'|} d\vec{r} d\vec{r}' + \frac{3}{10} (3\pi^2)^{2/3} \int n^{5/3}(\vec{r})d\vec{r} \quad (2.4)$$

$$+ \frac{3}{4} \left(\frac{3}{\pi}\right)^{1/3} \int n^{4/3}(\vec{r})d\vec{r}$$

In Equation 2.4, the lastly added term represents E_x and the approximation is called as Thomas-Fermi-Dirac approximation. One step further, the correlation energy was introduced by Gombás (1943) and the final form of the form of the formalism is Thomas-Fermi-Dirac-Gombás approximation.

The base of the DFT resides on the work of Hohenberg and Kohn (1964). In the Hohenberg-Kohn model, the ground state energy of a many body system under an external potential $V_a(\vec{r})$ is defined as a function of energy density $n(\vec{r})$:

$$E\left[n(\vec{r})\right] = \int n(\vec{r})V_a(\vec{r})d\vec{r} + F\left[n(\vec{r})\right] \quad (2.5)$$

The first term, external potential energy, is considered as constant and the variable term $F[n]$ contains the kinetic, Coulomb, exchange and correlation energies. At a given $V_a(\vec{r})$, $E[n]$ is minimized by the ground state density, with a conserved number of interacting electrons.

$$F[n] = \frac{1}{2} \int \frac{n(\vec{r})n(\vec{r}')}{|\vec{r}-\vec{r}'|} d\vec{r} d\vec{r}' + G[n] \quad (2.6)$$

Equation 2.6 separates the Coulomb interaction potential energy and yields a new universal functional $G[n]$; containing the kinetic, correlation and exchange terms. Hohenberg –Kohn model predicts a gradient expansion to $G[n]$, which includes the kinetic energy density $t_s(n)$, exchange energy density $e_x(n)$ and correlation energy density $e_c(n)$.

Kohn and Sham (1965) introduced a new approach to $G[n]$, given as:

$$G[n] = T_s[n] + E_{xc}[n] \quad (2.7)$$

The striking thing here is that $T_s[n]$ defines the kinetic energy of *non-interacting* electrons. By inserting Equation 2.7 into 2.6 and 2.5 a resultant effective potential can be defined as,

$$V_{eff}(\vec{r}) \equiv \frac{\delta}{\delta n(\vec{r})} (E[n] - T_s[n]) \quad (2.8)$$

It is clear that $V_{eff}(\vec{r})$ is a functional of electron density $n(\vec{r})$. Assuming an effective potential $V_{eff}(\vec{r})$, an approximation to electronic density of states can be estimated. Further expanding of the $E_{xc}[n]$ functional in a series of density gradients and omitting the higher order terms results in the most sophisticated approximation, called as local density approximation (LDA) [42].

When calculating the energy band diagram of solids, DFT and LDA give quite satisfactory results. However, there are still some deficiencies which give different results compared to experiments, which are due to the *ground state* calculations and to the approximations in the higher order gradient terms of functionals.

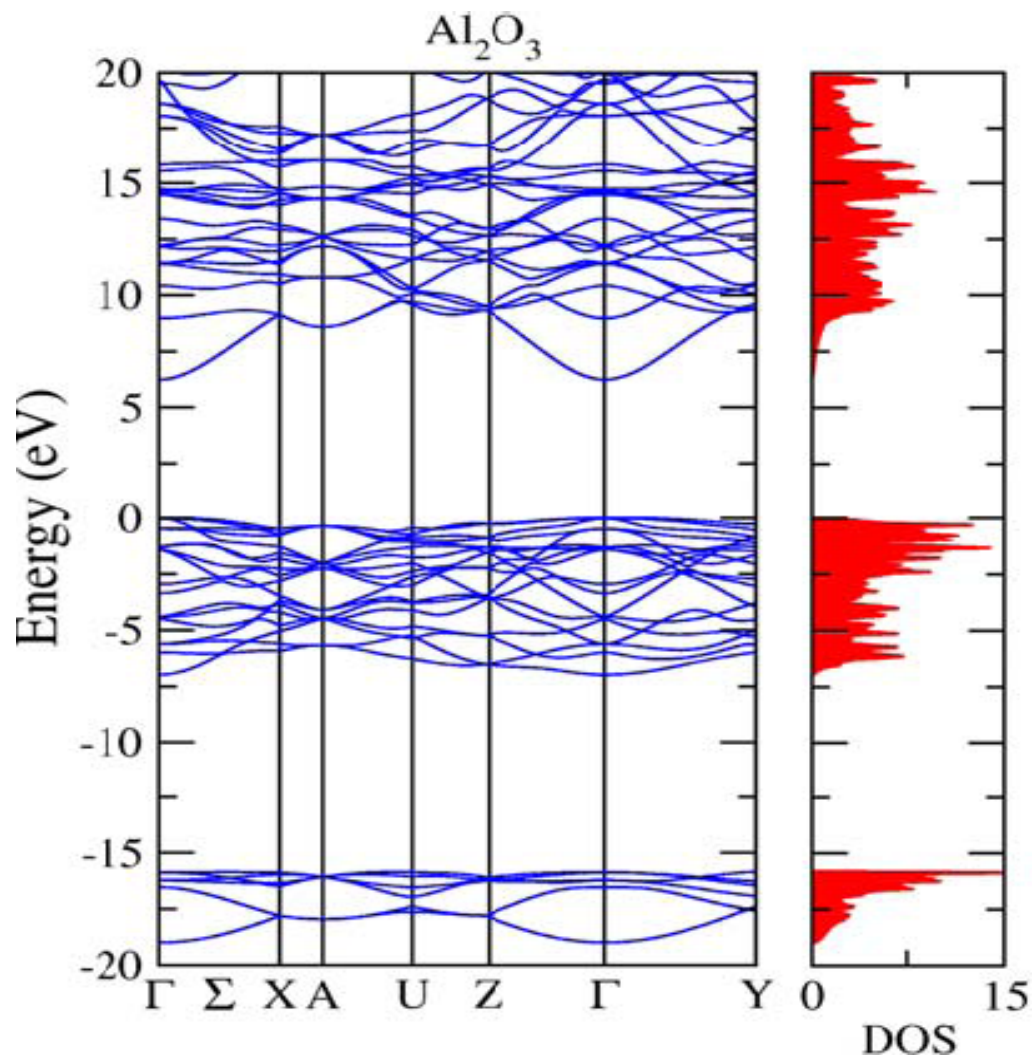


Figure 2.4. LDA band structure and total DOS of $\alpha\text{-Al}_2\text{O}_3$. Adopted from Ref. 43.

Figure 2.4 gives the LDA band structure of α -Al₂O₃ which is calculated as 6.30 eV [43]. Roughly, α -Al₂O₃ can be considered as a direct band gap insulator. As it is seen from the figure, the density of states (DOS) of valence band increase more abrupt than conduction band. Since the scattering probability of the charge carriers is directly proportional to the DOS, holes are scattered much more than electrons.

Table 2.2 gives the electron and hole effective masses for alpha- theta and kappa-Al₂O₃ with respect to different crystal directions. For α -Al₂O₃, the electron effective mass is much lighter than the effective mass of holes, resulting the fact that the majority charge carriers in α -Al₂O₃ are electrons [44].

Table 2.2. Electron and hole effective masses of different aluminas.

	Space group	Z	$\langle D_{Ca-O} \rangle$	Ca n.n.	$\langle D_{Al-O} \rangle$	Al n.n.	E_g	VBW	$m_e^{[100]}$	$m_e^{[010]}$	$m_e^{[001]}$	$m_h^{[100]}$	$m_h^{[010]}$	$m_h^{[001]}$
α -A	$R\bar{3}c$	2	—	—	1.91	6	6.48	7.1	0.38	0.38	0.38	3.99	3.99	3.99
θ -A	$C2/m$	2	—	—	1.77, 1.93	4, 6	4.95	6.4	0.41	0.41	0.37	0.64	0.64	13.68
κ -A	$Pna2_1$	8	—	—	1.77, 1.94	4, 6	5.49	6.6	0.37	0.35	0.36	4.90	6.22	0.47

Calculated total and orbital resolved partial DOS of α -Al₂O₃ are given in Figures 2.5 and 2.6, respectively [34]. As seen from Figure 2.5, the total DOS are mostly occupied by O in the conduction and upper valence band. The resolved partial DOS of α -Al₂O₃ shows that the conduction band is mostly occupied by O 2s and Al 3d orbitals while the upper valence band is occupied by O 2p and the lower valence band is occupied by Al 2p and 3d orbitals.

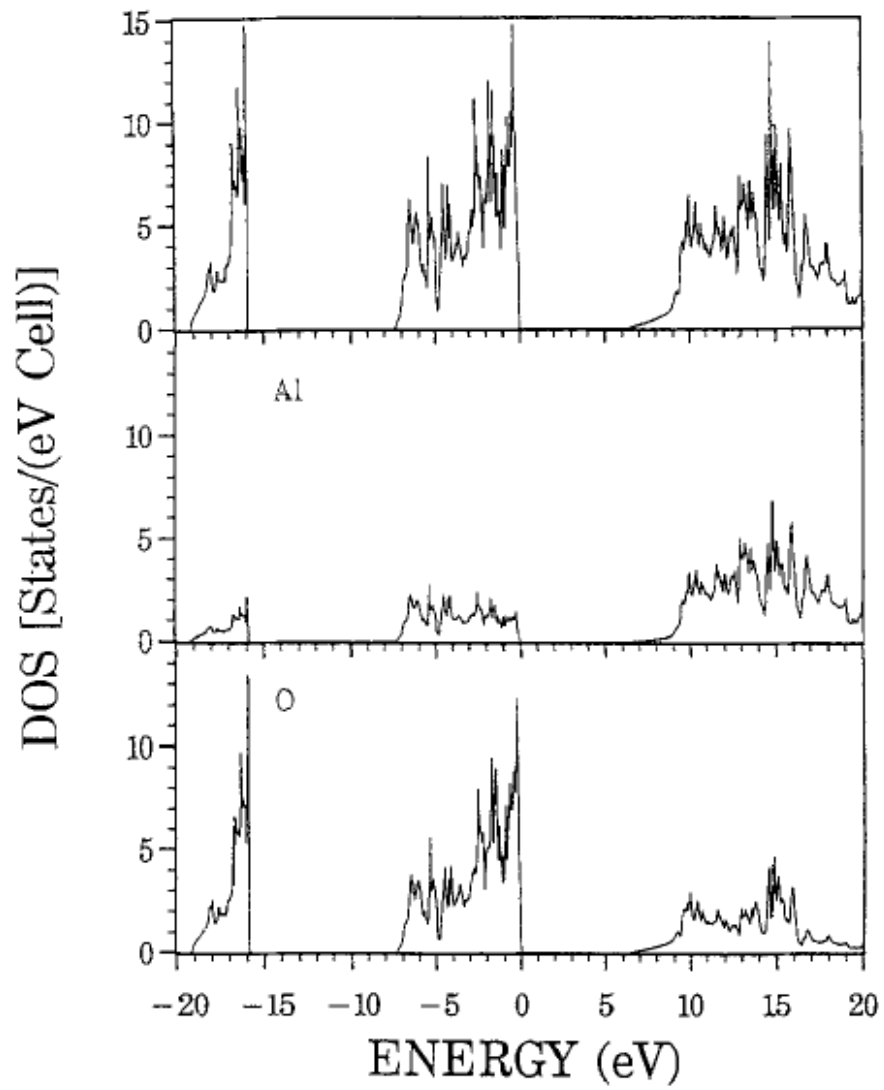


Figure 2.5. Calculated total and partial DOS of $\alpha\text{-Al}_2\text{O}_3$. Adopted from Ref. 34.

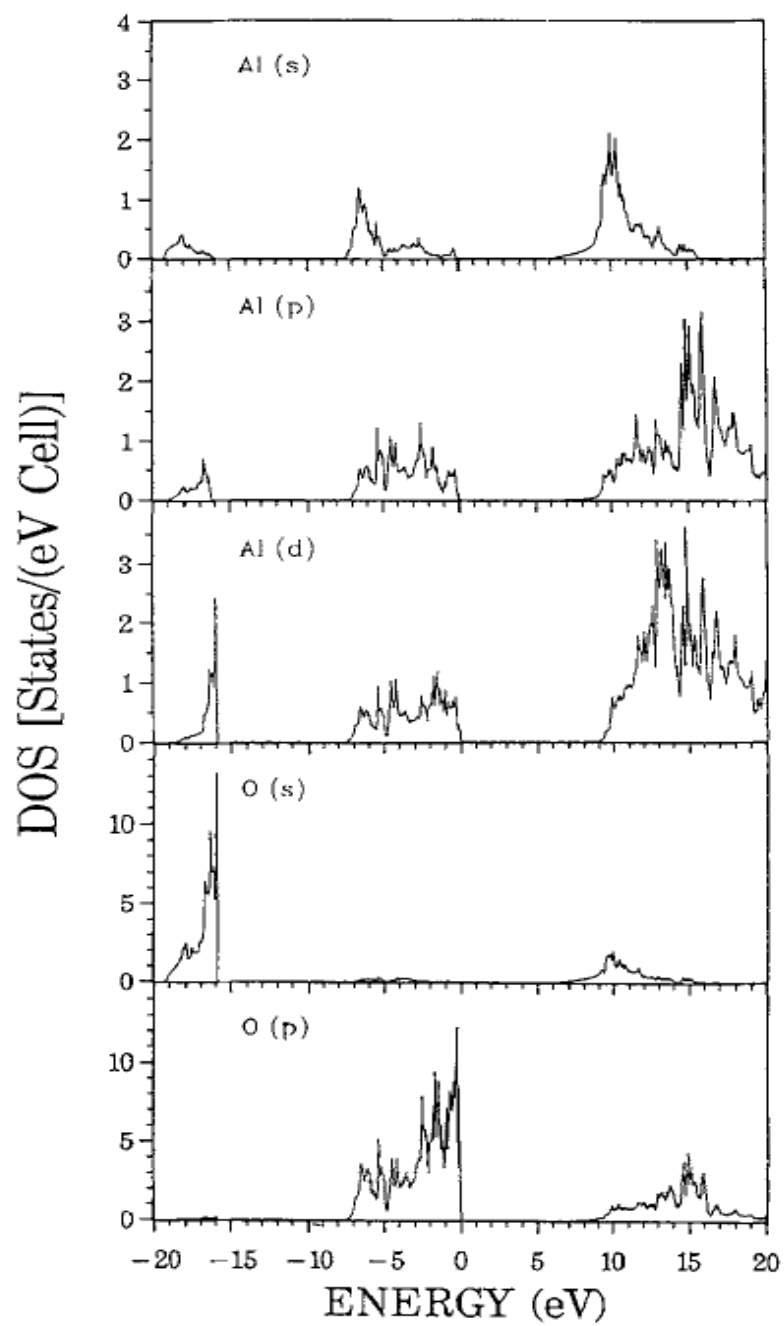


Figure 2.6. Calculated orbital-resolved partial DOS of α -Al₂O₃. Adopted from Ref. 34.

2.2.2.2 Optical Constants:

As mentioned at the beginning of Section 2.2.2, crystal defects, grain boundaries and interfaces are of critical importance in applications of Al₂O₃ and affect its optical properties. The optical properties of materials are composed of real and imaginary parts, so they have complexity. The transformation of the experimental data into complex variables is done by using the Kramer's Kröning dispersion analysis.

The reflectance, R , of a solid is related to the index of refraction, n , according to the following formula

$$R(E) = \frac{(n-1)^2 + k^2}{(n+1)^2 + k^2} \quad (2.9)$$

Here E is the energy and k is the extinction coefficient [45]. As a whole, the index of refraction is complex, $n + ik$, and it is related to the complex dielectric constant,

$$\varepsilon = \varepsilon_1 + i\varepsilon_2 = (n + ik)^2 \quad (2.10)$$

The Kramer's Kröning analysis of the reflectance gives us the reflected phase, Φ , of the light from the reflectance amplitude, ρ :

$$\Phi(E) = -\frac{2E}{\pi} P \int_0^{\infty} \frac{\ln \rho(E')}{E'^2 - E^2} dE' \quad (2.11)$$

where P is the Cauchy principal value. The complex reflectance \hat{R} can be found by adding the Equations 2.9 and 2.11 consecutively,

$$\hat{R}(E) = R(E) + i\Phi(E) \quad (2.12)$$

$$\frac{n - 1 + ik}{n + 1 + ik} = \rho(E)e^{i\theta E} \quad (2.13)$$

The complex index of refraction and all other related optical properties can be found from Equation 2.13 and by using theoretical calculations, the refractive index of Al₂O₃ is found to be 1.96 and experimental results give a value of 1.77.

Figure 2.7 shows the reflectance of single crystalline α -Al₂O₃ determined by UV/visible spectroscopy. The similarity of the general behavior of the reflectance with DOS of conduction band is worth noting. The mobile carriers are electrons in the conduction band, so the increasing density of electronic states in the conduction band increases the reflectance. The LDA band gap edge is clearly noticed from the figure since at the gap region the reflectance is minimized and constant, and at the conduction band minimum indicates a dramatic increase of the reflectance.

Transmittance spectrum of α -Al₂O₃ is given in Figure 2.8. As seen from the figure, crystal α -Al₂O₃ is almost transparent to visible light and this property makes Al₂O₃ suitable for optical device applications.

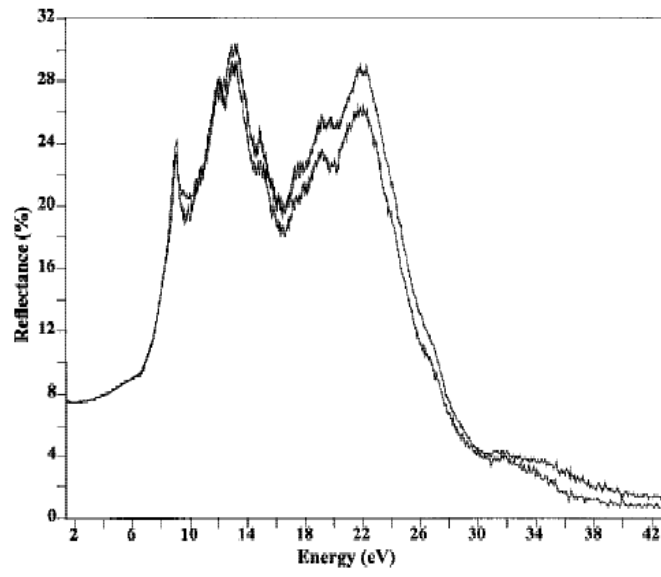


Figure 2.7 Reflectance of single crystalline α - Al_2O_3 . Adopted from Ref. 45.

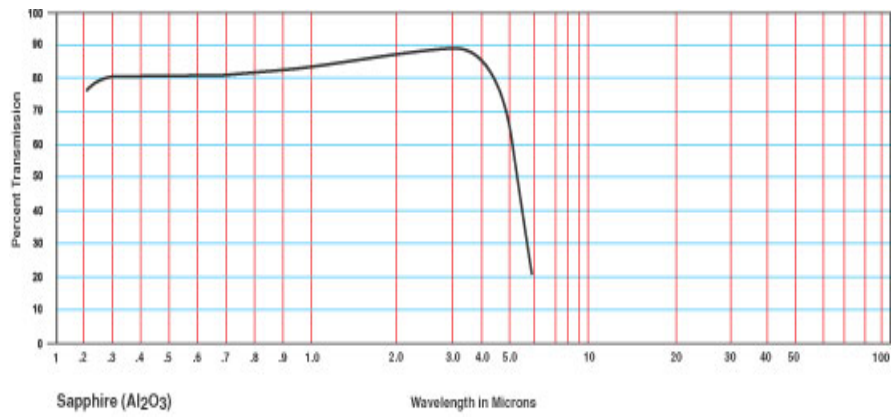


Figure 2.8. Transmittance spectrum of α - Al_2O_3 .

2.3 Nanocrystals – Quantum Mechanical Aspects:

Quantum dots (or nanocrystals), which are tiny structures in the order of nanometer size, do not exist in nature, but created artificially. Their size is usually smaller than 100 nm. The physics used for understanding the properties of nanocrystals includes some kind of approaches on three dimensional spatial confinement of electron motion. The electronic energy levels in nanocrystals are atom-like; they are quantized due to the confinement of electrons (Fig. 2.9). The conduction band (E_c) and the valence band (E_v) split into overlapping sub bands that become narrower as the electron motion is restricted in more dimensions [46]. The electron and hole energy states within the nanocrystal are function of nanocrystal diameter. As the size decreases, the Coulomb potential exerted on confined electrons also decreases. As a result, the difference between the energy states becomes larger. In the same way, an increase in the diameter results in an energy decrease between the states. Since the electronic and optical properties of materials strongly depend on the electronic configuration, intentional differences can be created by varying the size of a nanocrystal.

The physical results of nanocrystals and their analytical expressions can be revealed by two cases, the so called weak confinement and strong confinement [47].

2.3.1 Weak Confinement:

Weak confinement corresponds to the situation in which the dot size “a” is a few times larger than the exciton Bohr radius “ a_B ”. In weak confinement regime, the quantization of the exciton center of mass motion occurs. The energy of exciton in this case is described by the following formula:

$$E_{nml} = E_g - \frac{R_y^*}{n^2} + \frac{\hbar^2 \chi_{ml}^2}{2Ma^2} \quad (2.14)$$

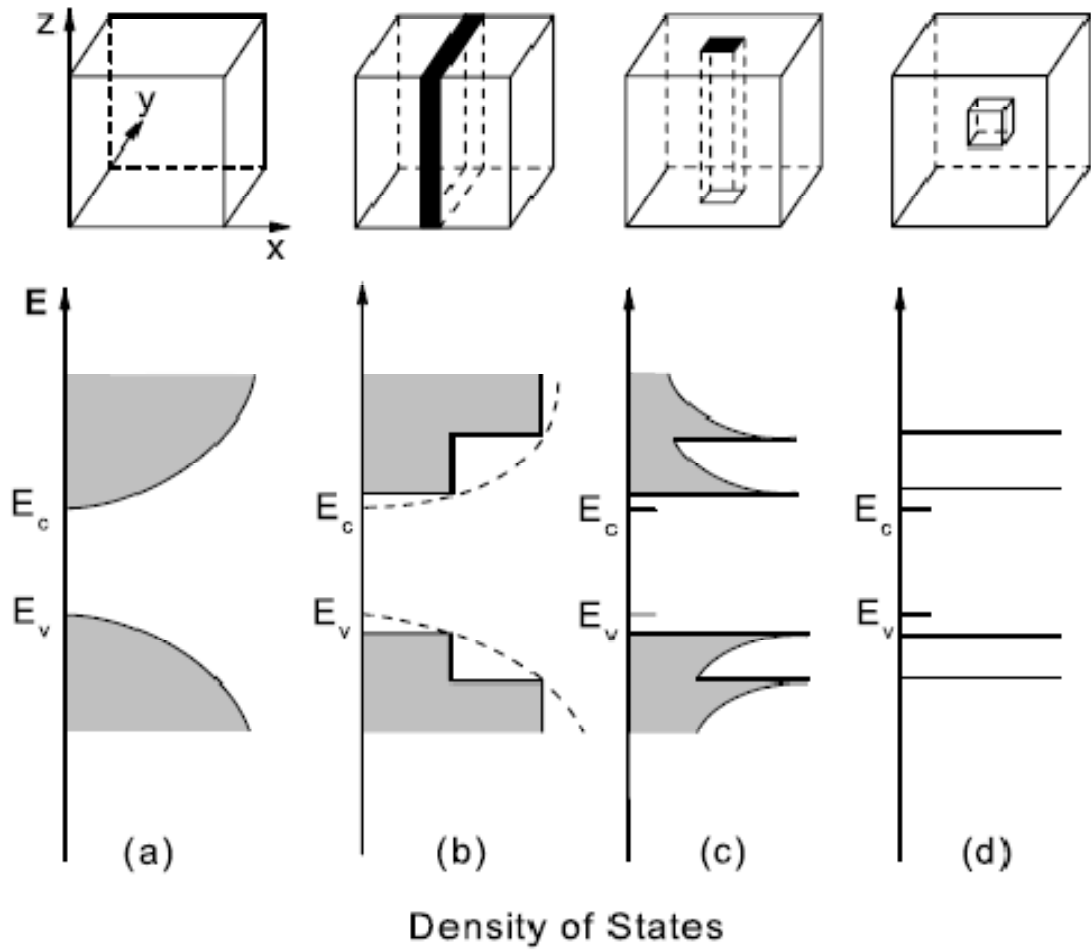


Figure 2.9. The density of states of carriers in different confinement configurations (a) bulk, (b) quantum well, (c) quantum wire, (d) quantum dot.

Where the first term is the band gap energy, the second term is the exciton Rydberg energy at the confinement limit and the last term is the quantized exciton energy in spherical box. The internal excitons in a quantum dot directly depend on the quantum number n arising from the Coulomb electron-hole interactions (1S, 2S, 2P...). m and l describes the states connected within the exciton center of mass motion (1s, 2s...) under the effect of external conditions. For the lowest case ($n=1, m=1, l=0$), the energy of the exciton turns out to be;

$$E_{1S1s} = E_g - R_y^* + \frac{\pi^2 \hbar^2}{2Ma^2} \quad (2.15)$$

And R_y^* is defined as;

$$R_y^* = \frac{\mu e^4}{2\epsilon^2 \hbar^2} \quad (2.16)$$

The total energy and the quantized part of exciton pair is then defined in terms of exciton Rydberg energy,

$$E_{1S1s} = E_g - R_y^* \left[1 - \frac{\mu}{M} \left(\frac{\pi a_B}{a} \right)^2 \right] \quad (2.17)$$

From the Equation 2.17, the quantized exciton energy is defined as,

$$\Delta E_{1S1s} = \frac{\mu}{M} \left(\frac{\pi a_B}{a} \right)^2 R_y^* \quad (2.18)$$

If we assume creation of electron-hole pairs with no angular momentum, the “free” electrons and holes have energies

$$E_{ml}^e = E_g + \frac{\hbar^2 \chi_{ml}^2}{2m_e a^2} \quad (2.19)$$

$$E_{ml}^h = \frac{\hbar^2 \chi_{ml}^2}{2m_h a^2}$$

The quantized exciton energy is small compared to R_y^* as far as $a \gg a_B$. This gives the quantitative description of “weak confinement”. The physical interpretation to this analytical result is that if the size of the nanocrystal is larger compared to the exciton Bohr radius, the needed energy for the creation of electron-hole pairs are lower.

2.3.2 Strong Confinement:

In the strong confinement regime, the dimension of nanocrystal is smaller than the exciton Bohr radius ($a \ll a_B$). At this case, electrons and holes have no bound states corresponding to hydrogen like exciton and the lowest state kinetic energy in Equation 2.19 is considerably larger than the Rydberg energy, R_y^* . Due to this factor, the absorption spectrum gives discrete bands which can be formalized as follows:

$$E_{nl} = E_g + \frac{\hbar^2 \chi_{nl}^2}{2\mu a^2} \quad (2.20)$$

The absorption energy is strongly varying with the size, which means at the strong confinement regime, the absorption-emission spectrum can be modified by changing the nanocrystal size.

2.3.3 Growth of Nanocrystals in a Matrix:

Growth of crystallites in a matrix is due to the phase transition in a supersaturated solution. The temperature range in which the phase transformation occurs is between the temperature of the matrix transition and the temperature of the melting point of matrix:

$$T_{matrix} < T < T_{melting} \quad (2.21)$$

This process is controlled by the diffusion of ions dissolved in the matrix.

The precipitation phenomenon of interdiffused ions throughout the matrix is occurred in three steps: 1. nucleation, 2. normal growth and 3. competitive growth [48 - 52]. At the nucleation stage, small nuclei are formed. At the second stage, crystallites exhibit a monolithic growth due to the motion of atoms through the interface of nucleus and matrix. At the final stage, the crystallites are large enough and super saturation is negligible. At this stage, the growth mechanism is driven by the diffusive mass transfer from smaller particles to larger ones and the surface tension plays the dominant role. This stage is commonly referred as Ostwald ripening, competitive growth, diffusion limited growth or coalescence.

The size of the nanocrystals can be controlled by the fabrication method, operation pressure, temperature, layer thickness and concentration of individuals in the matrix. To analyze the formation and evolution of nanocrystals in a matrix, electron microscopy, electron spectroscopy, Raman scattering and x-ray scattering may be used. The fabricated sample can also be treated to optical analyses. In the next chapter, the method of fabrication and characterization techniques is discussed.

CHAPTER 3

INSTRUMENTATION FOR FABRICATION AND CHARACTERIZATION

3.1 Introduction:

In this part, a background on the instrumentation for fabricating and analyzing the studied samples will be given. The fabrication method to these samples was magnetron sputtering technique and post annealing in order to induce film crystallization and nanocrystal formation. There were numerous diagnostic techniques to monitor these formations. X-ray diffraction (XRD) was employed in order to detect the crystal structure and phase of the Al_2O_3 and Si nanocrystals. Atomic force microscopy (AFM) and scanning electron microscopy (SEM) were used for the detection of the surface profile of the films. X-ray photoelectron spectroscopy (XPS) revealed the atomic composition and chemical state of the films with respect to depth. Finally, photoluminescence (PL) was used to monitor the absorption emission mechanism of the films. Here brief information about these techniques will be given.

3.2 Magnetron Sputtering:

Sputtering is the physical vaporization of atoms from a target surface by momentum transfer from bombarding energetic atomic sized particles. Sputter deposition is the deposition of particles, whose origin is from a target being sputtered. Planar magnetron sputtering is the most widely used technique, which uses magnetic field to confine the motion of secondary electrons above the surface

of the target [53]. The target to be sputtered is the source of the deposition material in the sputter deposition process (Figure 3.2) [54]. Figure 3.1 shows our sputter deposition system Nano D100, which is produced by VAKSIS [55].



Figure 3.1. Main chamber of the sputter deposition system located in Semiconductor Material & Device Fabrication Lab.



Figure 3.2 The targets used in the experiments: Al₂O₃ (left) and Si (right)

A good sputter deposition process should be done in vacuum ($<10^{-6}$ Torr with a base pressure) and in a low pressure gas ambient in order to enhance the rate and the yield of the deposition process ($<5 \times 10^{-3}$ Torr). Sputter deposition can be done by using an elemental material or a compound material as a target. When using a compound material, the deposited film usually lacks of the element that is more volatile in the target (oxygen from SiO₂ or Al₂O₃) because of the transport and condensation process. This loss can be overwhelmed by adding some proportion of the corresponding element in the sputtering gas. This process is called “quasi-reactive sputtering”. Sputtering yield depends on:

- The mass and the energy of the sputtering particles in the gas
- Angle of incidence of the bombarding particles
- Structure of the target (bonding energy etc.)
- Target morphology (yield decreases as the target surface goes from smooth to rough, which is called “preferential sputtering”)

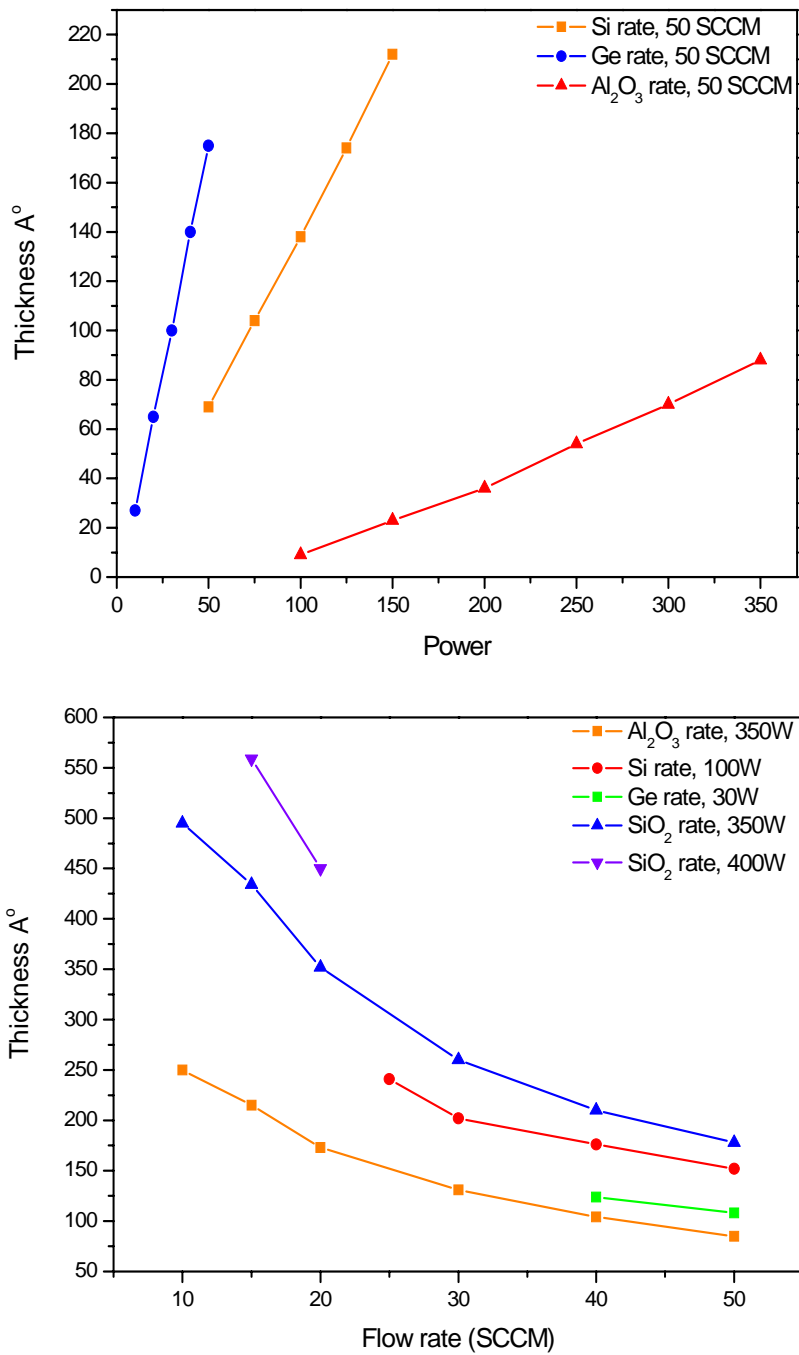


Figure 3.3. Sputter rate with respect to magnetron power (above) and Ar flow rate (below). Each thickness value was recorded after 15 minutes of sputtering.

Figure 3.3 shows the sputter rate with respect to Ar flow and magnetron power for different target materials for our system. By increasing the energy sputter yield increases initially but at very high energies, sputtering yield decreases since the bombarding particles may re-sputter or implant the substrate surface (not shown here). Sputtering yield can be inferred from the ratio of the number of atoms ejected from the surface to the number of atoms bombarding the surface [56]. If a weakly conducting or a non-conducting layer is formed on the surface of a conductor target, the sputter rate consequently decreases and arches are seen on the target surface. This “poisoning” effect is due to the interaction of the target species with plasma.

3.2.1 Sputtering Methods:

There are large varieties of techniques for sputter deposition of the materials. The most widely used ones are cold cathode DC diode sputtering, DC triode sputtering, AC sputtering, radio frequency (RF) magnetron sputtering, DC magnetron sputtering, pulsed DC magnetron sputtering, ion and plasma beam sputtering.

3.2.1.1 RF Magnetron Sputtering:

In RF sputtering a large peak to peak voltage is applied to the electrodes and an alternating voltage is applied target surface. The advantage of the RF technique is that insulating targets can also be sputtered under alternating cycles of voltage. At one half-cycle of the potential the target surface is bombarded by the ions and the target species are sputtered. At the following half-cycle, the electrons are directed towards the target surface in order to prevent any charge build up. The range of frequencies is from 0.5 to 50MHz, but 13.56MHz is widely used. Most insulating materials have large thermal expansion coefficients and are brittle materials. During RF sputtering at high energy bombardments, the excess energy may cause

fracturing of the target material. Another drawback of RF technique is the low sputter rates with respect to other techniques. Pulsed DC sputtering can also be used for reactive sputtering of the electrically insulating oxide targets.

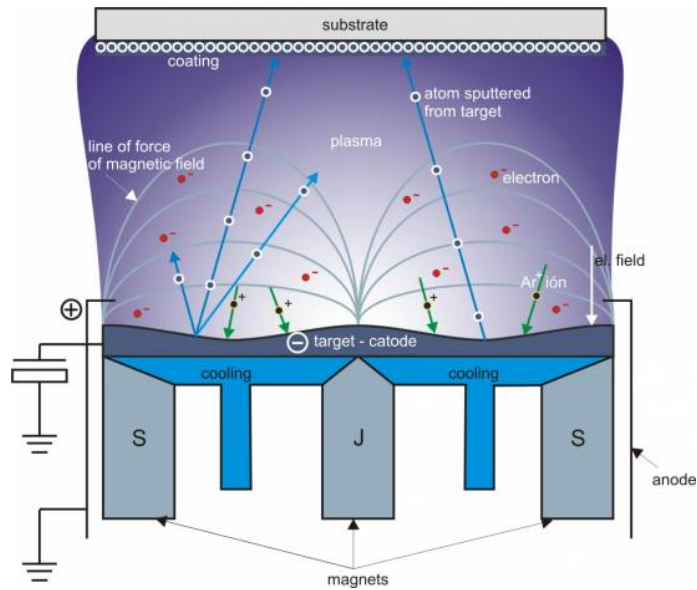


Figure 3.4. The schematic of the sputter deposition system. The positively charged Ar^+ ions hit to target/cathode and the neutrally ejected target atoms stick to the substrate. Adopted from Ref. 57.

3.2.1.2 DC Magnetron Sputtering:

In DC magnetron sputtering, the electrons that are ejected from the target surface are not effectively used as in the case of RF sputtering technique. In DC magnetron sputtering, however, the ejected target electrons is circulated above the surface by applying a magnetic field and arranging the magnets suitably. These

circulating electrons create highly dense plasma above the surface and DC magnetron sputter process starts. Very high sputter rates are fed by the high density plasma above the target surface. This is the most important advantage of this technique. Main disadvantage of the DC magnetron sputtering is the relatively non-uniform plasma above the target surface, which depends on the configurations of the magnetrons. In order to prevent non-uniform growing of the film, substrate position must be well aligned with respect to the target.

3.2.2 Reactive and Non-Reactive Sputter Deposition:

A gaseous medium of lighter atoms in a sputter chamber results in reactive sputtering but not physical sputtering [58]. Generally a heavier inert gas is used to aid in physical sputtering (such as argon). Heavier sputter gas and lighter reactive gas is injected together to concede reactive sputtering. Main drawback of the reactive sputtering technique is “poisoning” of the target material by the reactive species in the plasma. Poisoning effect drastically reduces the sputter rate and efficiency. Poisoning effect becomes weaker when the total gas pressure decreases. In some systems the sputtering gas flow is very close to the target while the reactive gas is sent through the substrate. By this way, the effect of poisoning is minimized. Increasing the temperature of the gas increases the reaction rate, which consequently increases the sputter rate, and prevents target poisoning. In reactive sputtering the location and variation of the plasma is also very important. The formation of plasma should be closer to the substrate when processing reactively.

In non reactive sputtering, the film properties are affected by the pressure of the gas and thermalization of the particles. Sputter gas pressure affects the density and the residual film stress. At relatively high pressure values, the film is less tensile, however at lower pressures; the sputtered film stress is higher.

3.2.3 Changing the Geometry of the Target:

Change in the geometry can cause negative effects on sputter deposition. In planar magnetron sputtering, a “race-track” is formed on the target. The unused parts may be poisoned in time, resulting in a decrease of the sputtering rate and arcs may be seen. Moreover a rougher target surface will also decrease the sputter rate. Roughening can be due to preferential sputtering according to the atomic planes of the target or surface recrystallization of the target.

For further information about sputtering principles and applications, refer to M.Sc. Thesis by Arif Sinan Alagöz [59].

3.3 X-Ray Diffraction:

X-ray diffraction (XRD) is a technique, used for characterization of crystalline phases of materials. By using XRD, some structural properties can also be estimated such as strain, grain size, phase composition, preferred orientation, defect structure and film thickness. Determining these physical properties of thin films from XRD is of technological interest since these properties also affect the optical and electronic properties of films.

3.3.1 Ideal diffraction conditions:

Figure 3.5 shows the basic features of XRD experiment [60]. Here the diffraction angle 2Θ is the angle between the incident and diffracted x-ray. The x-ray source is Cu K_α for our system with a wavelength of 1.54\AA . From the successive diffraction of x-ray through the planes of a crystal, the plane spacing can be found:

$$\lambda = 2d_{hkl} \sin \Theta_{hkl} \quad (3.1)$$

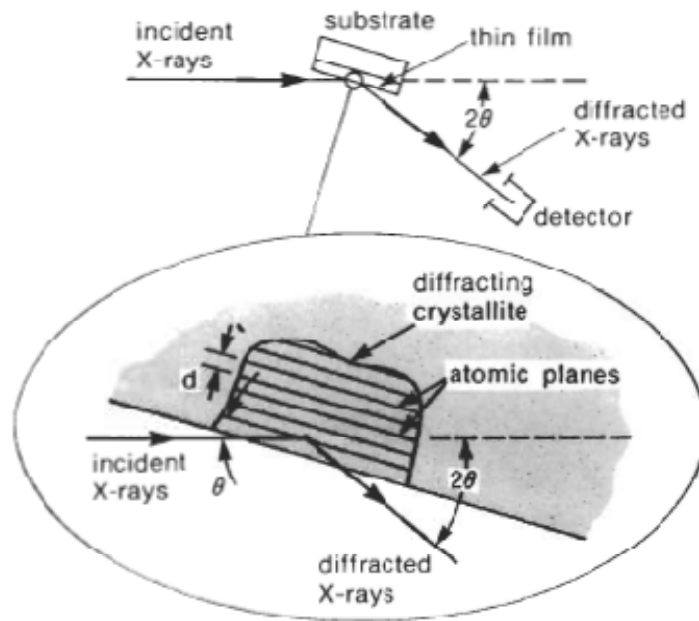


Figure 3.5 The basic features of an XRD experiment.

This is Bragg's law of diffraction. From the plane spacing, by knowing the Miller indices, the lattice constant of the interested material can be found.

$$d_{hkl} = \frac{a_0}{\sqrt{h^2 + k^2 + l^2}} \quad (3.2)$$

Bragg-Brentano geometry (Figure 3.6) [61] is widely used for analyzing the polycrystalline thin films. Since the incident and diffracted x-rays make the same angle on the surface, the obtained data includes the information from the planes parallel to the surface exclusively.

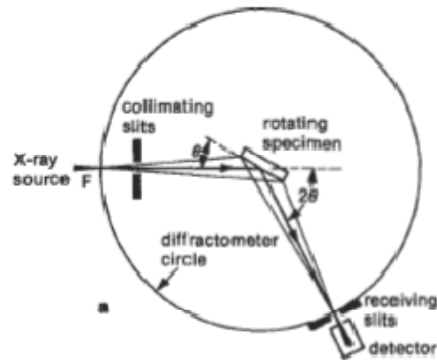


Figure 3.6. Bragg-Brentano diffractometer. The point F is either the focal point of the monochromator or the focal point on an X-ray tube. Adopted from Ref. 61.

3.3.2 Non ideal diffraction conditions:

The Bragg Law, defined in the previous section is exactly true only in ideal conditions. When talking about ideal conditions, the structure of the crystal and also the impinging x-ray beam should be considered. An infinite-size crystal and a beam composed of perfectly parallel rays form together the ideal conditions. However, not any crystal has infinite size, the discontinuity at the “edges” and at the “corners” can be thought as imperfections. Non-parallel beams do exist in experiments, since a perfectly parallel beam can’t be created in the laboratory. In fact, the incoming x-ray beam is composed of divergent and convergent rays as well as parallel rays. Figure 3.7 shows the ideal and experimental diffraction conditions from a certain specimen. In ideal conditions, the Bragg Law is exactly satisfied and a single intense line is observed from the angle 2Θ . In this scheme, the diffracted beams are destructively interfered, and only a constructive interference is seen at Bragg angle.

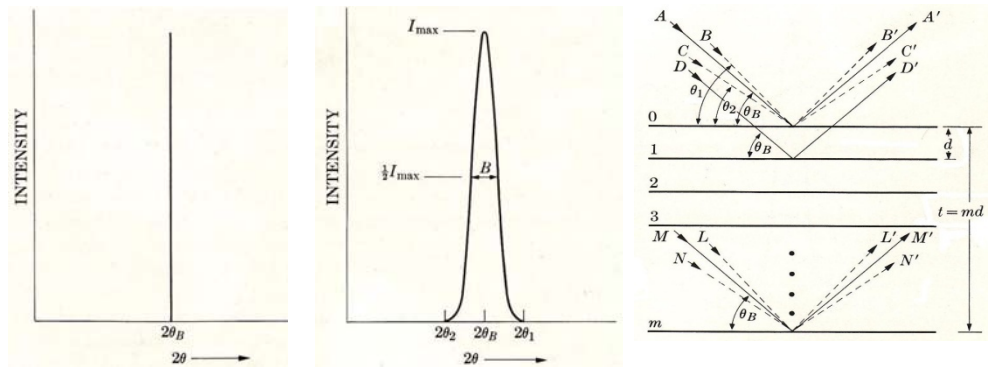


Figure 3.7. The diffraction at ideal (left) and non ideal (centre) conditions. The effect of the finite size of the crystal on diffraction is seen on the right.

As the number of Bragg planes becomes less, the chance of complete destructive interference is decreased. The consequence of this phenomenon is a broader diffraction peak i.e. a larger width at the value of FWHM ($I_{\max}/2$). If the size of the interested crystal is less than 200 nm, the effect of broadening becomes clearly evident. From this broadening, the size estimation of the nanocrystals is possible [27]:

$$t = \frac{K\lambda}{B \cos \Theta_B} \quad (3.3)$$

The formula is named as Scherrer's formula and the method is named as Scherrer's method. Scherrer's method is used to estimate the particle size of very small crystals [62]. In the above equation, λ is the wavelength of incoming x-ray (Cu K_α for our system with a wavelength of 1.54\AA), B is the full width half maximum

of the diffraction peak, K is the Scherrer's constant and t is the size of the crystal grain.

3.4 Scanning Electron Microscopy:

Scanning electron microscope (SEM) replaces the optical microscope as the starting tool for material characterization due to its wide range of information that it provides from the surface. The resolution of the SEM can be down to 2-3 nm and the possible range of magnification is from 10X to 300.000X for a standard SEM. The information we “see” from SEM is the topological image of the electrons collected from the very top surface layers of the specimen.

SEM works under high vacuum conditions through which a source of electrons from the electron gun is focused on the surface of the specimen as seen from the Figure 3.8 [58]. At the surface, some certain interactions occur between surface atoms and incoming electrons. Mainly, surface electrons are ejected and these secondary electrons are collected by appropriate detectors and the output is modulated to give a contrasted electron image. The x-y scanning modes then give a fully scanned and contrasted image.

In SEM, generally vacuum compatible samples are analyzed. If the sample is conducting, a good image quality is obtained. For insulating samples, the image quality is decreased due to poor conductance of the surface. In order to improve the quality of the image, the surface of the specimen is sputtered with a thin (1-10 nm) conducting film of carbon, gold or other metals. Low vacuum mode can also be used to monitor the insulating films if sputtering is not desirable.

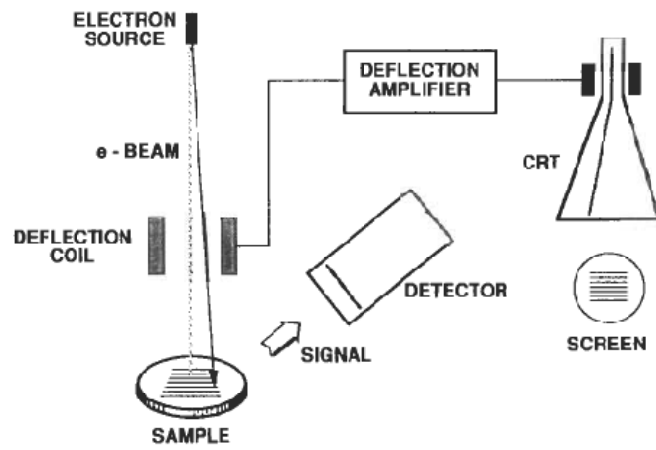


Figure 3.8. The schematic describing the operation of an SEM.

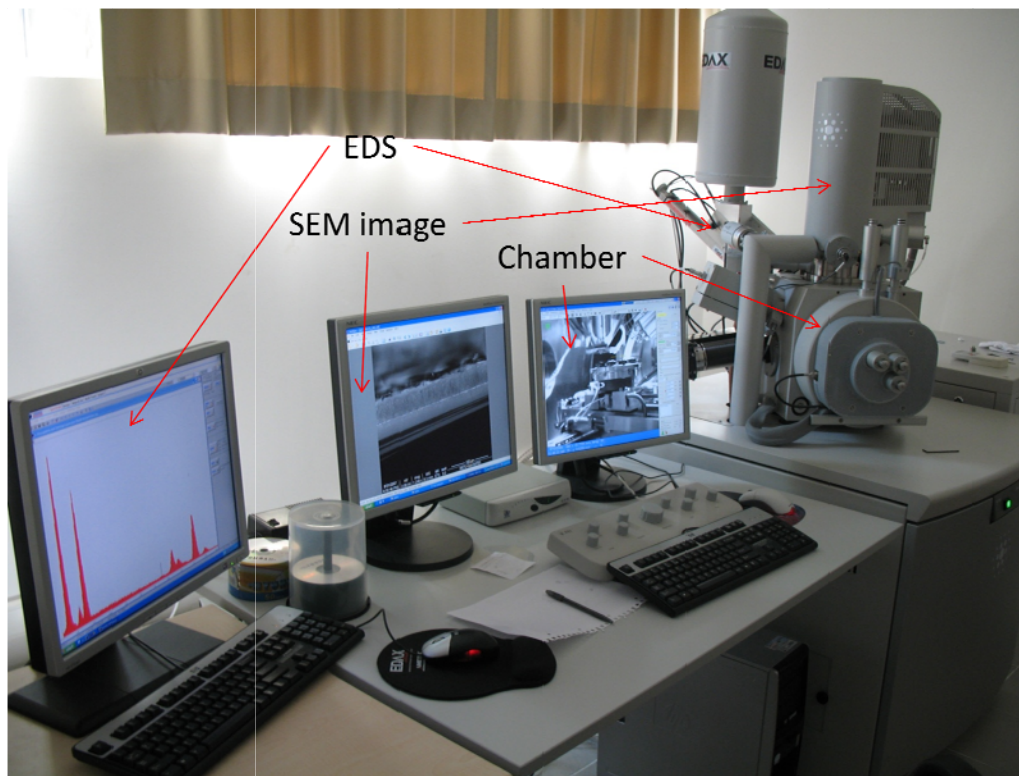


Figure 3.9. The image of the SEM, located at Central Laboratory.

For elemental detection, both energy dispersive and wavelength dispersive detectors can be used in SEM [58]. The electrons produce an output signal which is proportional to the number of x-ray photons in the bombarded area. The resulted spectrum contains different peaks at different energies and intensities, corresponding to different elements and proportions, respectively. Figure 3.10 shows an EDS spectrum of the sputtered Al_2O_3 samples containing Si nanocrystals. The information gathered from the sample goes deeper as the electron energy is increased.

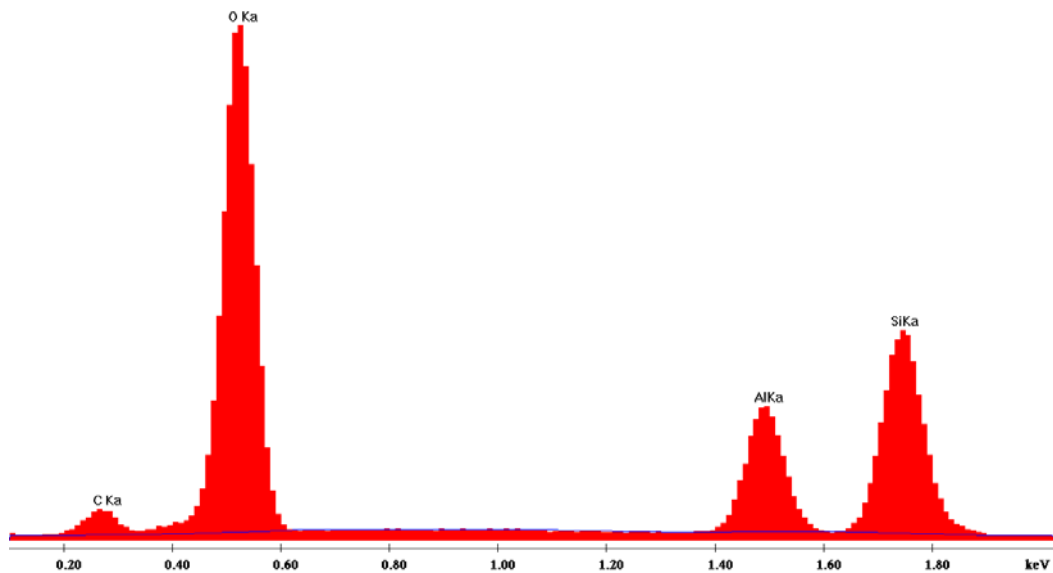


Figure 3.10. A typical EDS spectrum of Al_2O_3 sputtered films with Si nanocrystals. C peak is from the surface due to contamination.

3.5 X-Ray Photoelectron Spectroscopy:

X-ray photoelectron spectroscopy (XPS) is a quantitative spectroscopic technique that measures the elemental composition, chemical state, empirical formula, and electronic state of the elements existing in the analyzed specimen. The irradiation source can be either an aluminum or magnesium x-ray. The obtained spectra is a measure of the kinetic energy E_{kin} and number of electrons from the top 1 to 10 nm of the sample surface. Due to the necessity of high surface sensitivity, ultra high vacuum conditions (UHV) are crucially important. The ejected electrons are from the core shells of the atoms and their kinetic energies are fingerprints of their host atoms. From the slight variations in E_{kin} of an electron, the alternative binding and oxidations states can be detected [63].

The binding energy of an emitted electron can be found by using an equation based on the work of Ernest Rutherford (1914) [64]

$$E_B = E_{ph} - E_{kin} - \Phi \quad (3.4)$$

When an incident x-ray photoelectron, $E_{ph}=h\nu$, interacts with an electron with binding energy E_B , the electron is removed as far as $E_{ph}>E_B$. If the liberated electron has enough energy to overcome the work function, Φ , of the spectrometer, it will reach to vacuum level with a remaining kinetic energy E_{kin} . Since E_{ph} and Φ are known quantities, it is left to E_{kin} , to estimate the binding energy of the “photo-emitted” electron. The schematic diagram representing these physical phenomena is illustrated in Figure 3.11.

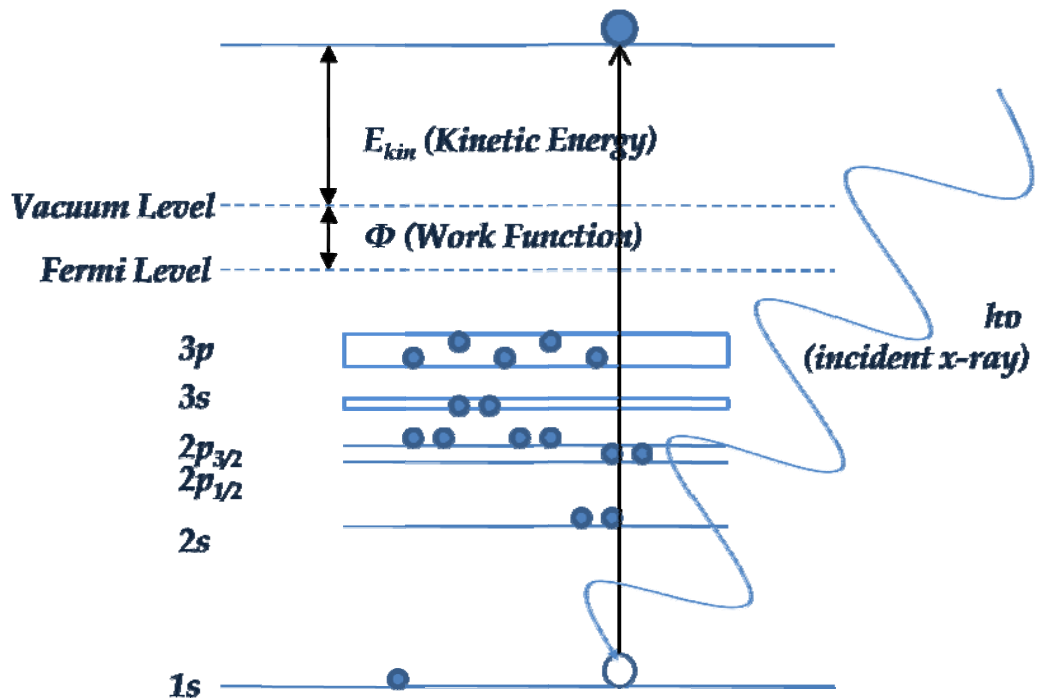


Figure 3.11. An illustration of the photoemission phenomenon in XPS.

Figure 3.12 represents the Specs 200 x-ray photoelectron spectrometer in which the experiments are conducted. It's not just taking the data, but also a comprehensive work to analyze it. The raw data usually includes background "noise" and possible binding and oxidations states. To do a suitable background subtraction is of crucial importance to deconvolute the possible binding states correctly. The most widely used background subtraction methods are proposed by Shirley [65] and Tougaard [66]. For the peak fitting process, Voigt function should be used, which is a Gaussian/Lorentzian type function.

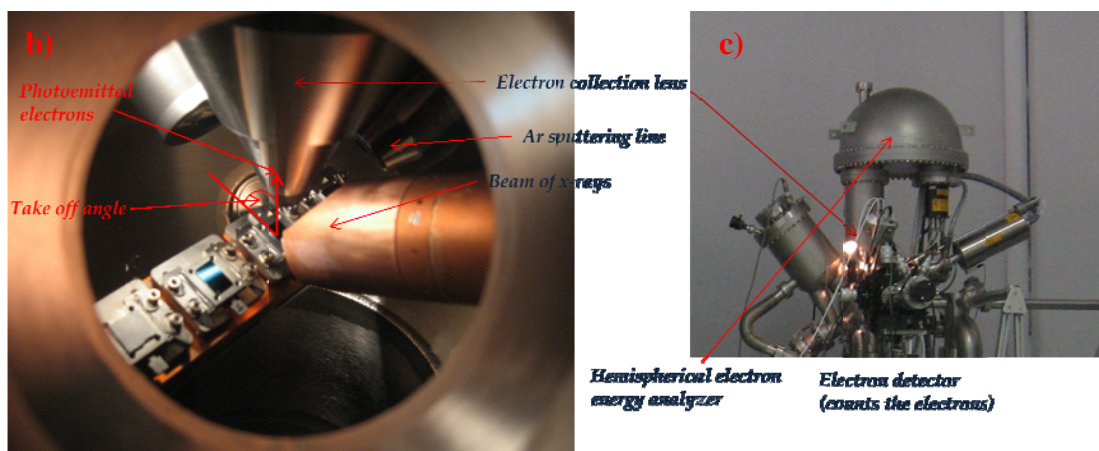


Figure 3.12. Specs 200 XPS, located at Central Laboratory (a) General view, (b) process chamber and (c) electron analyzer.

XPS is not only suitable for surface analysis, but also for depth profiling of the elements and binding states throughout the specimen. The depth profiling process is actually a means of sputtering with accelerated Ar atoms onto the film. Thus, this is a destructive technique, and by this process, atomic mixing, knock on implantation, bond breaking, charging and preferential sputtering might possibly occur. In order to get rid of these effects, it's best to use high mass ions with low energy [67].

There are a number of applications and studies of XPS on the topic of semiconductor nanocrystals. Semiconductor nanocrystals and their interfaces can be studied by depth profiling and synchrotron radiation respectively [68 - 69]. For further information, refer to Ms. Thesis by Selçuk Yerci [70].

3.6 Photoluminescence Spectroscopy:

Photoluminescence spectroscopy (PL) is used for the detection of “photo-emitted” light from matter. Being non-destructive is the main advantage of this technique. In principle, an incoming high energy light at a constant wavelength, preferentially a laser is used to illuminate the specimen to be analyzed. The high energy of the incoming photons is transferred to charge carriers by exciting them to permitted higher energy bands of the specimen. The relaxation, or recombination, of the excited charge carriers is possible between the allowed bands through forbidden gaps. If the recombination mechanism is radiative, the energy is “photo-emitted” from the specimen with a wavelength that represents the characteristic energy between two energy bands, or the energy of the forbidden gap.

By using PL spectroscopy, the band gap and impurity levels and defects can be studied. Analysis of the PL also helps to understand the radiative recombination mechanisms. A representative illustration for the generation and recombination mechanism is given in Figure 3.13.

The most widely used PL experiment types are continuous wave PL, time resolved PL, temperature dependent PL and Z-scan PL.

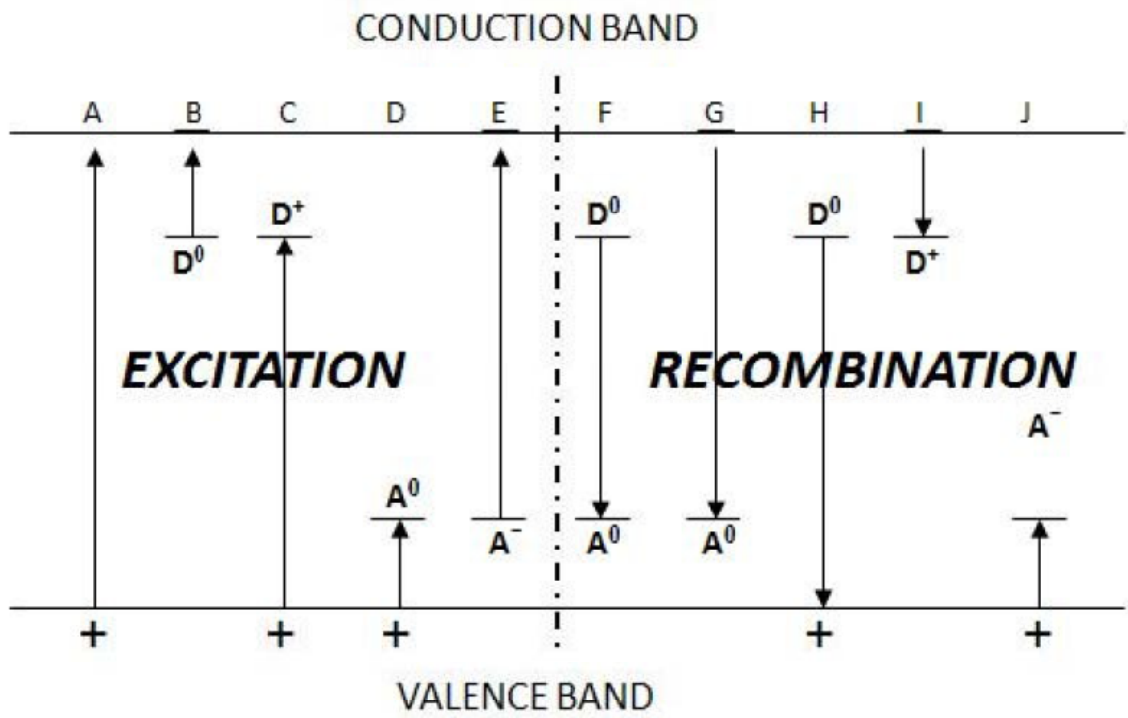


Figure 3.13. Possible excitation and recombination mechanisms between the conduction and valence bands of semiconductors [71].

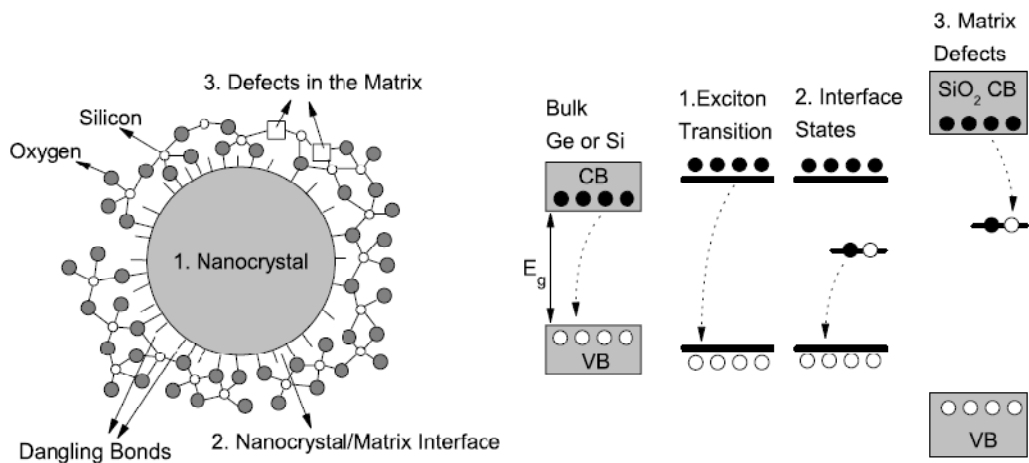


Figure 3.14. Possible light emitting mechanism of PL from Si-nc/SiO₂ system: Left: pictorial illustration, right: energy levels including (1) recombination of electron-hole pairs in the nanocrystal, (2) radiative states at the interface between the nanocrystal and SiO₂ matrix (3) luminescent defect centers due to the matrix defects [72].

In the case of semiconductor nanocrystals, PL is used to determine the radiative recombination that might be generated from the excitons in nanocrystals, interface regions, or from the defects in the matrix. If the PL is due to the radiative recombination in the nanocrystals, the shift in the PL peak position is a result of size variation of the nanocrystals. Hence, the excitonic transitions in nanocrystals should be size dependent due to quantum confinement effect. For the interface and defect related emissions, the PL signal does not show a systematic behavior and quantum size effects are not present. The possible emission mechanisms for the Si-nc/SiO₂ system are given in Figure 3.14.

A typical PL setup consists of an excitation source to generate electron hole pairs, a monochromator to resolve the photo emitted light from the specimen, and a

CCD camera to record the spectrum. In this work, an excitation source of 532 nm Nd:YAG laser, an MS 257 type monochromator and Hamamatsu CCD camera is used for measurements.

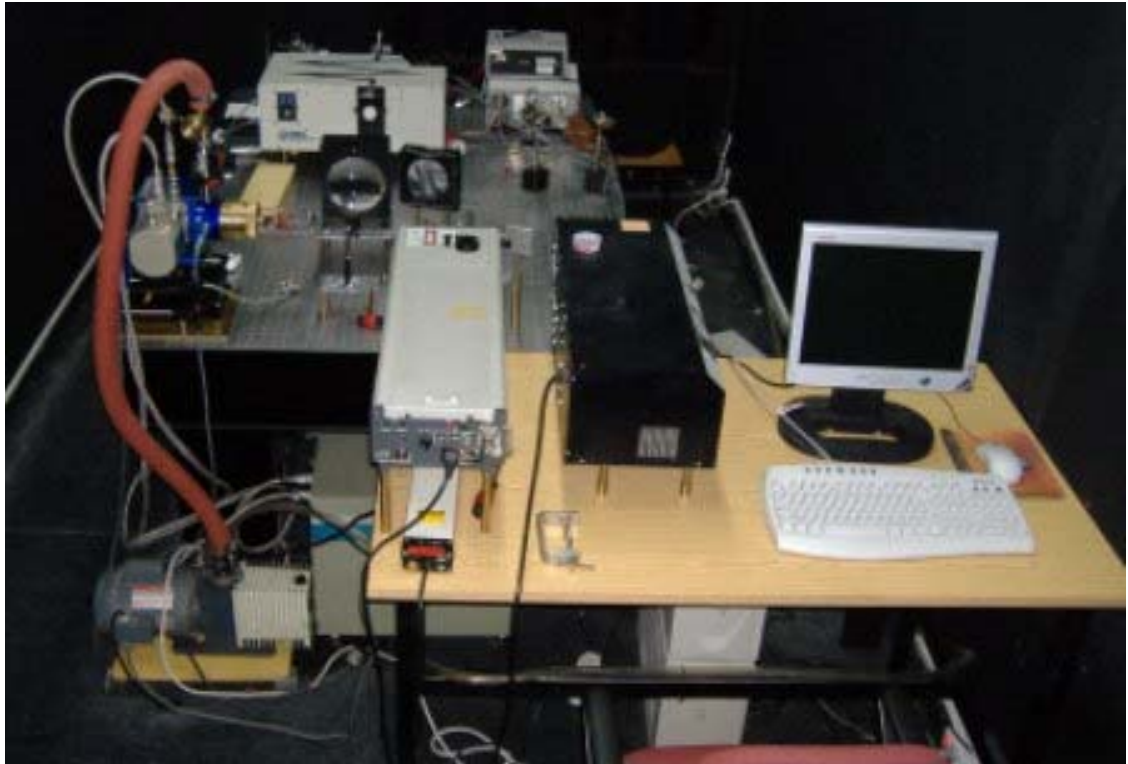


Figure 3.15. The experimental PL setup used in this work.

CHAPTER 4

FABRICATION AND CHARACTERIZATION OF Al₂O₃ SPUTTERED FILMS

4.1 Fabrication:

N-type Si (100) wafers (resistivity of 1-10 Ωcm) without any thermal oxide layers were used as substrates for Al₂O₃ sputtering. The substrates were subjected to standard Si wafer cleaning procedure. A ceramic Al₂O₃ target was placed on one of the magnetrons, which was powered by RF generator. Before fabricating the samples, pre-sputtering process was carried on, in order to avoid the unwanted effects of remnants on the Al₂O₃ target from the previous runs. The sputtering gas used in the system was electronic grade (6.0) Argon and the reactive gas for sustaining stoichiometry was electronic grade (5.5) Oxygen. Table 4.1 shows the details of the pre-sputtering procedure before each run.

Table 4.1. The details of the pre-sputtering procedure.

RF Power	Flow Rate	Target	Base Pressure	Operating Pressure	Time
150W	50SCCM	Al ₂ O ₃	6x10 ⁻⁷ Torr	3x10 ⁻³ Torr	30 min

In order to get rid of the contamination due to residual water and water vapor at the walls, the chamber was heated at 400°C for 30 minutes before sputtering. Deposition of Al₂O₃ films were at room temperature and the base pressure before sputtering was in the order of 10⁻⁶ Torr. Power of the RF was 350 W and different amount of oxygen was sent into the plasma in order to determine the desired stoichiometry. Also the effect of total gas pressure on the stoichiometry was studied for 50 and 20 SCCM total gas flow (Ar+O₂). Details can be seen in Figure 4.1., Table 4.2 and Figure 4.2.

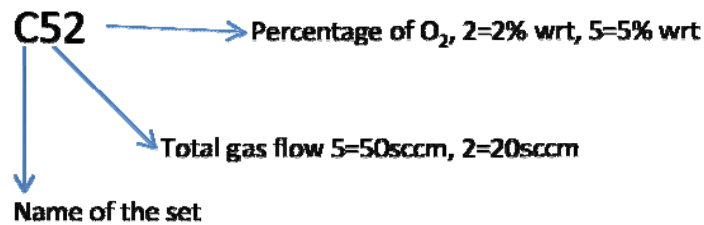


Figure 4.1. Abbreviations used in coding the sample names.

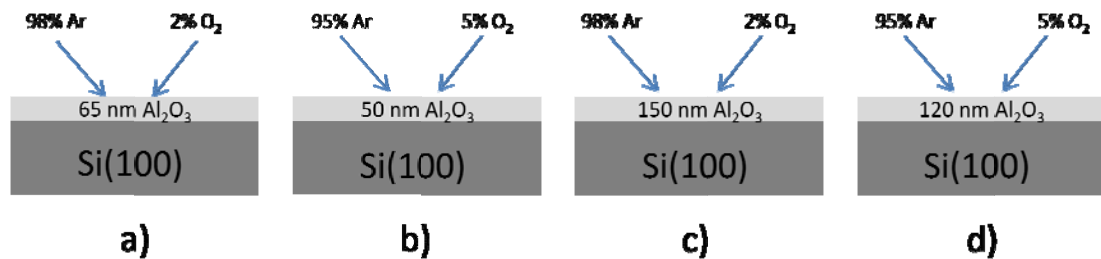


Figure 4.2. Schematic diagram of the sputtered samples of (a) C52, (b) C55, (c) C22 and (d) C25.

Table 4.2. Details of the sputtering procedure.

Set	Base Pr. (Torr)	Ar Pr. (Torr)	RF (Watt)	Flow (Ar+O ₂) (SCCM)	Oxygen (%)	Sp. Time (min)	Film (nm)
C52	9.0x10 ⁻⁷	2.7x10 ⁻³	350	49+1= 50	2	180	65
C55	1.6x10 ⁻⁶	2.9x10 ⁻³	350	47.5+2.5= 50	5	180	50
C22	1.2x10 ⁻⁶	9.0x10 ⁻⁴	350	19.6+0.4= 20	2	180	150
C25	1.0x10 ⁻⁶	1.1x10 ⁻³	350	19+1= 20	5	180	120

These samples were annealed under N₂ ambient at atmospheric pressure for 1 hour at 900, 1000 and 1100°C. Samples were annealed separately in order to prevent diffusion between sample surfaces at high temperatures.

When oxygen is added to the sputtering gas, excellent stoichiometry can be obtained but the sputter rate is dramatically decreased with increasing oxygen partial pressure as it is seen in Table 4.2. This phenomenon was also proposed by others [73]. Increasing the plasma pressure also has a negative effect on sputter rate. Lower pressure samples have higher growth rate than high pressure ones. Moreover better uniformity is obtained for low pressure samples due to reduction of diffusion [74]. These discussions will be done in more detail in the characterization section.

4.2 Characterization:

Characterization process of sputtered Al_2O_3 samples was in terms of crystallographic, surface topographic, stoichiometric and optic techniques. To do these processes, XRD, AFM, XPS and PL techniques were employed. In order to determine the MOS compability and sensitivity as a radiation sensor, dosimetry experiments were conducted.

4.2.1 X-Ray Diffraction:

XRD is used in order to track the crystalline phases by increasing annealing temperature. XRD measurements were done by Rigaku Miniflex standard x-ray diffractometer with the excitation source of Cu K_α (1.54Å). XRD scans were performed at a scan speed of $2\Theta=0.5^\circ/\text{min}$ with steps 0.04° . It is known that different transition forms may coexist in the annealed samples below 1200°C [37]. As the temperature increases, the existed transition forms in the films become more stable. Figure 4.3 shows the XRD spectrum of C22 and Figure 4.4 shows the sputtered and annealed Al_2O_3 samples with flow rates 20 and 50 SCCM.

In Figure 4.3, almost no diffraction peak is seen for the as sputtered sample, indicating that the unannealed film was almost amorphous. As the annealing temperature increases, small diffraction peaks become evident between $2\Theta=35-60^\circ$. Some of the diffraction peaks increase with annealing temperature, while some of them disappear with annealing. This phenomenon can be explained by phase transition of aluminas with increasing temperature. For example the peaks located at 44.73° and 48.04° are stronger in 1000°C annealed sample with respect to 1100°C annealed sample and these peaks are due to the scattering from kappa-, eta-, delta-, chi- and gamma-alumina phases. However the peak located at 51.3° is more intense in 1100°C annealed samples, which is the alpha-alumina phase. So, when the temperature increases, some of these transition phases appear, and the

signal due to the stable ones increases while unstable ones turns into more stable forms. The overall x-ray diffraction data of the transition aluminas can be seen in Figure 4.5.

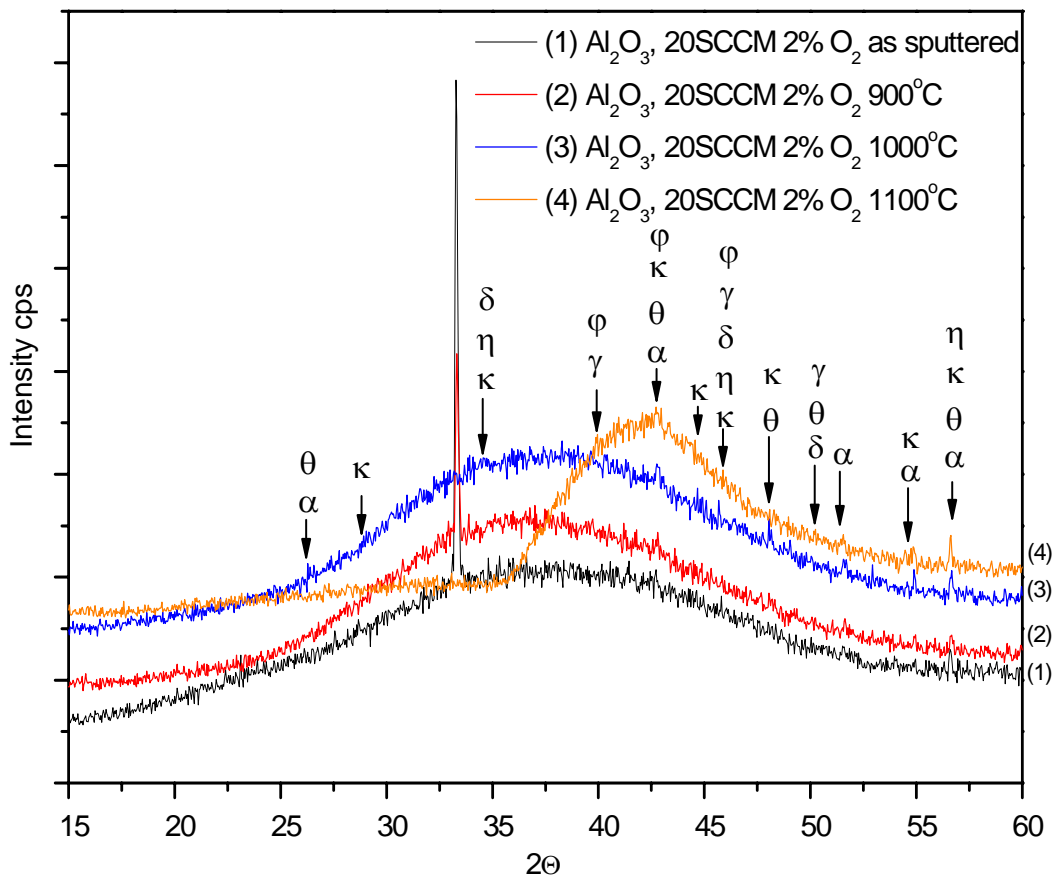


Figure 4.3. XRD spectrum of the sample C22, annealed at different temperatures.

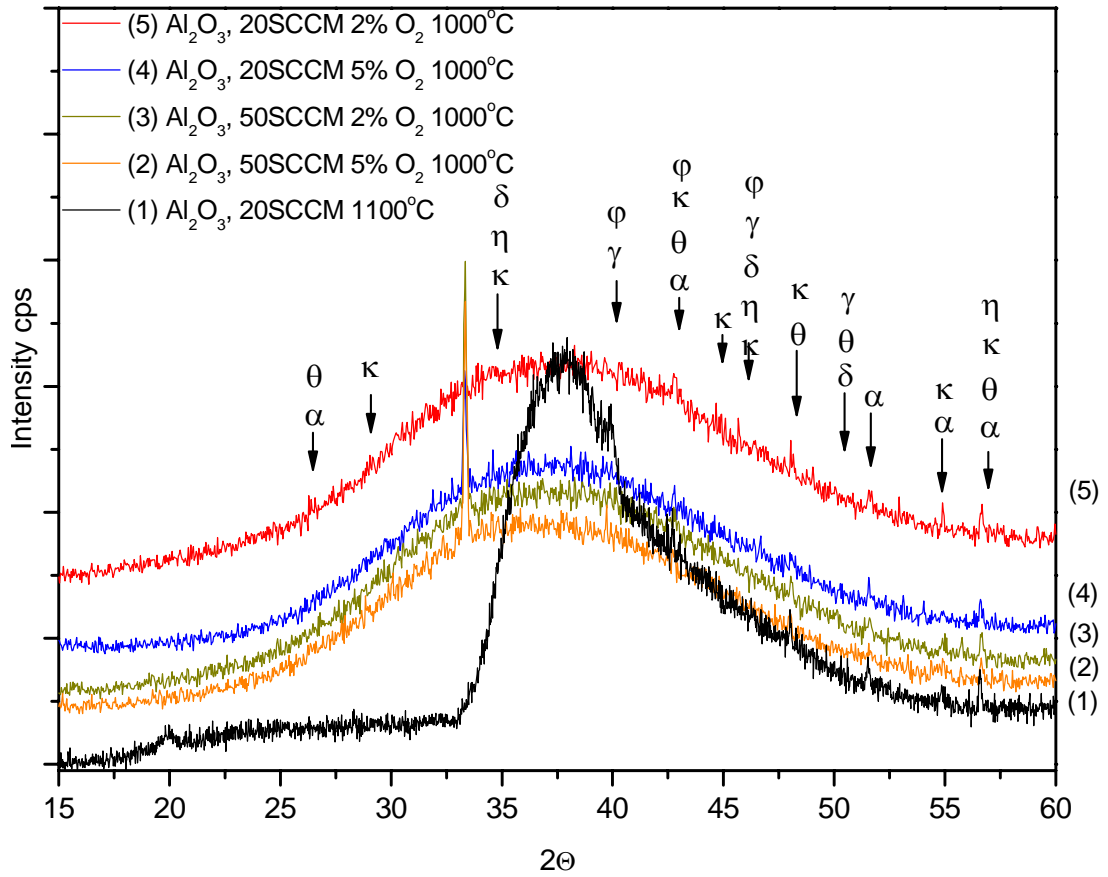


Figure 4.4. XRD spectrum of the samples annealed at 1000°C at different O₂ partials and reference sample sputtered without O₂.

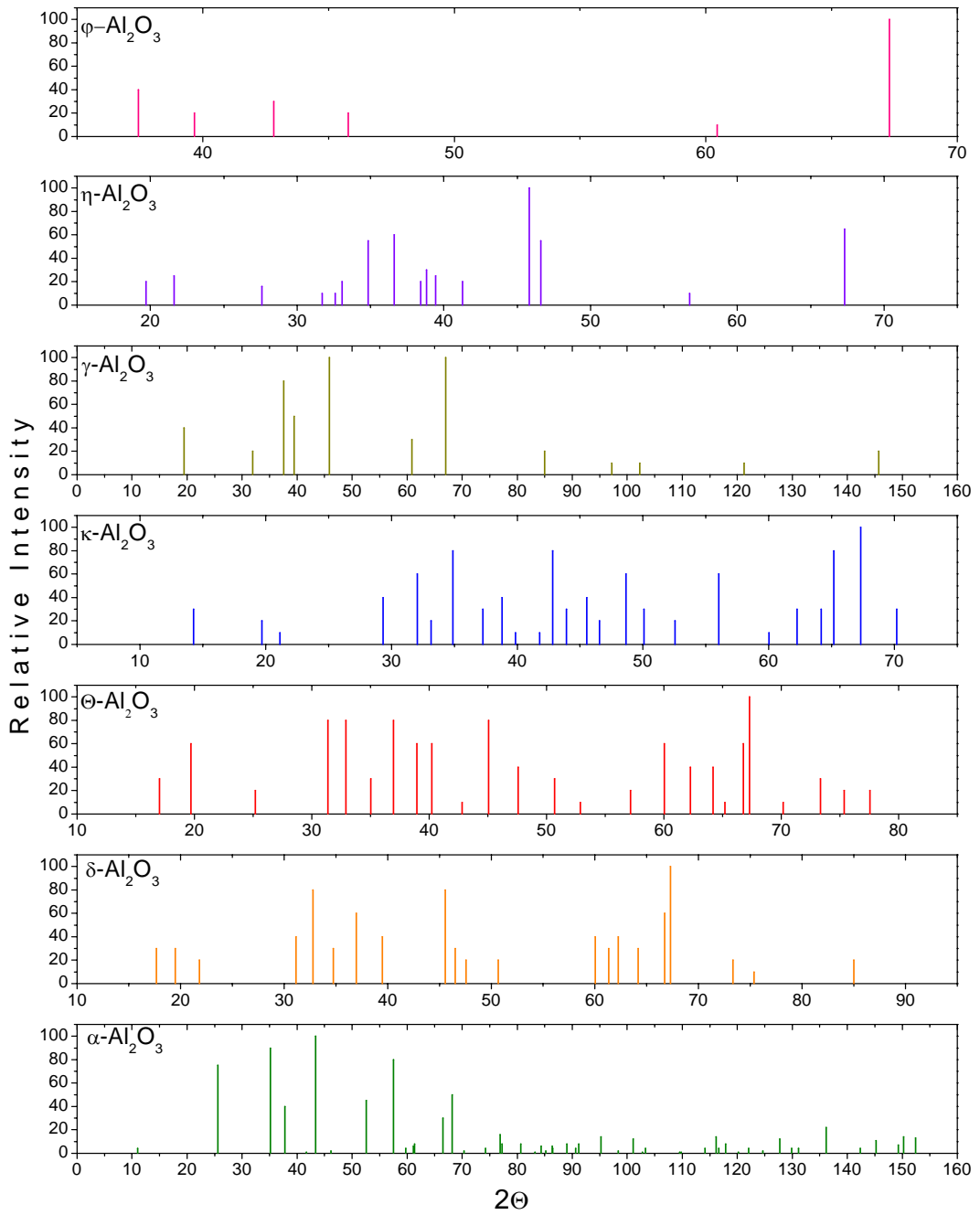


Figure 4.5. X-ray diffraction data of the transition aluminas.

Figure 4.4 shows the deposited samples annealed at 1000°C. All the deposited samples show almost similar diffraction peaks, which is due to the same transition forms of alumina at 1000°C. From (1) to (5), the intensity of the diffraction peaks increase. This phenomenon can be explained in terms of increased crystallinity with better stoichiometry. (1) is the reference sample, sputtered without any O₂ addition. By comparing the diffraction peaks in Figure 2.3, (1) is not an exact alumina form. O₂ addition to the sputtering gas is then sustains stoichiometry, giving more reliable diffraction peaks compared to (1).

Table 4.3 shows the composition of alumina films at different annealing temperatures. The least stable form Chi-alumina is the main form of the as sputtered samples. When the temperature increases, the transitions turn to more stable forms, which is theta-alumina for the 1000 and 1100°C annealed samples, as confirmed from the Figure 2.2. These diffraction peaks were estimated by the ICDD electronic database of the diffractometer manually.

Table 4.3. The transition forms, included by the films at different temperatures.

	<u>C55</u>	<u>C52</u>	<u>C25</u>	<u>C22</u>
<u>As</u>	Kappa	Chi	Chi	Chi
<u>900°C</u>	Gamma	Kappa	Delta	Gamma
<u>1000°C</u>	Gamma, Theta	Theta	Theta	Theta
<u>1100°C</u>	Gamma, Eta	Delta, Eta, Theta	Delta, Theta	Theta

The diffractometer used in the experiments was a standard diffractometer which takes data down to 2 μm from the top surface. Since the sputtered samples have thicknesses varying from 50 to 150 nm, the strength of the diffraction peaks were quenched strongly by the background diffraction from the substrate. Due to this reason, the signal to noise ratio is low, and the diffraction spectrum gives tiny little peaks from the sample.

4.2.2 Atomic Force Microscopy:

The atomic force microscopy (AFM) was developed to estimate the surface roughness of the sputtered films [75, 76]. Fabricating a smooth surface is desirable since the smoothness of the film is directly related to its quality. Figure 4.6 shows the AFM surface images of the sputtered film, coded as C22, with respect to increasing annealing temperatures. The scanned area of the films was $3 \times 3 \mu\text{m}$ and the size of the surface formations change from 2 nm to 10 nm. For the as sputtered sample, there is no obvious formation and the surface is completely amorphous and the roughness is about 2 nm. For 900 and 1000°C annealed samples, surface islands are evident and the size of these islands are around 10-15 nm. These formations are not so densely located which is a characteristic feature of the unstable alumina forms [37]. 1100°C annealed sample shows more smooth and densely formed surface profile. The AFM images are in a good accordance with the XRD data discussed in the previous section, in which more stable aluminas were formed with increasing annealing temperature.

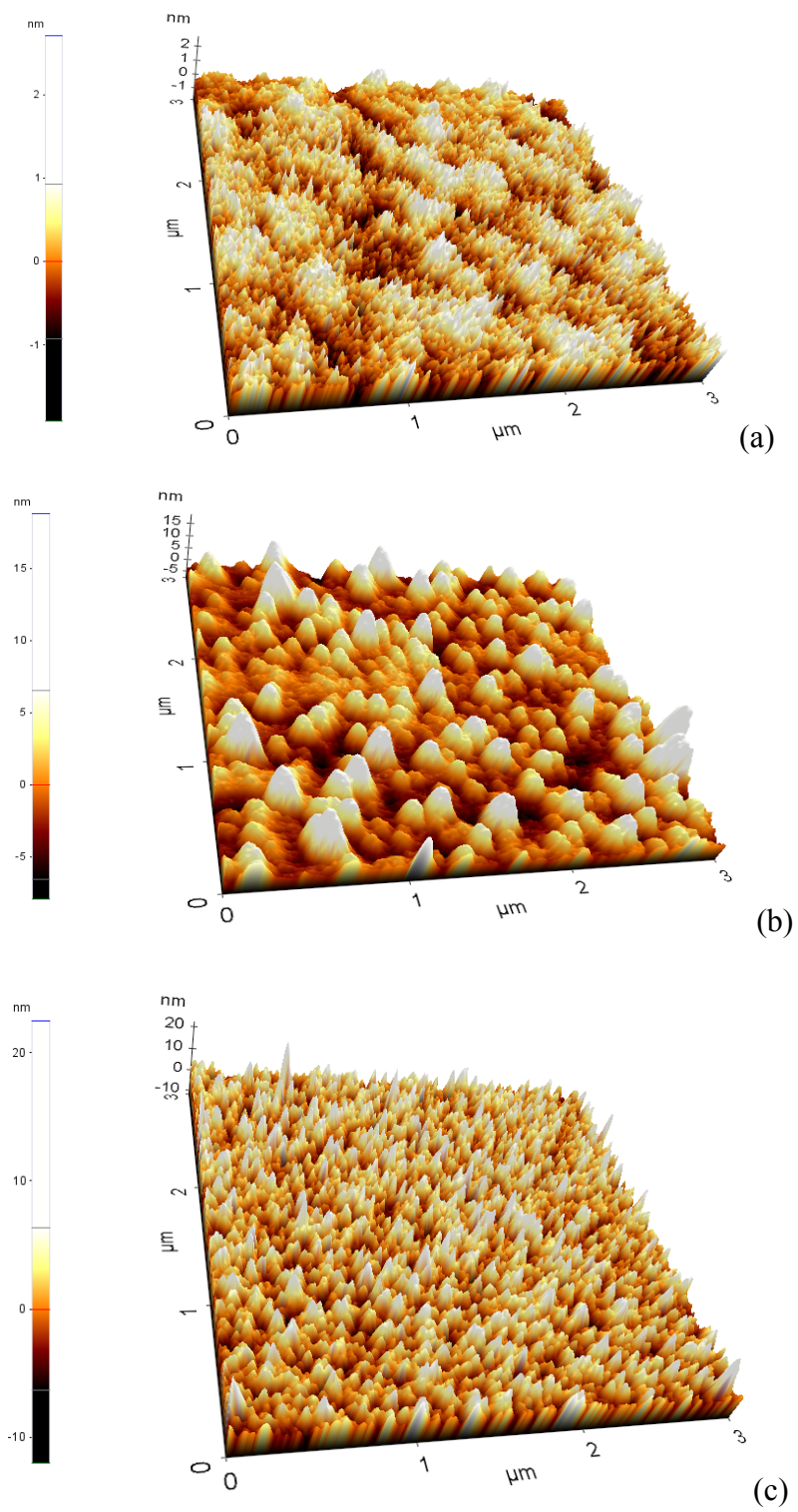


Figure 4.6 AFM images of C22, (a) as sputtered, (b) 900°C, (c) 1000°C and (d) 1100°C.

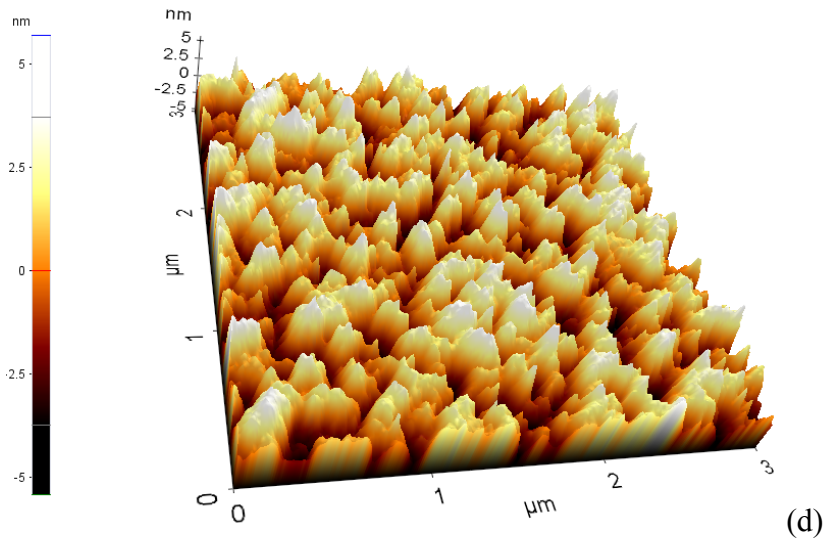


Figure 4.6 AFM images of C22, (a) as sputtered, (b) 900°C, (c) 1000°C and (d) 1100°C (continued).

4.2.3 X-Ray Photoelectron Spectroscopy:

XPS was employed to detect the stoichiometry of the as sputtered and annealed films. For the measurements, the surface layer was removed with 2500 eV Ar⁺ ions at duration of 3 min. and the layer just below the surface is examined for the desired stoichiometry. The measurement was conducted with an energy step of 0.10 eV, by using Al K_α as the excitation source. The range of the measurement for Al 2p was from 70 to 85 eV. All the measurements were done in UHV conditions.

Table 4.4 shows the atomic percentages of the films on the surface and beneath the surface. The stoichiometric analysis for the surface could not be done because of the existence of C contamination from the environment. C 1s peak was completely disappeared after the removal of the surface layer. From the atomic percentages, stoichiometry estimations can be done [77]. The as sputtered sample

of C22 has the most desirable proportions of Al and O, with a stoichiometry of $\text{Al}_2\text{O}_{2.98}$. After annealing, the ratio of O/Al was increased due to oxidation of upper surface layers under the carrying N_2 gas since N_2 has residual water and oxygen contamination.

Table 4.4. Atomic percentages of sample C22, with respect to increasing annealing temperatures.

<i>Sample</i>	<i>Al 2p %</i>	<i>O 1s %</i>	<i>C 1s %</i>	<i>Stoichiometry</i>
<i>C22 surf.</i>	35.3	49.0	1.,7	-
<i>C22 1st spt.</i>	40.6	59.4	<0.1	$\text{Al}_2\text{O}_{2.98}$
<i>C229 surf.</i>	29.5	58.9	11.7	-
<i>C229 1st pt.</i>	34.3	65.7	<1	$\text{Al}_2\text{O}_{3.83}$
<i>C229 2nd spt.</i>	33.7	66.3	<0.1	$\text{Al}_2\text{O}_{3.93}$
<i>C2211 surf.</i>	17.0	79.6	3.5	-
<i>C2211 1st spt.</i>	32.4	64.4	3.2	$\text{Al}_2\text{O}_{3.97}$
<i>C2211 2nd spt.</i>	33.6	66.4	<0.1	$\text{Al}_2\text{O}_{3.55}$

Figure 4.7 shows Al 2p peak position of the as sputtered sample C22. The surface chemical state and the beneath-surface chemical state of the peak are shown as squared and circled lines, respectively. Shift to lower binding energy of the

surface peak is due to the contamination at the surface. Beneath the surface, the peak position of the Al 2p is around 75.5 eV, which corresponds to the third oxidation state of Al, namely Al³⁺ [78]. This indicates the formation of Al₂O₃ for sample C22, just beneath the surface.

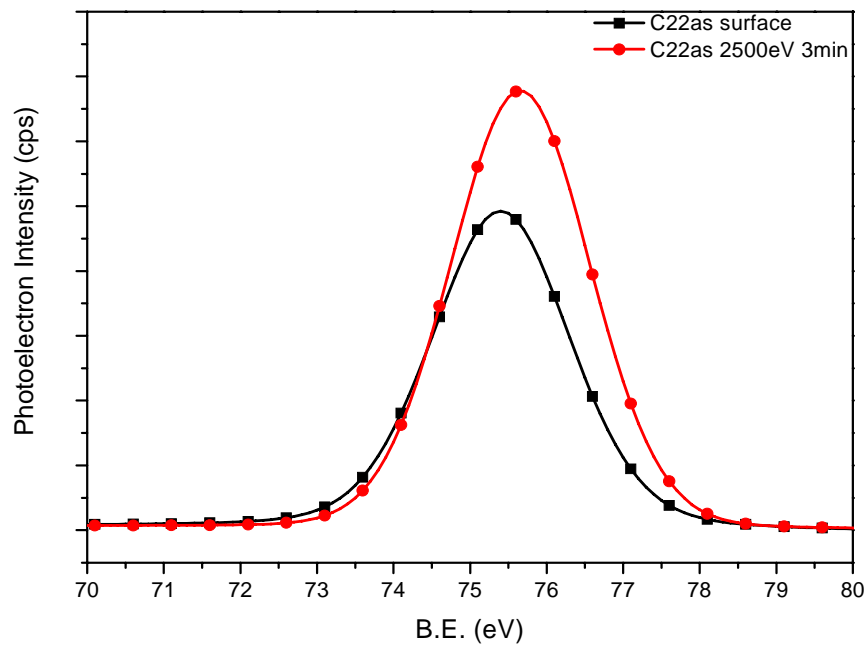


Figure 4.7. XPS spectrum of the sample C22, surface and beneath-surface measurements.

4.2.4 Photoluminescence Spectroscopy:

The characteristic emission from Al₂O₃ is well known with its different type of defects. If someone gets a spectrum which is similar to characteristic emissions, this means that the corresponding sample is “evidently” Al₂O₃. Defects in Al₂O₃ can be classified in two parts. The former is Cr³⁺ and Ti³⁺ defects [27, 79 - 81]

resulted from the fabrication of Al_2O_3 wafers and targets, the latter is oxygen related defects in the matrix. These defects are named as F , F^+ , F_2 , F_2^+ and F_2^{2+} centers [27, 82] with respect to oxygen vacancies and number of trapped electrons. These emission properties are widely studied by our group and others, as referenced above.

Figure 4.8, 4.9 and 4.10 shows the Al_2O_3 sputtered films with respect to oxygen percentage, partial pressure and annealing temperature.

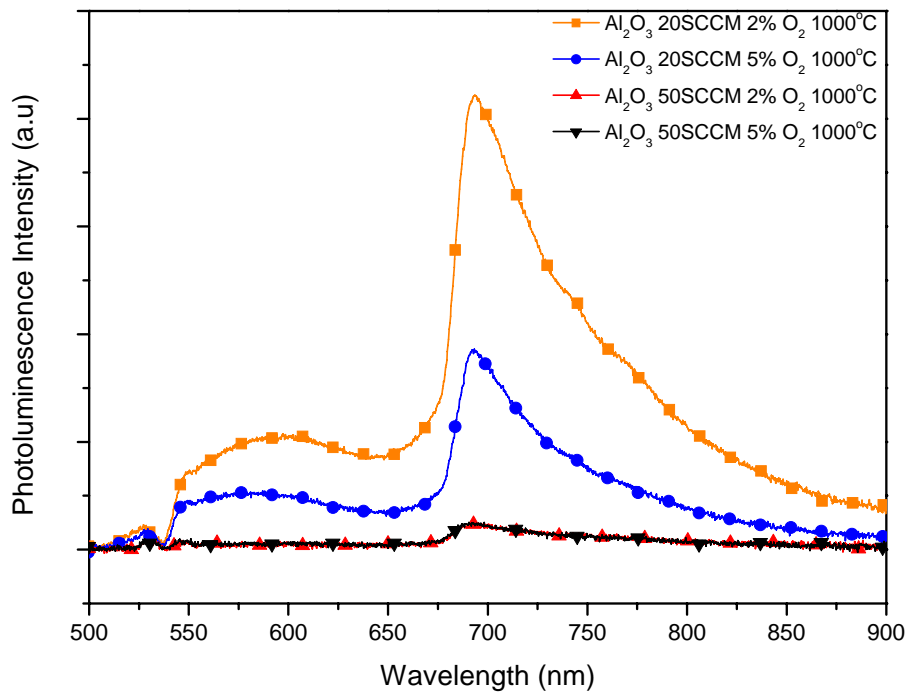


Figure 4.8. PL spectra of the sputtered samples, annealed at 1000°C for 1 hour.

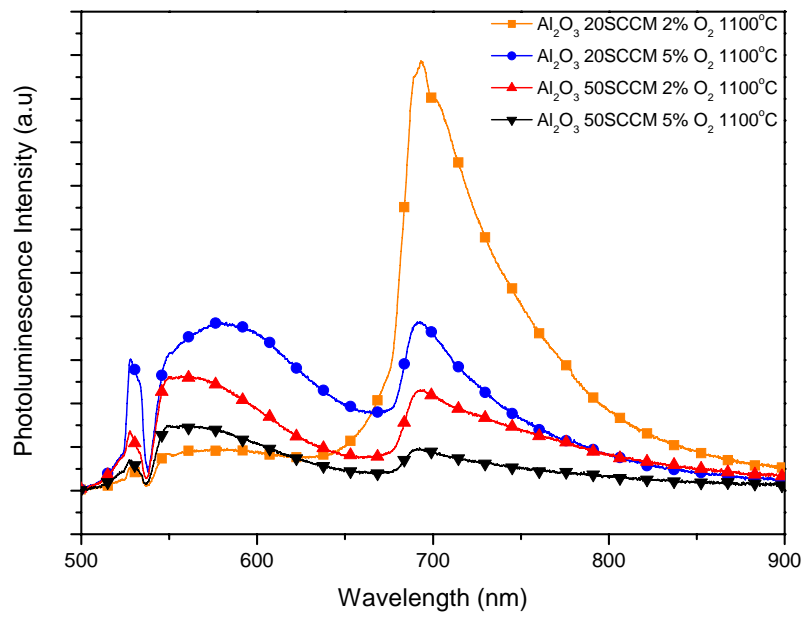


Figure 4.9. PL spectra of the sputtered samples, annealed at 1100°C for 1 hour.

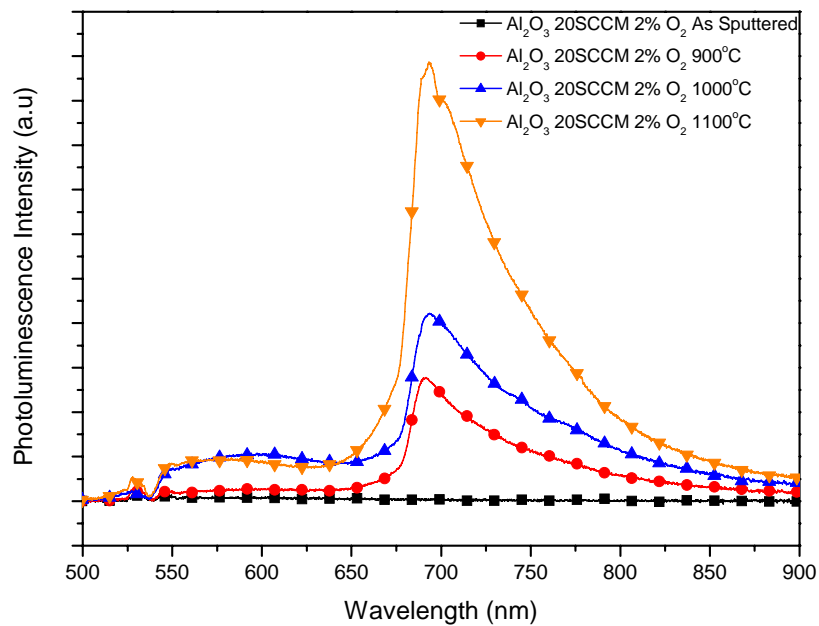


Figure 4.10. PL spectra of the sputtered sample C22, annealed at various temperatures for 1 hour.

The PL emission of all the samples exhibits similar characteristics. The most intense main peak located around 694 nm is due to the Cr^{3+} emission and the continuing shoulder down to 710 nm is from Ti^{3+} impurities. The wide and faint peak located around 600 nm is due to the F centers, oxygen vacancies with or without trapped electrons. The PL emission of all the samples increases with increasing annealing temperature. If we compare the oxygen percentages with respect to intensities we see that the emission intensity of 2% O_2 sputtered samples are higher than that of 5% O_2 sputtered samples ($I_{\text{C52}} > I_{\text{C55}}$ and $I_{\text{C22}} > I_{\text{C25}}$). Moreover, if we compare the PL emission intensities with respect to total gas low rate ($\text{Ar} + \text{O}_2$), low pressure sputtered samples have much more intense emissions than high pressure sputtered samples. By making a quick conclusion, low pressure sputtered sample with 2% O_2 has the most intense emission, namely C22. The reason for quenching the emission at high oxygen concentration samples may be due to the excess oxygen, killing the emission from Al_2O_3 .

Figure 4.10 shows the PL emission spectra of sample C22. As it is clearly seen, the as sputtered sample shows no PL emission. As the temperature increases, the typical emission of Al_2O_3 enhances and reaches to a maximum value at 1100°C annealing.

4.3 Application to MOS Based Radiation Sensors:

We have investigated the effect of Al_2O_3 dielectric in the MOS based radiation sensors [83]. The aim of this work was to investigate the dielectric sensitivity of Al_2O_3 layer with respect to classical SiO_2 layer. MOS based radiation sensors are also quite compatible with the existing CMOS technology [84, 85]. The best quality Al_2O_3 films were C22, so the same samples were sputtered at the same parameters with three different thicknesses 250, 500 and 750 nm in order to see the shift in the C-V curve at different thicknesses. It is known that the voltage shifts upon irradiation are mostly due to trapped oxide charges in the oxide [86].

The response of the MOS capacitors under gamma irradiation was studied using Co-60 gamma source from 2 to 4 Gray at a dose rate of 0.018Gy/sec. Before measurements, the samples were annealed under hydrogen atmosphere at 400°C for 30 min. in order to completely passivate the defects in the oxide/metal and oxide/semiconductor interfaces. Figure 4.11 shows the radiation induced negative shifts in the C-V curve along the voltage axis. The increase in the radiation dose results in a much more negative shift in the voltage. This negative shift is attributed to trapping of holes generated by radiation since the interface defects were passivated previously. During the irradiation with gamma rays, generated electrons move through the metal contacts and/or substrate, thus leaving a hole in the oxide. The trapping of holes in the oxide defects is the reason of this negative shift.

Figure 4.12 shows the radiation induced charges as calculated from the capacitance-voltage equation:

$$Q = \varepsilon(A/d)\Delta V \quad (4.1)$$

Where $\varepsilon=8.40\varepsilon_0$ for Al_2O_3 , A is the area, d is oxide thickness and ΔV is the flat band voltage shift due to irradiation. As it is seen from the figure 4.12, the amount of radiation induced charges is ten times larger for the MOS devices based on Al_2O_3 than SiO_2 . This is due to the charge content in the Al_2O_3 sample.

The samples in this work have good stoichiometry, sputtered with the best parameters, probed with a number of diagnostic techniques. The Al_2O_3 sputtered samples in this work exhibit great compability to MOS capacitors and have promising applications to the microelectronic technology.

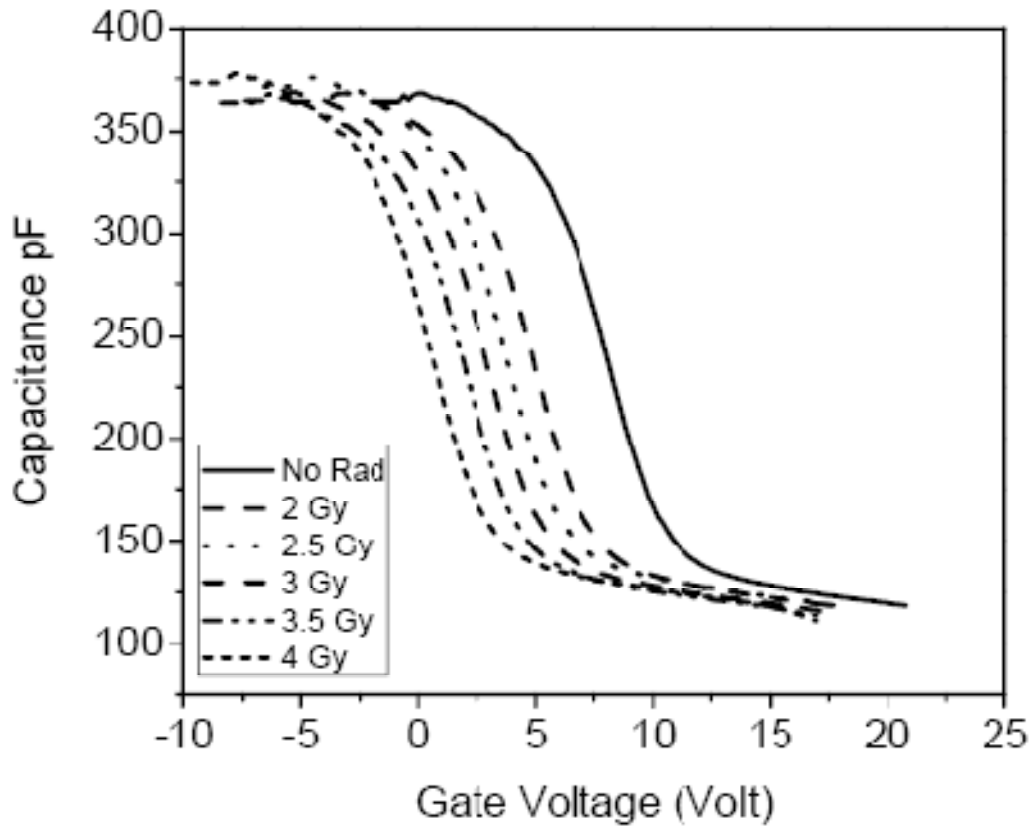


Figure 4.11 The C-V curve of the Al₂O₃ MOS capacitor before and after gamma irradiation at 1000 kHz.

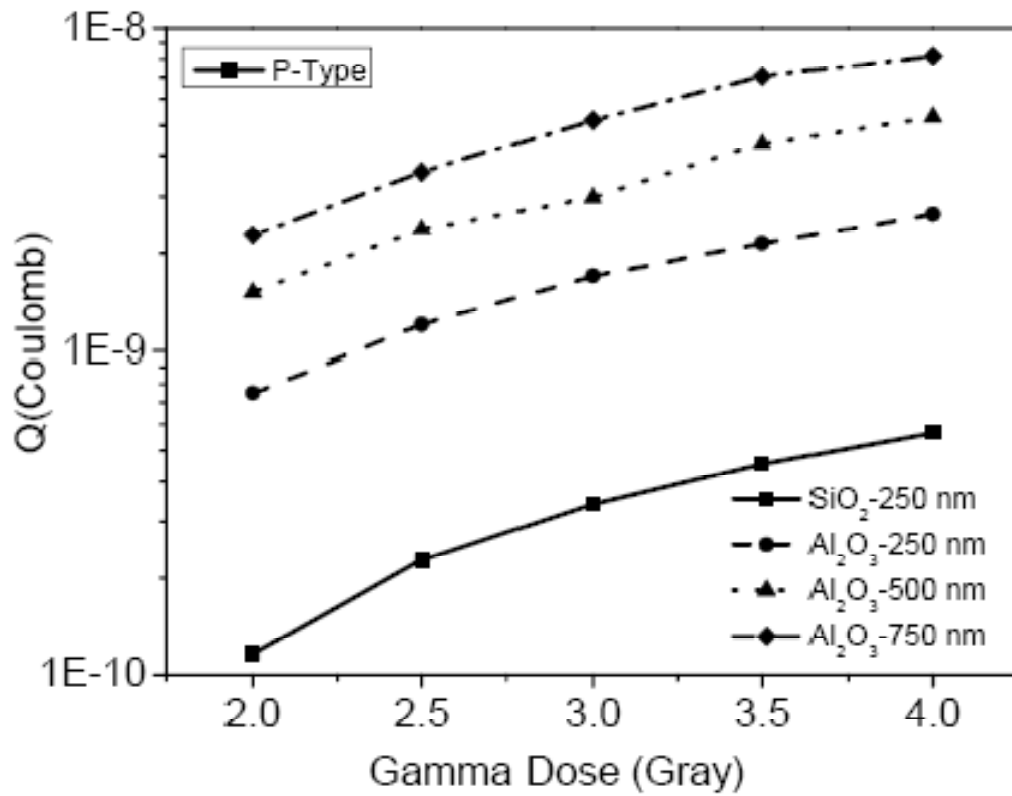


Figure 4.12. Radiation induced charges for p-type SiO₂ with 250 nm thick and Al₂O₃ with 250, 500 and 750 nm thick MOS capacitors.

CHAPTER 5

FABRICATION AND CHARACTERIZATION OF Si NANOCRYSTALS IN Al₂O₃ CO-SPUTTERED FILMS

5.1 Fabrication:

In this work, n-type Si (100) wafers with nominal resistivity of 1-10 Ωcm were used as substrates for Si/Al₂O₃ co-sputtering. Like in the previous work, the substrates were subjected to standard Si cleaning procedure in clean room conditions. In the sputtering chamber, two targets were used for fabrication. Al₂O₃ target was placed on RF magnetron and Si target was placed on DC magnetron. Electronic grade Ar (6.0) is used for co-sputtering Si and Al₂O₃ together. Five sets of samples were sputtered with respect to varying Si concentrations. Before each run, the chamber was heated at 400°C for 30 minutes in order to eliminate the negative effect of contamination such as residual water and oxygen. Substrates were held at room temperature during deposition process. RF power of Al₂O₃ was always constant at 350 W. The details of the fabrication are given in Table 5.1, Figure 5.1 and 5.2.

Samples were annealed under N₂ atmosphere for 1, 2 and 6 hours at 900, 1000 and 1100°C in order to see the onset temperature of nanocrystal formation and evolution with respect to annealing temperature and time.

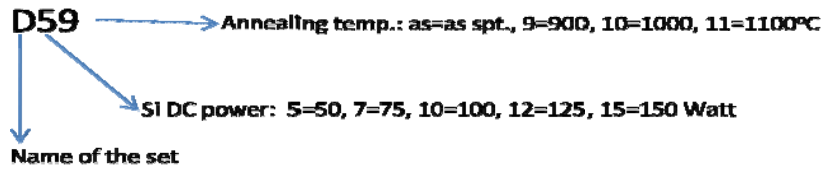


Figure 5.1. Abbreviations used in coding the sample names.

Table 5.1. Details of the sputtering procedure.

Set	Base Pr. (Torr)	Ar Pr. (Torr)	RF (W) Al ₂ O ₃	DC (W) Si	Sputter Time (min)	Thickness (nm)
D5	1.7x10 ⁻⁶	2.4x10 ⁻³	350	50	80	100
D7	1.5x10 ⁻⁶	2.4x10 ⁻³	350	75	65	100
D10	1.3x10 ⁻⁶	2.5x10 ⁻³	350	100	54	100
D12	1.2x10 ⁻⁶	2.4x10 ⁻³	350	125	45	100
D15	1.3x10 ⁻⁶	2.4x10 ⁻³	350	150	40	100

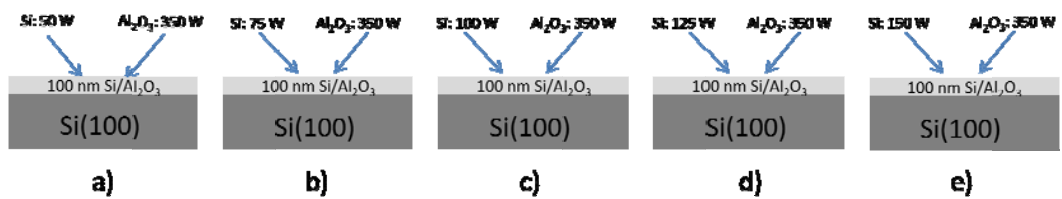


Figure 5.2. The schematics of the sputtered samples of (a) D5, (b) D7, (c) D10, (d) D12 and (e) D15.

5.2 Characterization:

Characterization process of co-sputtered Si/Al₂O₃ samples was done by using XRD, SEM, XPS and PL techniques. The effect of Si DC-power and annealing temperature on nanocrystal formation was detected by XRD. Formation of Si nanocrystals and their variation with respect to depth from the sample surface have been studied by XPS. From XPS, the variation of the Si-Si bonds with respect to depth and annealing temperature was tracked. The effect of annealing on the oxidation state of Si nanocrystals was studied in terms of higher bonding states of Si. Finally, PL Spectroscopy was employed to locate and understand the emission mechanism around 700-900 nm.

5.2.1 X-Ray Diffraction:

The samples analyzed in x-ray diffractometer were about 90-100 nm thick and the signal from Si nanoparticles cannot be detected so easily. In order to increase the signal/noise ratio, full spectrum scans and $2\Theta=28^\circ$ region scans were done in a slow scan rate.

Figure 5.3 shows the common XRD spectra of the samples. Scans were taken in the interval $10^\circ < 2\Theta < 80^\circ$ at a scan speed of $2\Theta=1^\circ/\text{min}$ with 0.1° steps. Although these scans were relatively quick, they give a general idea on the diffraction pattern of the films. There are two strong peaks located at 26.6° and 54.8° for the films of 50 W Si (D5) and 75 W Si (D7). These signals are due to the scattering from the crystalline quartz substrate. The broad signal around 24° is coming from the amorphous phases of the matrix. The latter broad signals coming from the 40° and 60° region of the films indicate mainly the formation of gamma- and theta-alumina [87] and also some other transition forms. These transition forms were also detected when analyzing stoichiometric alumina samples as shown in Figures 4.3 and 4.4. These formations are evident for all samples.

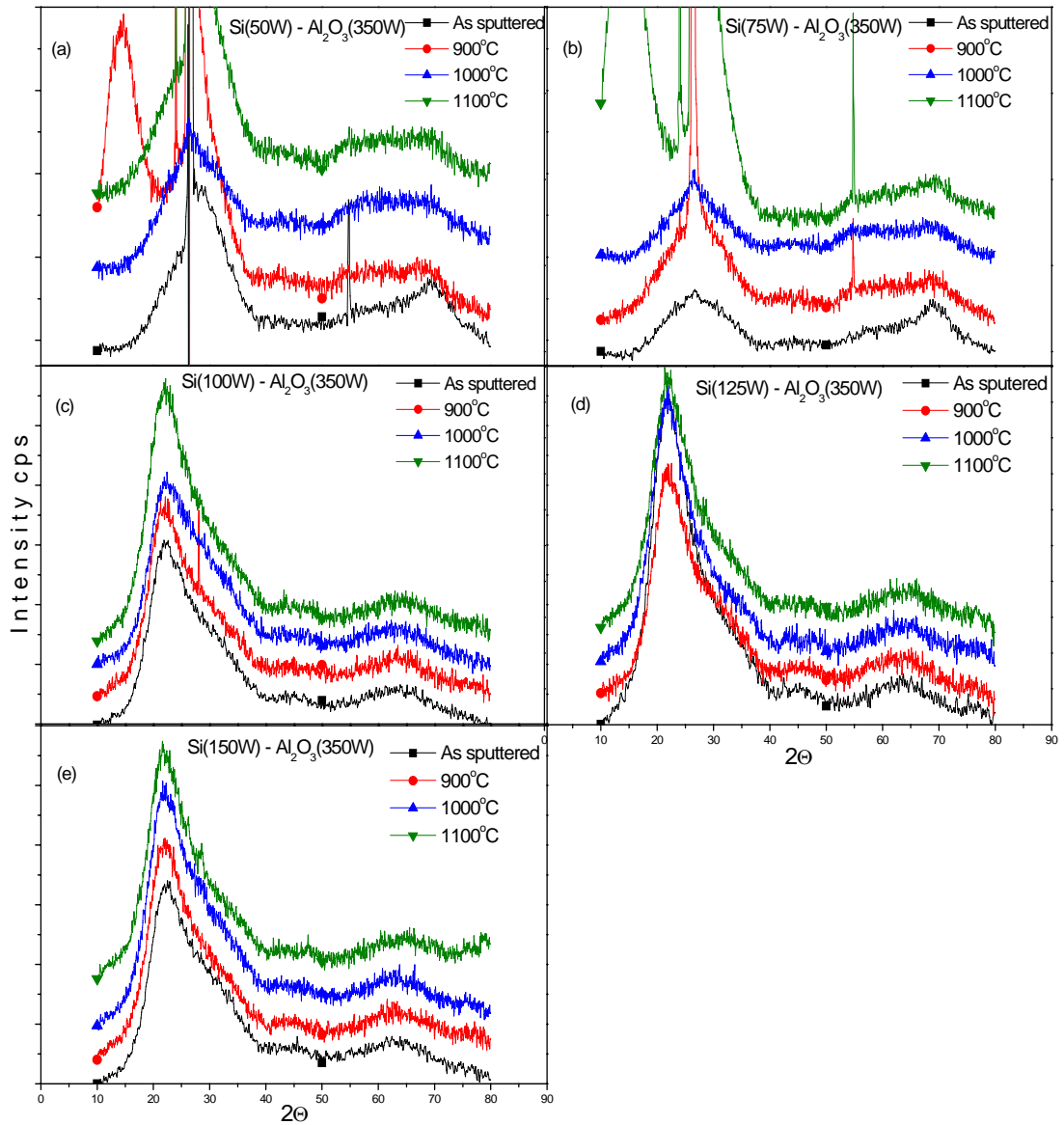


Figure 5.3. XRD spectra of the samples (a) D5, (b) D7, (c) D10, (d) D12 and (e) D15.

To get a higher resolution from the diffraction spectra, 1100°C annealed samples of D10, D12 and D15 were scanned with a scan speed of $2\Theta=0.3^\circ/\text{min}$. The resolution step was set to 0.03° . The scanning of each sample lasts for 230 min. Figure 5.4 clearly indicates the transformation of gamma- and theta- phases to eta- and alpha-alumina phases. The same tendency of the film crystallization with annealing temperature shows similar characteristics for all the samples. Since each sample contains different amount of Si concentration, we can say that Si has no evident effect on the crystallization of alumina.

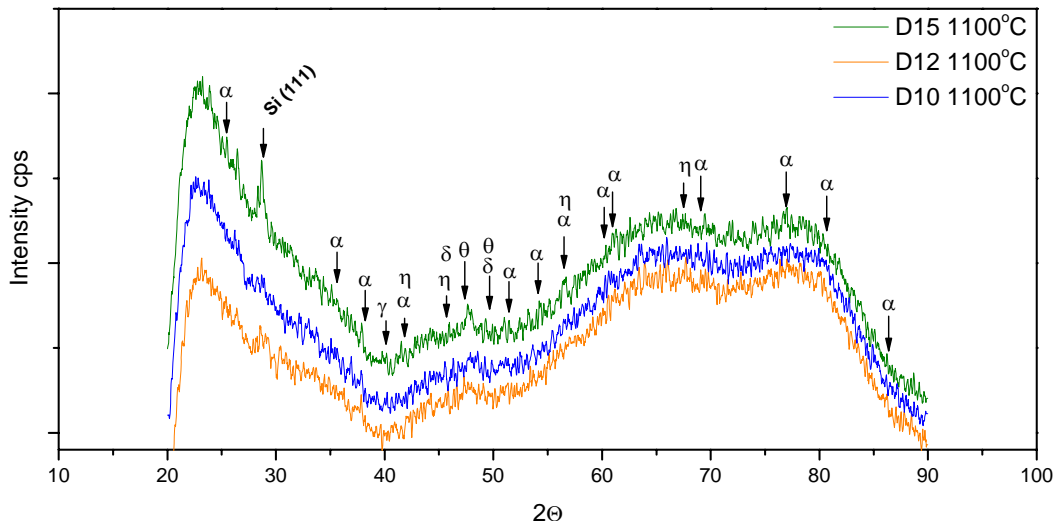


Figure 5.4. XRD spectra of the samples D10, D12 and D15.

The peak located at 28.54° is due to the scattering from Si (111), which most probably are the crystal planes of Si nanocrystals. The intensity of the peaks increases with annealing temperature and Si concentration. This means the volume of the nanocrystal depends on the Si concentration and temperature.

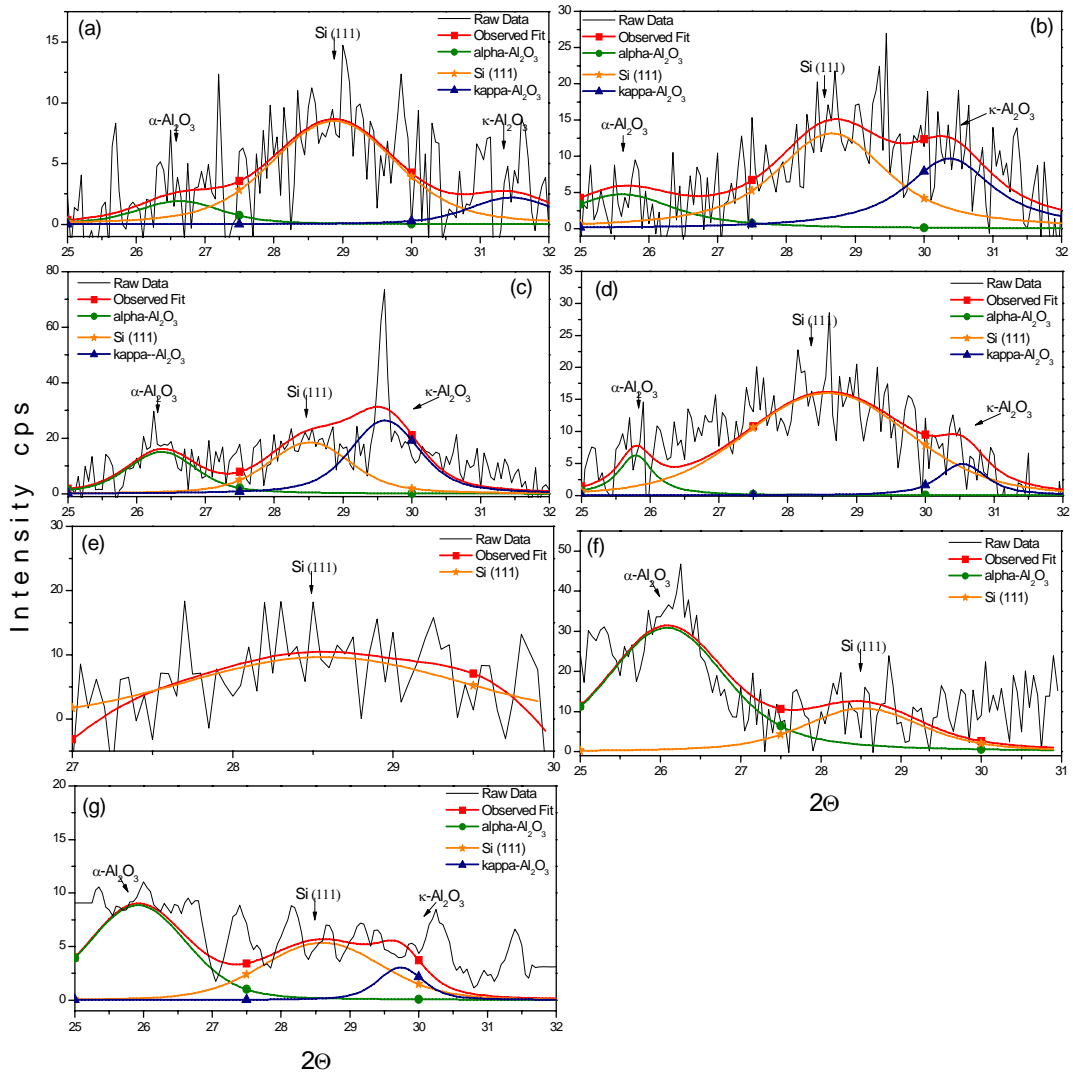


Figure 5.5. XRD peak fits around $2\theta=28.5^\circ$ region of 150 W [(a) 900° , (b) 1000° , (c) 1100°]; 125 W [(d) 900° , (e) 1000° , (f) 1100°] and 100 W [(g) 1100°] Si target power sputtered samples.

Figure 5.5 shows the region between $25^\circ < 2\Theta < 32^\circ$, where the Si (111) peak is located. The standard XRD scans were performed at a scan speed of $2\Theta = 0.1^\circ/\text{min}$ with steps 0.05° . The obtained XRD spectra are the average of three scans which last 210 minutes for each sample. In the spectrum, Cu $K\alpha_2$ lines were eliminated by using Rachinger's method assuming that $K\alpha_1$ lines were two times more intense than $K\alpha_2$ lines [88]. It is expected that by increasing the Si DC-power, more intense and well pronounced Si (111) will appear. This is the case in Figure 5.5, in which Si nanocrystal size and the surrounding matrix evolves with annealing temperature and Si DC-power. For 150 W and 125 W Si sputtered samples, the increasing annealing temperature creates higher number of nanocrystals resulting to an increase in the overall Si (111) peak intensity. The peaks located around 26° and 30° are from the matrix. The transformation phases are alpha- and kappa- Al_2O_3 , respectively. See how the temperature dependence of the recovering of matrix is obvious from the figures. For 900° annealed samples, the phases are not so obvious but for 1100°C annealed samples, phase separations are clearly visible, like in the case of Si (111). Since alumina has various peaks and some alpha- and kappa- peaks are very close to the Si (111) peak position, it is not so easy to define the phases and Si clusters from the raw data. But by making careful examinations, the size of the Si nanocrystal can be calculated from the broadening of the Si (111) peak located at 28.54° . The peak position of Si nanocrystals can change from 28.51° to 28.87° . From the shift in the XRD peak position, lattice constants and elastic strains can be calculated.

The sizes of the nanocrystals were estimated by using Scherrer's method, given in Equation 3.3. The Scherrer's constant K is taken as 0.893 which is true for spherical nanocrystals [88]. Table 5.2 demonstrates the physical information, obtained from the XRD scan of Si/ Al_2O_3 co-sputtered films. In the table, "Si DC" is the DC-power of Si target during sputtering, "T" is the annealing temperature under N_2 ambient for 1 hour, " 2Θ " is the Si (111) peak position, " β " is the integral breadth (FWHM) of the diffraction peak, "Size" is the nanocrystal size in nanometers, "d" is the Bragg plane spacing, "a" is the lattice constant and finally " $\Delta a/a$ " is the percentage of lattice parameter shift with respect to bulk Si (111)

peak. It is seen from that, the nanocrystal size increases with increasing annealing temperature and Si DC-power. The largest nanocrystal mean sizes were obtained from 150 W, 1100°C annealed sample. Mean sizes of the largest nanocrystals were about 5.75 nm and the smallest nanocrystals were about 2.90 nm.

The estimated lattice constants of Si nanocrystals were always smaller than the bulk value which is 5.43Å (Table 5.2). This mentions there exists a stress, which compresses the nanocrystals.

Table 5.2. The physical parameters, gathered from the XRD scans.

Si DC (W)	T (°C)	2 Θ	β (2 Θ)	Size (nm)	d(Å)	a(Å)	Strain	$\Delta a/a(\%)$
150	1100	28.5154	1.4145	5.75	3.1265	5.4153	2.71×10^{-3}	0.271
150	1000	28.6566	1.9395	4.19	3.1114	5.3891	7.53×10^{-3}	0.753
150	900	28.8735	2.1268	3.83	3.0885	5.3494	1.48×10^{-2}	1.484
125	1100	28.5227	1.7418	4.67	3.1257	5.4139	2.97×10^{-3}	0.297
125	1000	28.5645	1.9908	4.08	3.1212	5.4061	4.40×10^{-3}	0.440
125	900	28.5783	2.8022	2.90	3.1197	5.4035	4.88×10^{-3}	0.448
100	1100	28.5964	2.0310	4.00	3.1178	5.4002	5.49×10^{-3}	0.549

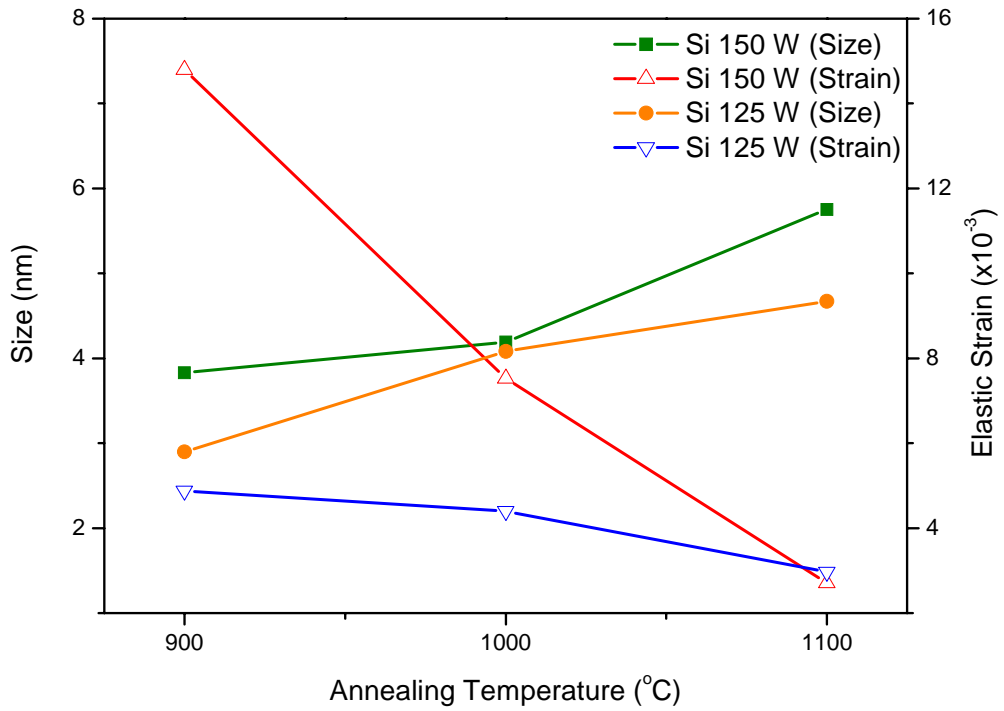


Figure 5.6. Variation in the nanocrystal size and elastic strain with respect to annealing temperature and Si DC-power.

Figure 5.6 shows the variation in the nanocrystal size and elastic strain with respect to annealing temperature and Si DC-power. Nanocrystal size variation is given by filled symbols and the strain variation is given by open symbols. For low annealing temperatures, there exists considerably high strain on Si nanocrystals. This might be due to the unstable transition forms of Al_2O_3 matrix, which have larger lattice constants with respect to $\alpha\text{-Al}_2\text{O}_3$. For example $\eta\text{-Al}_2\text{O}_3$ has a hexagonal structure with $a=b=7.8490 \text{ \AA}$, $c=16.183 \text{ \AA}$; $\theta\text{-Al}_2\text{O}_3$ has a monoclinic b axis with $a=11.740 \text{ \AA}$, $b=5.720 \text{ \AA}$, $c=11.240 \text{ \AA}$; $\gamma\text{-Al}_2\text{O}_3$ has a cubic structure with $a=b=c=7.900 \text{ \AA}$ and $\chi\text{-Al}_2\text{O}_3$ has a cubic structure with $a=b=c=7.950 \text{ \AA}$. The stable $\alpha\text{-Al}_2\text{O}_3$ has a hexagonal structure with $a=b=4.758$

\AA and $c= 12.991 \text{ \AA}$. Low temperature annealed films have transition forms, which apparently have much more lattice mismatch with Si clusters. When the temperature increases, the stability also increases and the percentage of lattice mismatch between the matrix and Si nanocrystals decreases. This is the main reason explaining why relaxation of compressive strain occurs with high temperature treatment. From these data, we can say that the most suitable, strain free nanocrystals were formed in 150 W Si sputtered and 1100°C annealed samples.

5.2.2 Photoluminescence Spectroscopy:

PL of the Si – Al_2O_3 co-sputtered films exhibits variation and this variation strongly depends on the Si DC-power. In the Figure 5.7, the graphs are ordered from the lowest to the highest Si DC-power. For 50 W (D5) and 75 W (D7) sputtered samples, there are two main emission peaks; the broad one, which is located around the circa 600 nm, and the sharp one, located at 694 nm. The peak around 600 nm has a strong emission at 900°C , and the intensity of this emission decreases with increasing annealing temperature. The latter peak located at 694 nm is not evident at 900°C but at 1000 and 1100°C . The explanation of these emission behaviors requires a careful examination and discussion.

Increasing annealing temperature makes the matrix recover itself by decreasing the density of radiative and non-radiative defect centers. Decreasing intensity of the peak around 600 nm with increasing annealing temperature clearly indicates its defect related nature. The main defect type in alumina is oxygen related; called F centers and it is known that, in the presence of F type defects, UV and visible emission is obtained from the matrix depending on the type of the F centers. The types of these defects are oxygen divacancies with four, three and two electrons (F_2 , F_2^+ and F_2^{2+}) [89] and oxygen vacancies with two and one electrons (F and F^+) [90]. The representations of the energy diagram of F centers are given in Figure 5.8 [91]. The peak around 600 nm from our samples is hence, coming from

the F_2^{2+} centers (oxygen divacancies with two trapped electrons), present in the Al_2O_3 matrix.

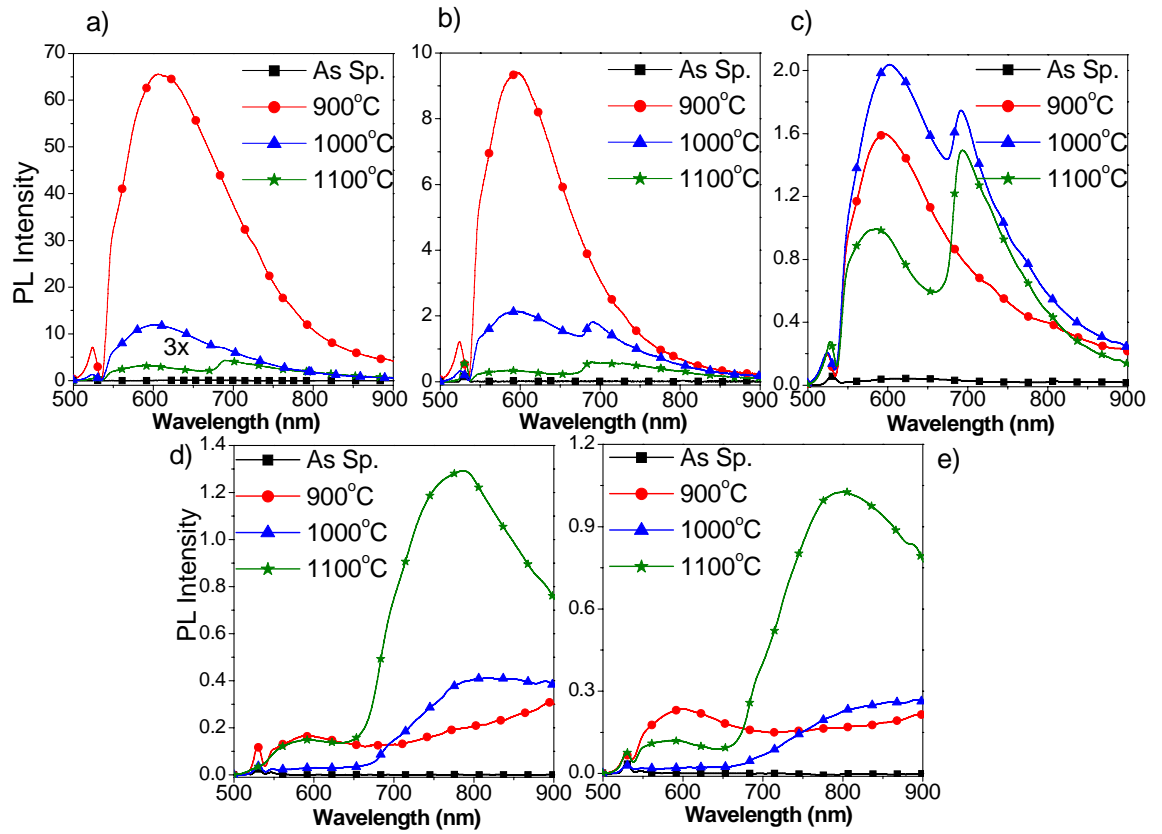


Figure 5.7. PL Spectra of the samples. (a) D5, (b) D7, (c) D10, (d) D12 and (e) D15

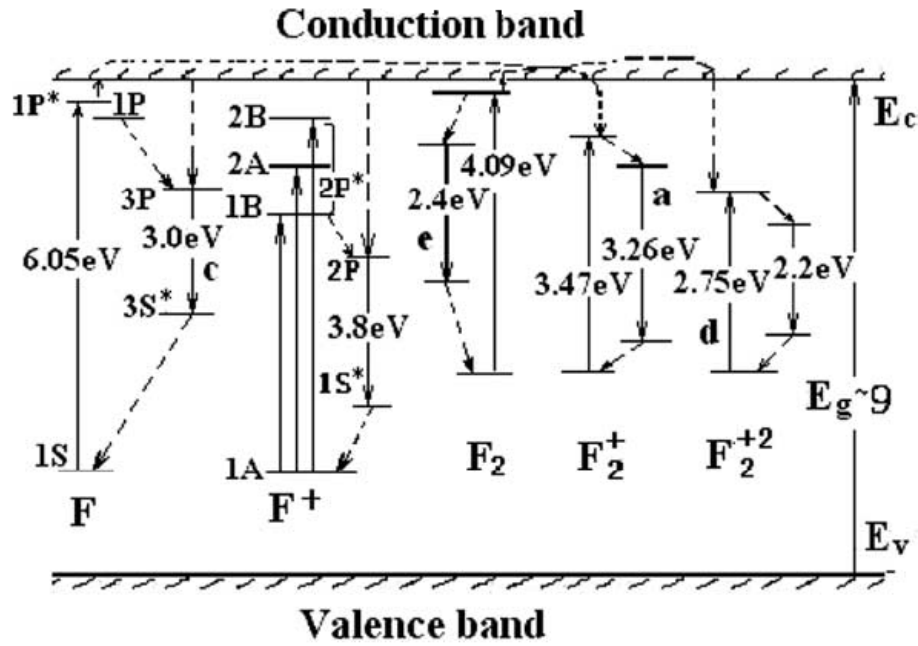


Figure 5.8. Flat band diagram of Al₂O₃ summarizing the relative energy positions of F type centers at different charge states. Adopted from Ref. 91.

Al₂O₃ lattice contains Cr₂O₃ in the order of part per million. Cr³⁺ is a natural substitutional metal atom to Al³⁺ [92]. By the relaxation of Cr³⁺ to its ground state at room temperature, a sharp luminescence doublet is obtained at 692.9 nm (1.789 eV) and 694.3 nm (1.786 eV) which referred to as R₁/R₂ doublets [93]. So the peak seen around 694 nm is a characteristic emission coming from Cr³⁺ centers [27]. Recovering of Cr₂O₃ with annealing temperature also indicates the simultaneous recovering of Al₂O₃ matrix since the F center related emissions decreased with annealing temperature. So the emission from 694 nm is a good indication of formation of high temperature Al₂O₃.

For the 100 W sputtered sample (D10) in Figure 5.7, the intensity of Cr³⁺ becomes comparable to F center emission and a lower shoulder became evident beyond 700

nm. The intensity of the F centers is dramatically decreased and an emission between 700 – 900 nm was visible for 125 W (D12) and 150 W (D15) sputtered samples. For a specific sputtering power, the intensity of the peak increases while the peak position was almost remained constant. But when the Si power was increased, a shift to lower energies was observed. Sample D12, which was sputtered with a Si DC-power of 125 W, has a peak position around 775 nm while sample D15, sputtered at 150 W, has its position around 800 nm. The shift in the PL peak position is due to the confinement of electron wave motion in tiny small structures, namely Si nanocrystals. The formation and evolution of Si nanocrystals with (111) planes, which was tailored by XRD, is the main reason of this size dependent luminescence. Here, variation of size is clearly a function of DC-magnetron power. Cr^{3+} peak is still visible in the form of a shoulder in these samples. PL spectra of the 100, 125 and 150 W sputtered samples probably have emission tails in the near infrared region which cannot be detected with our CCD. 900° annealed 125 and 150 W samples exhibit an increase through the infrared part. The reason of this emission may be from partly amorphous Si clusters or lattice defects due to huge compressive strain discussed in the previous section.

Figure 5.9 shows the variation of the typical PL emission with respect to annealing time. As it is seen from the figure, the intensity of the emission was increased while no clear shifts were observed. According to this graph, longer annealing time does not create larger nanocrystals or Ostwald ripening of small nanocrystals, but increase the number of same sized nanocrystals. This might be the main reason of this stable increase. The emission is most probably from the band to band transitions of Si nanocrystals [26].

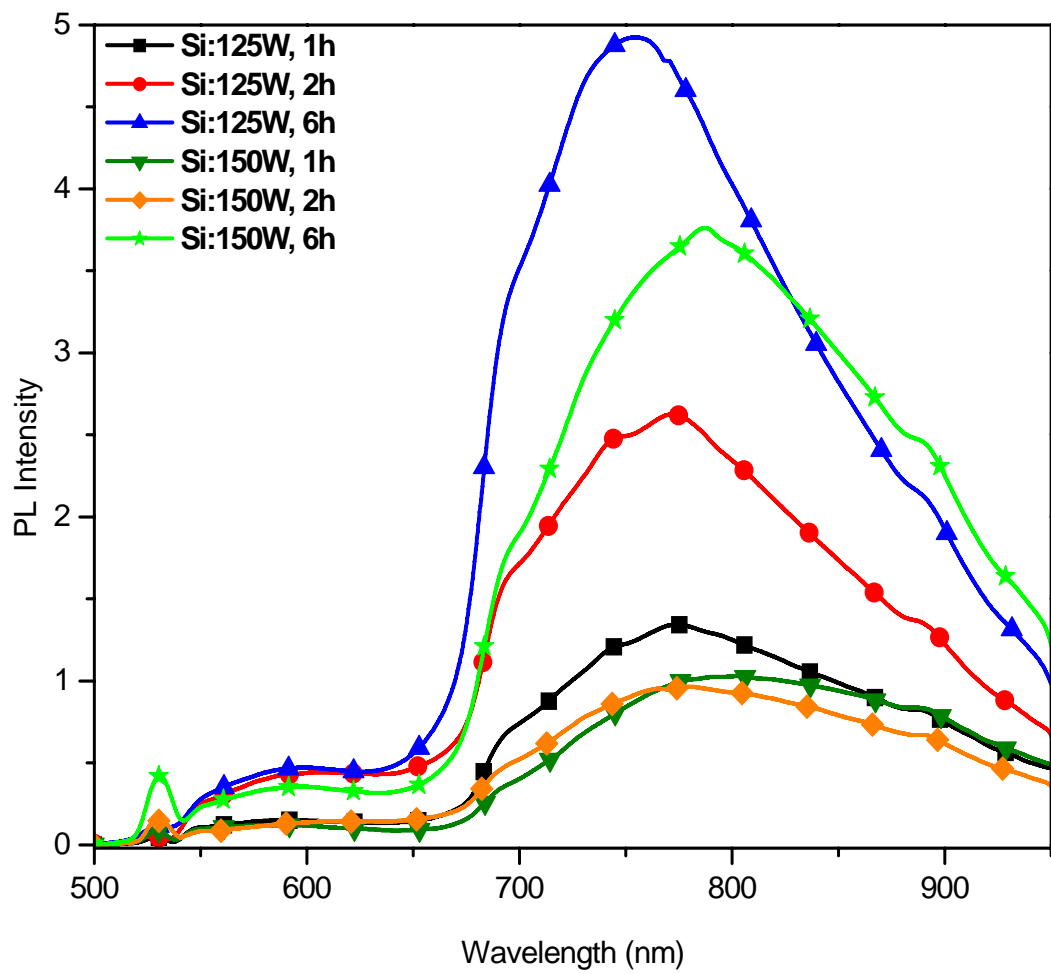


Figure 5.9. Variation of the PL emission spectra with respect to time.

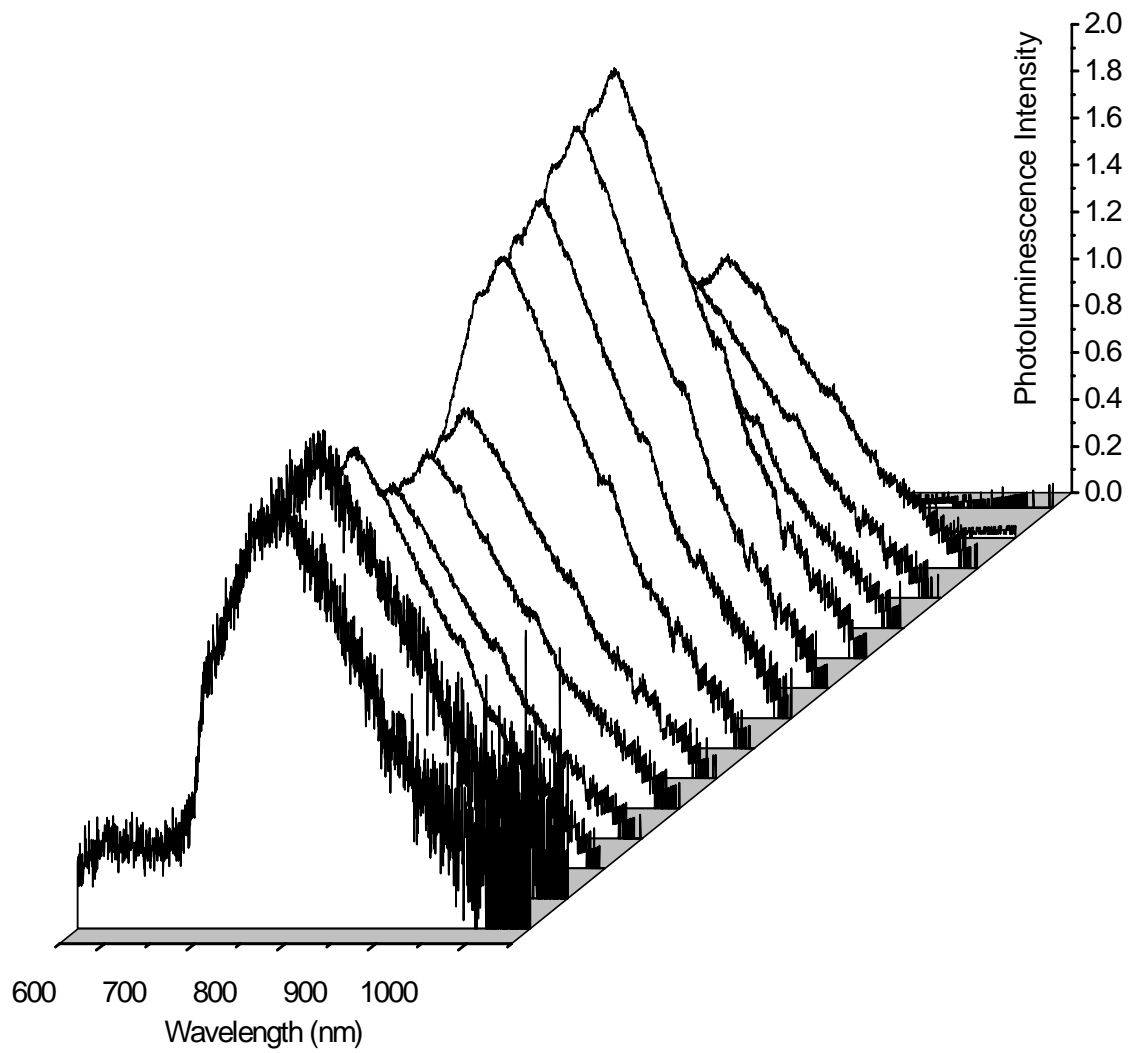


Figure 5.10. PL depth profile of the 150 W sputtered and 1100°C annealed sample.

For the depth profile investigation, 150 W sputtered 1100°C annealed sample was dipped into dilute HF solution. After each etching step, PL spectra were measured. The experiment was processed until there was no signal from the sample meaning that the substrate surface is reached. Figure 5.10 shows depth profile variation of the corresponding sample. The first thing that can be inferred from the graph is the stable peak position of the maximum PL emission point with respect to depth. With depth, PL emission intensity is stable up to a certain point. After that point, the emission is dramatically increased. The emission is totally quenched by reaching the film substrate interface. In order to identify the origin of the PL more clearly, XPS depth profile measurements were conducted. Still from the figures presented in this section and the XRD section, the emission mechanism is most probably from the Si nanocrystals formed in the matrix but the chemical status should be identified by XPS.

5.2.3 X-Ray Photoelectron Spectroscopy:

XPS was developed in order to investigate the chemical structure of the atoms in Si/Al₂O₃ co-sputtered films. A Specs 200 system was used for the XPS measurement. Measurements were taken under UHV conditions. For spectroscopic analysis, a hemispherical electron analyzer was used which is operating with a focusing lens at a spot size of 750 μm. Excitation source for our experiments was Mg K_α with a power of 200 W. Depth profile measurements were done with accelerated Ar⁺ ions. Acceleration voltage was 2000 eV for each layer and the time between two successive sputtering was 12 minutes. Energy resolution of the measurement was set to 0.1 eV. Background correction and also peak fitting of the raw data were processed by using XPSPEAK95 software [94]. XPS measurements were done for Al 2*p*, C 1*s*, O 1*s* and Si 2*p* states. Binding energies of these states are 75.6 eV (for Al₂O₃, not shown here), 284.4 eV, 532.5 eV and 99.8 eV, respectively.

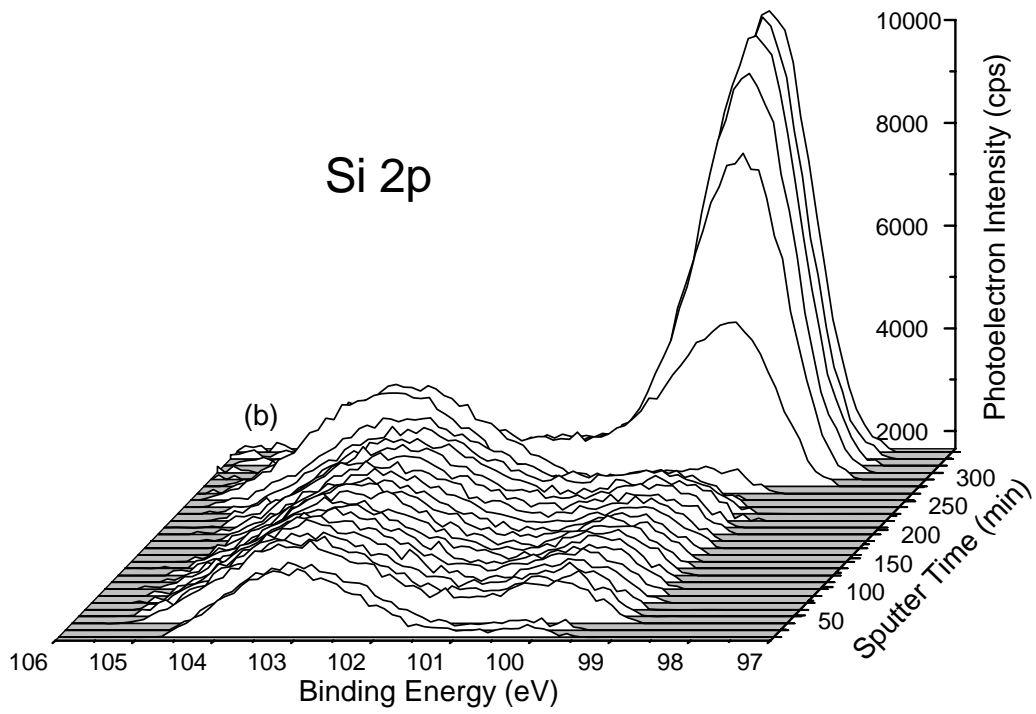
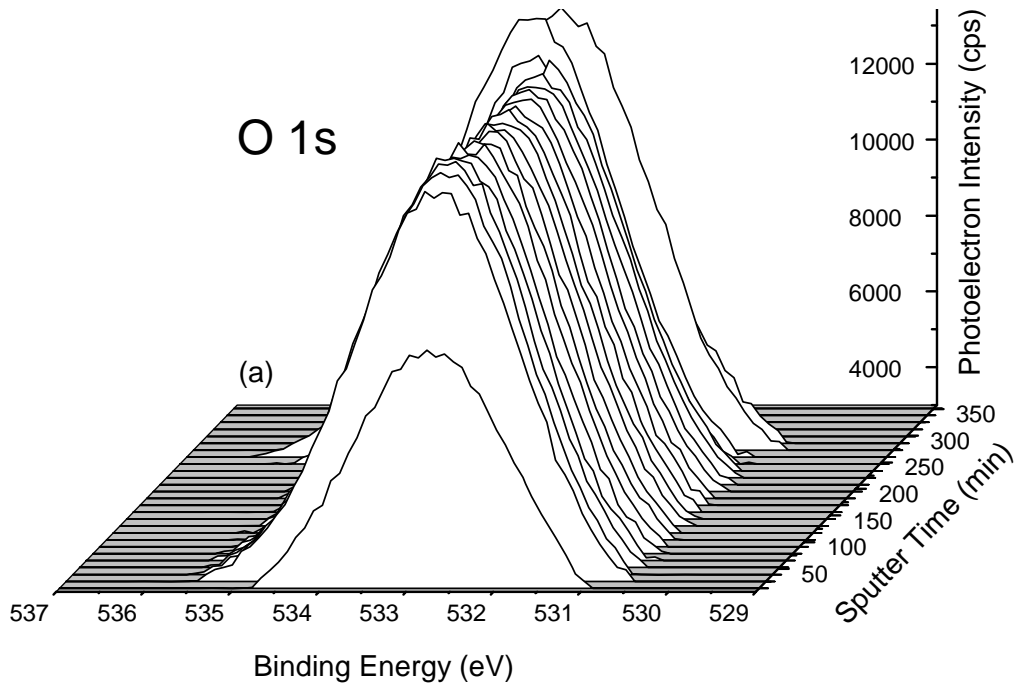


Figure 5.11. XPS depth profiles of the as sputtered 150 W sample (a) O 1s and (b) Si 2p.

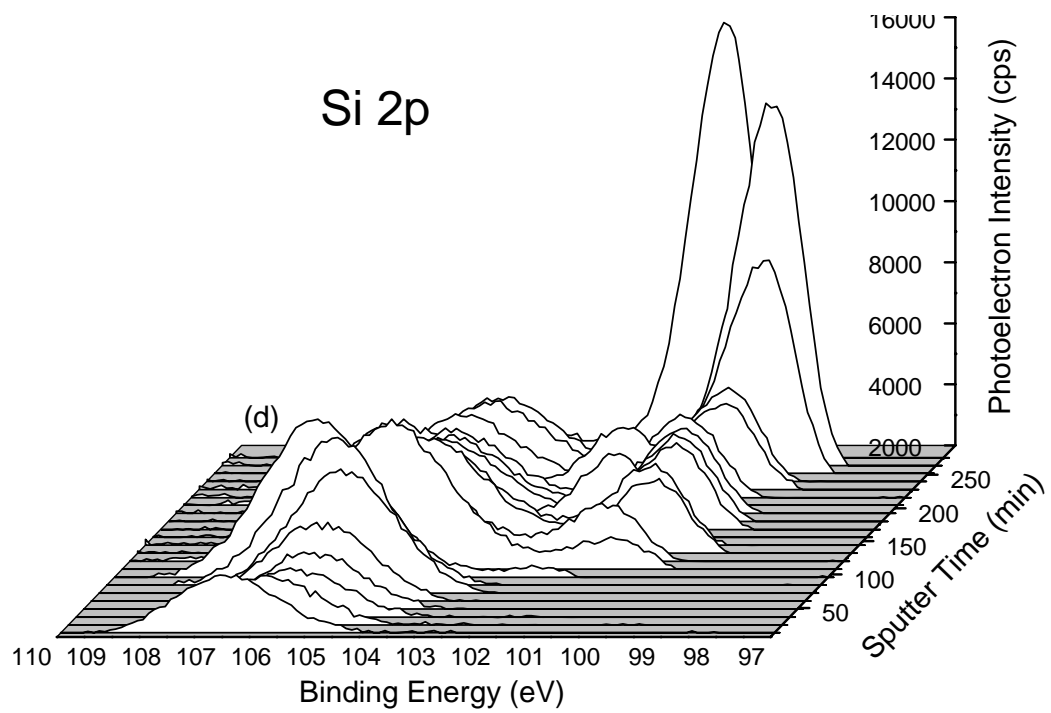
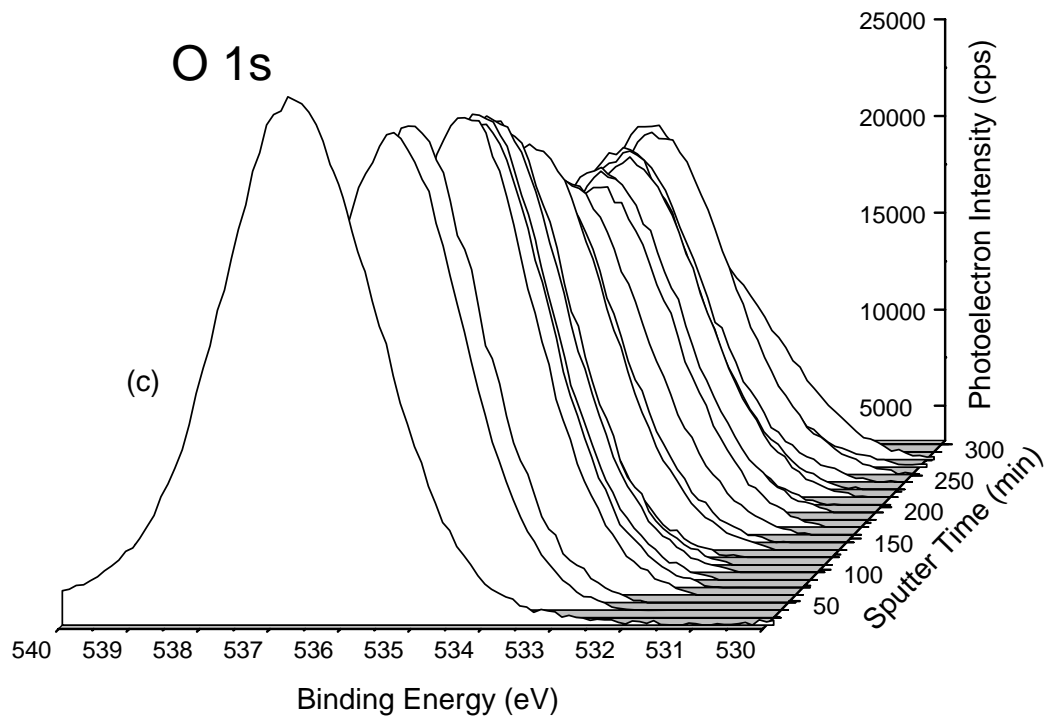


Figure 5.12. XPS depth profiles of the 1100°C annealed 150 W sample (a) O 1s and (b) Si 2p.

Figures 5.11 and 5.12 represent the depth profile measurements of the as sputtered and 1100°C 150 W sputtered samples, respectively. For the as sputtered sample shown in Figure 5.11 (a), the oxygen concentration has a peak exactly at 532.5 eV and this peak position remains constant throughout the film. Ignoring the first layer, which was facing with open ambient conditions all the time, the oxygen concentration is always constant and completely removed at the interface. As sputtered sample in Figure 5.11 (b) has Si⁰ and the higher oxidation states of Si (Si¹⁺, Si²⁺, Si³⁺, Si⁴⁺) almost at constant proportions through the film. However, the main Si species in the film is Si⁴⁺. After some certain depth, Si⁰ concentration is increased, and a sharp peak is appeared. This is the interface region between the film and substrate.

After high temperature annealing at 1100°C, the chemical structure of the film is completely changed. During annealing, the residual oxygen in the carrying N₂ gas might have oxidized the Si in upper layers of the film. The evidence of the oxidation can be seen by the increased intensity of O 1s peak beneath the surface. The effect of oxidation can also be inferred from Si 2p spectrum, in which the layers beneath the surface are fully turned into Si⁴⁺. The fourth oxidation state of Si is the evidence of SiO₂ formation. From these changes we can say that the high temperature treatment is a strong driving force in the equilibrium dynamics of the film.

At high temperature treatment, the phase separation of the intermediate oxide states (Si¹⁺, Si₃O; Si²⁺, SiO; Si³⁺, Si₂O₃) is taking place. At this temperature, higher oxidation states tend to form SiO₂ while lower oxidation states of Si tend to form Si⁰ which are thermodynamically much more stable than intermediate states. Formation mechanism is the exchange of oxygen and silicon between Si₃O, SiO, Si₂O₃; leading to formation of stoichiometric SiO₂ and Si nanocrystals. According to this phenomenon, the transformation of the intermediate states should result an increase in the intensity of Si⁴⁺ and Si⁰ signals. The situation is showed in Figure 5.13. Enhancing of Si⁴⁺ and Si⁰ signals and quenching of Si¹⁺, Si²⁺ and Si³⁺ signals are clearly seen before and after annealing.

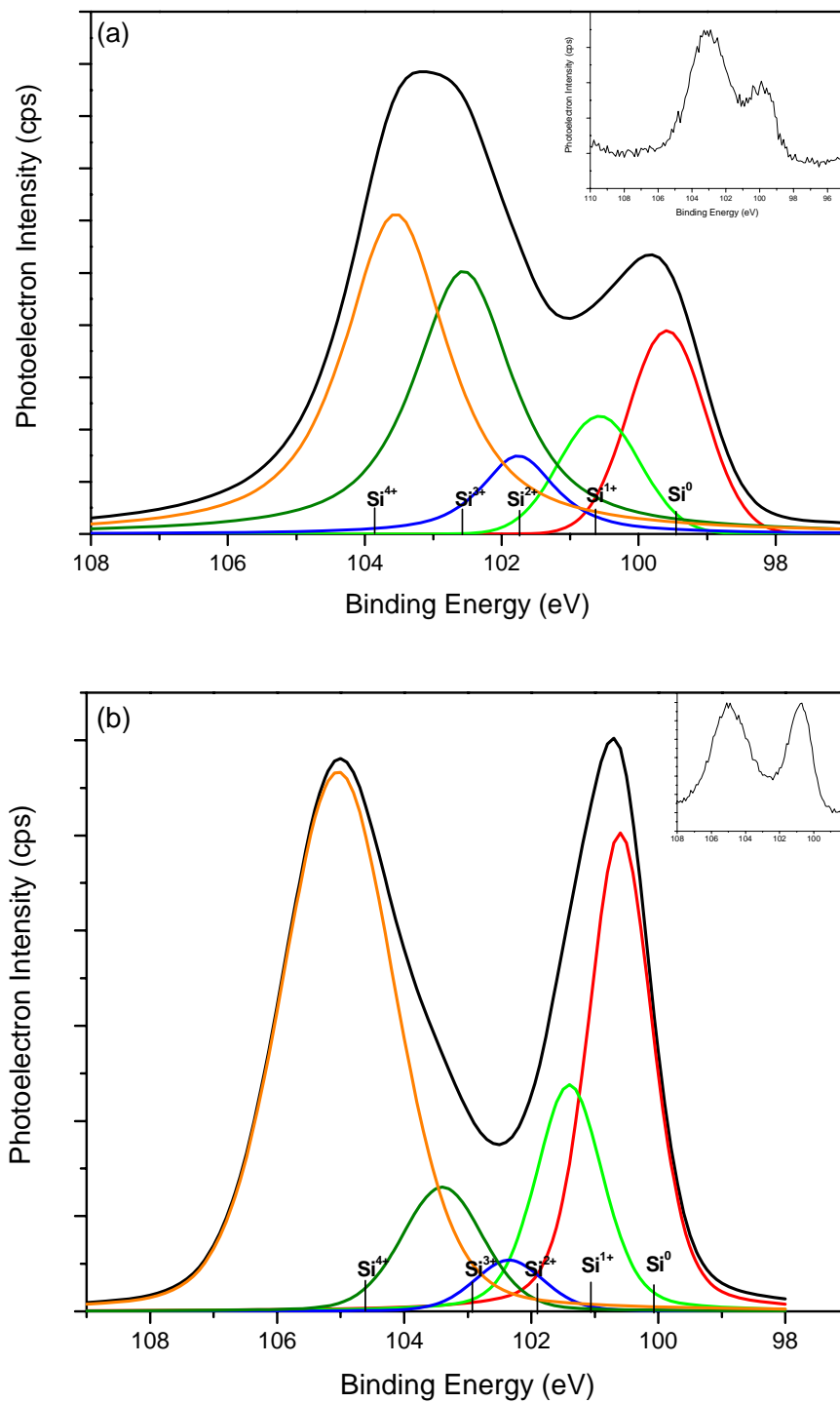


Figure 5.13. Deconvolution of Si 2p signals of (a) as sputtered and (b) 1100⁰C annealed sample. Identical layers (17th layers from the top surface) were chosen from Fig. 5.11 (b) and 5.12 (d). The effect of annealing was increased the Si and SiO₂ density. Inset shows the raw data.

By comparing Figure 5.12 (d) and 5.13 (b), we can say that coalescence of Si atoms to form nanocrystals was occurred at high temperature below a certain depth. The phase separation of stoichiometric SiO₂ and Si in Al₂O₃ matrix is evident in both of these figures. Here the stoichiometric SiO₂ possibly be in the form of a shell structure surrounding the Si nanocrystals. Although we still see Si¹⁺, Si²⁺ and Si³⁺ signals in the XPS spectra even after annealing, their intensities are significantly reduced. Further annealing may reduce the intensities of these peaks while forming new nanocrystals and therefore, the PL intensity is increased for a specific dose [93]. Depending on the state of Si, these oxidation states might be located in the nanocrystal-shell (Si/SiO₂) or shell-matrix (SiO₂/Al₂O₃) regions.

Figure 5.14 shows the variation in the atomic concentrations and PL intensity with respect to sputter time and depth for 150 W sputtered sample. PL depth profiling was performed by dipping the sample into dilute HF solution. Etching process was repeated until there were no PL emissions from the sample. The variation was referenced to the maximum of the main peak centered on 800 nm. In Figure 5.14, the concentrational variation of O 1s is almost constant while Al 2p and Si 2p show abrupt changes. The top 30 nm of the annealed film contains mainly Al₂O₃ and little amount of Si. Figure 5.12 (d) indicates the existence of only Si⁴⁺ within the upper layers. This is apparently due to the oxidation of the surface layers at high temperature. The variation of the PL intensity is directly related with the variation of Si 2p concentration. The PL intensity increases with Si⁰ concentration and this strongly indicates that the PL band in the range of 700 – 900 nm is related to the presence of Si nanocrystals. The correlation between PL intensity and Si⁰ concentration and the existence of nanocrystals tailored from XRD and PL revealed the origin of the emission was from the Si nanocrystals.

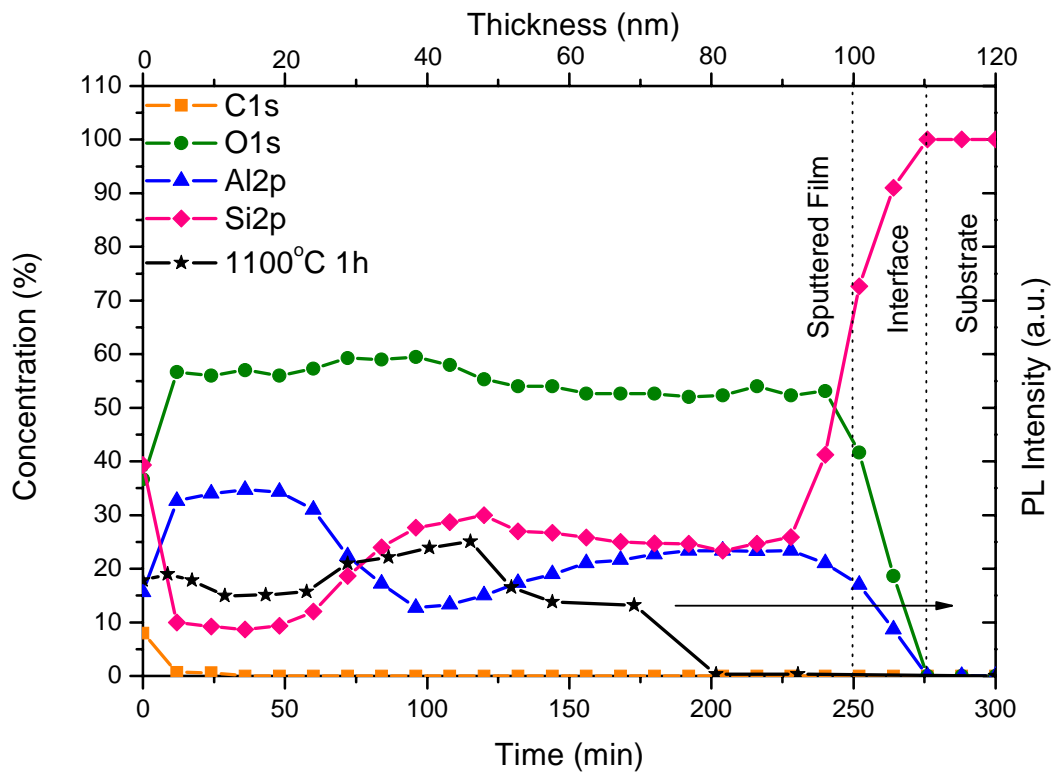


Figure 5.14. The variation in the atomic concentrations and the PL intensity of the 1100°C annealed sample in Figure 5.13 with respect to sputter time and depth. The PL etching was referenced to the maximum of the main peak around 800 nm.

CHAPTER 6

CONCLUSIONS AND FUTURE WORK

In this work, Al₂O₃ and Si/Al₂O₃ films were fabricated by using RF magnetron sputtering and RF & DC magnetron co-sputtering techniques, respectively. Post annealing at different temperatures was done in order to investigate the evolution of Al₂O₃ matrix and/or Si nanocrystals. Spectroscopic techniques were developed in order to probe the physical and chemical structures of the samples. By using these techniques, it is shown that Al₂O₃ films can make better dosimeter than SiO₂ and under certain conditions Si nanocrystals can emit efficient light in the Al₂O₃ matrix.

XRD was developed to identify the crystalline transition phases of Al₂O₃ forms at different annealing temperatures. It is found that as the temperature increases, the transition forms dynamically evolve, turning into more stable phases. At 1100°C, most of the film contains polycrystalline and partly amorphous α -Al₂O₃ which is the most stable form of alumina. For the Si containing samples, a very broad peak has emerged from the region $2\Theta=28.5^\circ$, where it corresponds to the scattering from the successive (111) planes of Si clusters. This clusters are most probably be crystalline, namely they are Si nanocrystals. The broadening of the peak increases with decreasing annealing temperature and decreasing Si dose in the film. This tells us the decreasing of size with increasing peak broadening. As the temperature increases, nanocrystal sizes consistently increases. Size calculation of the nanocrystals was performed by using Scherrer's formula. The estimated sizes were changing between 2.90 to 5.75 nm. These values are well compatible with the exciton Bohr radius of Si which means that the nanocrystals are in the strong confinement regime.

PL spectroscopy was used to analyze the optical properties of Al₂O₃ films. The fingerprints of alumina emission are detected from the high temperature annealed samples. These emissions were F center related defects and Cr³⁺ (R₁/R₂) emission doublets. The partition of oxygen is a crucial factor in forming alumina structure. It is found that 2% oxygen gives better results with respect to 5% oxygen. At high oxygen doses, the film was largely oxidized and characteristic emission from alumina is quenched. Formation of Si nanocrystals was also detected in terms of optical emission properties. The size dependent emission with temperature and Si dose was detected from the samples. By comparing the results from XRD measurements, as the size of the nanocrystal is increased, the peak position of the PL emission is red-shifted. Whenever the size is decreased, a blue-shift is observed. This is apparently the quantum confinement of the Si nanocrystals and the emission is due to the exciton recombination in the Si nanocrystals.

Formation of Si nanocrystals and the evolution of the host matrix with respect to depth were studied by XPS. Formation of Si nanocrystals is identified from the presence of Si-Si bonds whose strength increases with annealing temperature. However, it is found that, Si atoms resting in the region close to the surface of the sample are found to be oxidized. Detection from Si⁴⁺ bonds throughout the film indicates the presence of stoichiometric SiO₂ in the film. The possible formation mechanism is as a shell structure surrounding the Si nanocrystals. The depth profile investigations of PL and XPS were consistent with each other in which PL intensity and Si bond intensity are correspondingly changing.

As a comment on the work that can be done in the future, a better control on the size of the nanocrystals will be achieved. By controlling the size, different sized nanocrystals can be sputtered as a tandem structure as a prospective third generation solar cell. Formation of semiconductor nanocrystals and alumina matrix can be investigated in more detail by using Raman and FTIR spectroscopy. Angle resolved XPS can be studied and the effect of nanocrystals on the electrical properties of the films can be investigated in terms of charging and discharging.

REFERENCES

- [1] Feynman, R. P.; Caltech, <http://www.its.caltech.edu/~feynman/plenty.html> (1959), last accessed date: 2 July 2008.
- [2] Taniguchi N.; *On the Basic Concept of “Nano-Technology”*, Proc. Intl. Cond. Prod. Eng. Tokyo, Part II, Japan Society of Precision Engineering (1974)
- [3] Bardeen J., Brattain W. H.; Phys. Rev., 75, 1208 (1949)
- [4] Moore G E.; Electronics, 38, 114 (1965)
- [5] Moore G. E.; Tech. Dig. IEDM, 21, 11 (1975)
- [6] Tsoukas D., Dimitrikas P., Koliopolou S., Normand P.; Mater. Sci. Eng. B 93, 124 (2005)
- [7] Serincan U.; *Formation of Semiconductor Nanocrystals in SiO₂ Matrix by Ion Implantation*, PhD Thesis, Department of Physics, METU, Ankara (2004)
- [8] Wang Y., Herron N.; J. Phys. Chem. 95, 2, 525 (1991)

- [9] Hao M., Hwang H., Lee J. C.; Appl. Phys. Lett., 62, 1530 (1993)
- [10] Gonzalez-Varona O., Garrido B., Cheylan S., Perez-Rodriguez A., Cuadras A., Morante J. R.; Appl. Phys. Lett., 82, 2151 (2003)
- [11] Blauwe J. D.; IEEE Transactions on Nanotechnology, 1, 1 (2002)
- [12] Ammendola G., Ancarani V., Triolo V., Bileci M., Corso D., Crupi I., Perniola L., Gerardi C., Lombardo S., DeSalvo B.; Solid State Electronics, 48, 1483 (2004)
- [13] Iannaccone G., Coll P.; Appl. Phys. Lett., 78, 14, 2046 (2001)
- [14] Canham L. T.; Appl. Phys. Lett., 57, 1046 (1990)
- [15] Fauchet P. M.; IEEE Journal of Quantum Electronic., 4, 6, 1020 (1998)
- [16] Kulakci M., Serincan U., Turan. R.; Semicond. Sci. Technol., 21, 1527 (2006)
- [17] Pellegrino P., Garrido B., Garcia C., Arbiol J., Morante J. R., Melchiorri M., Daldosso N., Pavesi L., Scheid E., Sarrabayrouse G.; J. Appl. Phys., 97, 074312 (2005)

[18] Walters R. J., Kalkman J., Polman A., Atwater H. A., de Dood D. A.; Phys. Rev. B, 73, 132302 (2006)

[19] Dal Negro L., Yi J. H., Michel J., Kimerling L. C., Chang T. W. F., Sukhovatkin V., Sargent E. H.; Appl. Phys. Lett., 88, 233109 (2006)

[20] Walter R. J., Bourianoff G. I., Atwater H. A.; Nature materials, 4, 143 (2005)

[21] Conibeer G.; Materials Today, 10, 11 (2007)

[22] Conibeer G., Green M. A., Corkish R., Cho Y., Cho E. C., Jiang C. W., Fangsuwannarak T., Pink E., Huang Y., Puzzer T., Trupke T., Richards B., Shalav A., Lin K. I.; Thin Solid Films, 511, 654 (2006)

[23] Basore, P. A., 4th World Conf., PV Energy Conversion, Hawaii, 2089 (2006)

[24] Serincan U., Yerci S., Kulakci M., Turan R.; Nucl. Instr. and Meth. in Phys. Res. B, 239, 419 (2005)

[25] Serincan U., Aygun G., Turan R.; Journal of Luminescence , 113, 229 (2005)

[26] Serincan U., Kulakci M., Turan R., Foss S., Finstad T. G.; Nucl. Instr. and Meth. in Phys. Res. B, 254, 87 (2007)

[27] Yerci S., Serincan U., Dogan I., Tokay S., Genisel M., Aydinli A., Turan R.; J. Appl. Phys., 100, 074301 (2006)

[28] Yanagiya S., Ishida M.; Journal of Electronic Materials, 28, 5 (1999)

[29] Zhu Y., Wang H., Ong P. P.; Physica E, 15, 118 (2002)

[30] Robertson, J.; Rep. Prog. Phys., 69, 327 (2004)

[31] Ay F., Aydinli A.; Opt. Mat.. 26, 33 (2004)

[32] Ossicini S., Pavesi L., Priolo F., *Light Emitting Silicon for Microphotronics*, Springer, Berlin (2003)

[33] Krebs H. *Fundamentals of Inorganic Crystal Chemistry*, McGraw-Hill, London, U.K., 242 (1968)

[34] Ching W. Y., Xu Y. N.; J. Am. Ceram. Soc., 77 [2] 404 (1994)

[35] Wyckoff R. W. G., *Crystal Structures*, 2nd ed.; Wiley, New York, 274 (1964)

[36] Stumpf H. C., Russell A. S., Newsome J. W., Tucker C. M.; Ind. Eng. Chem. 42 1398 (1950)

- [37] Santos P. S., Santos H. S., Toledo S. P.; *Materials Research*, 3 [4] 104 (2000)
- [38] Wefers K., Misra C., *Oxides and Hydroxides of Aluminum*, ALCOA, Laboratories, Pennsylvania, USA, 20 (1987)
- [39] Thomas L. H., *Proc. Cambridge Phil. Soc.* 23 542 (1926); Fermi E., *Z. Phys.* 48 73 (1928)
- [40] Hohenberg P., Kohn W., *Phys. Rev. B* 136 864 (1964)
- [41] Kohn W., Sham L.J., *Phys. Rev.* 140A 1133 (1965)
- [42] Kiejna A., Wojciechowski K. F.; *Metal Surface Electron Physics*, Elsevier 77 (1996)
- [43] Sevik C. and Bulutay C.; *J. Mater. Sci* 42:6555-6565 (2007)
- [44] J. E. Medvedeva, E. N. Teasley, M. D. Hoffman, arXiv:0706.1986v1 [cond-mat.mtrl-sci] 13 Jun 2007
- [45] French R. H., Müllejans H., Jones D. J.; *J. Am. Ceram. Soc.*, 81 [10] 2459 (1998)

- [46] Saleh B. E. A., Teich M. C.; *Fundamentals of Photonics*, Wiley 573 (1991)
- [47] Elfros Al. L., Elfros A. L.; *Semiconductors*, 16, 1209 (1982)
- [48] Lifshitz I. M., Slyozov V. V.; *J. Phys. Chem. Sol.*, 28, 35 (1961)
- [49] Abraham F. F.; *Homogeneous Nucleation Theory*, New York: Academic Press (1974)
- [50] Koch S. W.; *Dynamics of First Order Phase Transitions in Equilibrium and Nonequilibrium Systems*, Berlin: Springer (1984)
- [51] Slyozov V. V., Sagalovich V. V.; *Sov. Phys. Uspekhi*. 151, 67 (1987)
- [52] Liu L-C., Kim M. J., Risbud S. H., Carpenter R. W.; *Philosoph Mag. B.*, 63, 769 (1991)
- [53] Donald M. M.; *Handbook of PVD Processing*, Noyes, 343 (1998)
- [54] Kurt J. Lesker Company,
http://www.lesker.com/newweb/menu_depositionmaterials.cfm/, last accessed date: 2 July 2008.

- [55] VAKSIS, AR-GE ve Mühendislik, Ankara, TURKEY
<http://www.vaksis.com/>, last accessed date: 2 July 2008.
- [56] Wilmott P. R.; Progress in Surface Science, 76, 163 (2004)
- [57] Institute of Materials & Machine Mechanics, Slovak Academy of Sciences,
<http://www.umms.sav.sk/>, last accessed date: 2 July 2008.
- [58] Sproul W. D., Christie D. J., Carter D. C.; Thin Solid Films, 491, 1 (2005)
- [59] Alagöz A. S.; *Synthesizin Germanium and Silicon Nanocrystals Embedded in Silicon Dioxide by Magnetron Sputtering Deposition Technique*, M.Sc. Thesis, Department of Physics, METU, Ankara (2007)
- [60] Brundle R. C., Evans C. A., Wilson S. Toney M. F.; *Encyclopedia of Materials Characterization*, Butterworth - Heinemann (1992)
- [61] Cullity B. D.; *Elements of X-Ray Diffraction*, Addison Wesley, Reading (1978)
- [62] Patterson, A.L.; Physical Review, 56, 978 (1939)
- [63] Bubert H., Janet H.; *Surface and Interface Analysis*, Viley-VCH Verlag GmbH (2002)

[64] Hufner S.; *Photoelectron Spectroscopy Principles and Applications*, Springer Verlag, Berlin (2002)

[65] Shirley D. A.; Phys. Rev., 55, 4709 (1972)

[66] Thougard S.; Surf. Interface Anal., 11, 453 (1988)

[67] Oswald S., Reiche R.; Appl. Phys. Sci., 179, 307 (2001)

[68] Yerci S., Yildiz I., Kulakci M., Serincan U., Barozzi M., Bersani M., Turan R.; J. Appl. Phys., 102, 024309 (2007)

[69] Renault O., Marlier R., Gely M., De Salvo B., Baron T., Hansson M., Barrett N. T.; Appl. Phys. Lett., 87, 163119 (2005)

[70] Yerci S.; *Spectroscopic Characterization of Semiconductor Nanocrystals*, M.Sc. Thesis, Department of Physics, METU, Ankara (2007)

[71] Goksen K.; *Optical Properties of Some Quaternary Thallium Chalcogenides*, PhD Thesis, Department of Physics, METU, Ankara (2008)

[72] Serincan U.; *Formation of Semiconductor Nanocrystals in SiO₂ Matrix by Ion Implantation*, PhD Thesis, Department of Physics, METU, Ankara (2004)

- [73] Bhatia C. S., Guthmiller G., Spool A. M.; *J. Vac. Sci. Technol. A*, 7, 3 (1989)
- [74] Sedga B. G., Jacquet B., Besse J. P.; *Vacuum*, 62, 27 (2001)
- [75] Lee J., Kim S. S., Im S.; *J. Vac. Sci. Technol. B*, 31, 3, 953 (2003)
- [76] Voigt M., Sokolowski M.; *Materials Science and Engineering B*, 109, 99 (2004)
- [77] Ha, W. H., Choo M. H., Im S.; *Journal of Non-Crystalline Solids*, 303, 78 (2002)
- [78] Pradhan A. A., Ismat S. S., Unruh K. M.; *Rev. Sci. Instrum*, 73, 11, 3841 (2002)
- [79] Park C. J., Kwon Y. H., Lee Y. H., Kang T. W., Cho H. Y., Kim S., Choi S. H., Elliman R. G.; *Appl. Phys. Lett.*, 84, 2667 (2004)
- [80] Bausa L. E., Vergara I., Jacque F., Garcia Sole J.; *J. Phys.: Condens. Matter*, 2, 9919 (1990)
- [81] Tetelbaum D. I., Gorshkov O. N., Ershov A. V., Kasatkin A. P., Kamin V. A., Mikhaylov A. N., Belov A. I., Gaponova D. M., Pavesi L., Ferraioli L., Finstad T. G., Foss S.; *Thin Solid Films* 515, 333 (2006)

- [82] Kokonou M. Nassiopolou A. G., Travlos A.; *Materials Science and Engineering B*, 101, 65 (2003)
- [83] Yilmaz E., Dogan I., Turan R.; *to be appeared in Nuclear Inst. And Methods in Physics Research, B* (2008)
- [84] Chauhan R. K., Chakrabarti P.; *Microelectron J.*, 33, 3, 197 (2002)
- [85] Arshak A., Arshak K., Korostynska O., Zleetni S.; *IEEE Trans. Nucl. Sci.* 1, 78 (2003)
- [86] Lenahan P. M., Dressendorfer P. V.; *J. Appl. Phys.*, 55, 10, 3495 (1984)
- [87] Yu. Z. Q., Li C., Zhang N.; *Journal of Luminescence*, 99, 29 (2004)
- [88] Klug H. P., Alexander L. E.; *X-Ray Diffraction Procedures*, Wiley, New York (1974)
- [89] Ramirez R., Tardio M., Gonzalez R., Santiuste J. E. M., Kotka M. R.; *J. Appl. Phys.*, 101, 123520 (2007)
- [90] Evans B. D.; *J. Nucl. Mater.*, 219, 202 (1995)

- [91] Song Y., Zhang C. H., Wang Z. G., Sun Y. M., Duan J. L., Zhao Z. M. ; Nucl. Instrum. and Meth. in Phys. Res. B., in press (2007)
- [92] Shangda X., Changxin G., Libin L., Ellis D. E.; Phys. Rev. B., 35, 7671 (1987)
- [93] Munisso M. C., Zhu W., Leto A., Pezzotti. G.; J. Phys. Chem. A, 111, 3526 (2007)
- [94] Kwok R. W. M.; www.phy.chuk.edu.hk/~surface/XPSPEAK, last accessed date: 2 July 2008.
- [95] Dogan I., Yildiz I., Turan R.; *to be appeared in Physica E* (2008)